Multi-plane Optical Diagnostics for Flow Dynamics and Turbulent Flame Fronts

Qichi He

Wadham College

University of Oxford

Supervisor: Prof. Benjamin Williams

A thesis submitted for the degree of

Doctor of Philosophy

Trinity 2024

Abstract

This thesis presents the first application of defocusing macroscopic Particle Image Velocimetry (PIV) based on an image splitting device. The compact and low-cost image splitting optics design provides the potential to extend any existing single-plane PIV system for flow field measurements on at least two planes. This work reports a well-controlled flow rig test for evaluating the measurement accuracy of the image splitting based defocusing PIV. This is the first systematic evaluation of macroscopic defocusing PIV. It points out that the measurement accuracy is not only related to depth of field, which is known widely, but also influenced by the flow fields on the two planes. With a typical field of view size (35 $\times$ 54 mm), the measurement error is found to be less than 0.1 pixel per time step, from 20 mm plane separation onwards. The image splitting device is successfully applied to simultaneously resolve the instantaneous swirl flow and tumble vortex structures in an optical internal combustion engine, which is not possible with a conventional single-plane PIV system. This example highlights how the defocusing approach could maximise the amount of information that may be collected from systems featuring limited optical access.

Simultaneous two-plane flame front measurement using defocusing PIV is also reported for the first time. A novel two-step filter is specifically designed for enabling highly reliable flame front tracking on two planes, despite interference from out-of-focus signals. With a 22 mm plane separation, the typical flame front position error due to out-of-focus crosstalk is smaller than 1 mm. Building on this work, a 3D printed laser splitting optics design is proposed, to enable rapidly reconfigurable, simultaneous four-plane flame front tracking using a single PIV laser, by combining the novel defocusing method with the typical polarisation method. However, a change in the scattered light polarisation is reported, which is inferred to be caused by stress-induced birefringence

of fused silica under high sealing pressure. The failure of polarisation separation led to the use of defocusing separation and temporal separation (2 μs) for the four-plane flame imaging tests, but this also highlights the importance of the defocusing approach: In cases where polarisation separation is ineffective, defocusing separation and wavelength separation would become the only two methods for simultaneous multi-plane measurement. The latter is normally costly and adds experimental complexity. Four-plane flame front tracking is demonstrated in the optical engine, with a plane-to-plane separation of 10 mm. Using the four-plane flame imaging technique, this thesis explores the potential to evaluate the local cycle-to-cycle variation (CCV) of combustion on the four planes. It is shown that the CCV in pressure-trace-derived overall burn duration (10% to 90%) is not correlated with the local combustion CCV, which may be related to the in-cylinder flow structure. Enabled by the multi-plane imaging technique, in future, correlations between local combustion CCV, in-cylinder flow CCV, and overall engine performance can be further investigated, notwithstanding the limited optical access offered by an optical engine.

Acknowledgements

Looking back on this long journey of my DPhil, I received so much help and support from a great many people.

First and foremost, my thanks go to Professor Ben Williams, to whom I am forever grateful. He offered me the opportunity to study at Oxford, and led me into the fantastic world of optical diagnostics. All of my academic achievements over the last four years would not have been possible without his extensive knowledge and dedicated supervision. Sincerely, I thank him for all his constant care and persistent support throughout this journey.

I am deeply indebted to Dr. Chris Willman, to whom I owe a huge part of my experimental skills. His willingness and patience in teaching me his knowledge of laser diagnostics and optical engine laid the foundation for my success.

I am grateful to Professor Richard Stone, for his willingness to help and provide advice during my entire DPhil. I cannot count how times he helped with the optical engine tests. I am privileged to have the opportunity to discuss and present my research to him regularly, and I owe a great deal of my ability in academic presentation to his insightful inputs.

I very much appreciate the financial support from the Department of Engineering Science and the EPSRC Prosperity Partnership project, without which I could not perform any of the work presented in this thesis.

I would like to express my gratitude to the colleagues and staff at the Engineering Science Department. Thanks to Dr. Kharthik Chakravarthy, the first one showing me details of a real optical diagnostic experiment in

the laser lab. His kind share of his knowledge and experience is my first "exposure" to how an optical diagnostic test is built in the real world. Thanks to Dr. Peter Walters, for his kind patience in assisting me with the design of those critical parts in my experiments. I also thank David Ilsley, for his professional suggestions on engines and plumbings (and all his funny jokes!)

I would also like to thank my buddies of the Thermal Propulsion System Research Group (TPSRG). Sam (B), Sam (W), Ruixuan, Varun, Tejo, to all those days we fought in the same trench! I will never forget those formal dinners, pub nights, punting trips...(can't list all of them!) Perhaps one day I will be too old to remember any research I did at Oxford, but your friendship is always a treasure in my life. To my buddies outside the office, Will, Liam, Shuang, Chengxuan, thank you for the nice meals, fantastic coffee, exciting board games, everything.

Last but not least, I could not get to this far without the love and support from my parents and family. You are always my harbour and motivation.

Contents

List of Figures

List of Tables

Acronyms

BDC Bottom Dead Centre

CAD Crank Angle Degrees

CCV cycle-to-cycle variation

CI Compression Ignition

COV Coefficient of Variation

DAQ Data Acquisition

DI Direct-injection

DNS Direct Numerical Simulation

DOC Depth of Correlation

ETCS Engine Timing Control System

HWA Hot Wire Anemometry

ICE Internal Combution Engine

IMEP Indicated Mean Effective Pressure

LDA Laser Doppler Anemometry

LES Large Eddy Simulation

LIF Laser-induced Fluorescence

LSV Laser Speckle Velocimetry

MART Multiplicative Algebraic Reconstruction Technique

MFB Mass Fraction Burned

NI National Instruments

NPBS Non-Polarising Beamsplitter

PBS Polarising Beamsplitter

PFB Planar Fraction Burned

PFI Port Fuel Injection

PIV Particle Image Velocimetry

PPP Particles Per Pixel

PTU Programmable Timing Unit

RANS Reynolds-averaged Navier–Stokes

RCOVF Ratiometric Coefficient of Variation Filter

RSMIF Ratiometric Sliding Maximum Intensity Filter

SI Spark Ignition

TDC Top Dead Centre

VVA Variable Valve Actuation

Chapter 1

Introduction

1.1 Motivation

Fluid motions are omnipresent and significant in our lives. The large-scale ocean and atmospheric streams drive climate and weather. The propulsion performance of cars, airplanes and rockets are highly dependent on their aerodynamics as they interact with the surrounding air. The small-scale blood flows in vessels are vital to the circulatory system and health. It has been a consensus for centuries that a detailed understanding of flows is essential to improve human life and be environmentally friendly.

Whether a flow contains chemical reactions classifies it as a reactive or non-reactive flow. Combusting flows are a type of reactive flow and one of the most complicated physical phenomena in nature, coupling fast chemical reactions, (mostly turbulent) fluid dynamics, heat transfer and species transport. Recently, turbulent premixed combustion is increasingly attracting attention in industrial applications where low (or zero) emissions are aimed for [1].

The complexity of flows determines that understanding them in detail is usually challenging. With the rapid development of high-performance computing and fluid modelling, numerical simulation is playing a more and more important role in fluid mechanics research, since it has the capability of resolving flow properties and variables

in space and time. However, cost-effective simulation techniques such as Reynolds-averaged Navier–Stokes (RANS) methods and Large Eddy Simulation (LES) require appropriate combinations of models for predicting the behaviours of turbulence, chemical reactions, heat transfer, to name just a few. These models are often based upon specific approximations or assumptions that are valid in certain contexts [2]. On the other hand, Direct Numerical Simulation (DNS) is not dependent on certain flow models, but is too computationally expensive for medium to large-scale flow problems. Therefore, flow measurements remain irreplaceable to develop fluid theory, validate numerical models, guide and optimise flow device design, and so on.

Optical techniques for measuring flow parameters have clear advantages over traditional methods (such as velocimetry by hot wire), as they offer the capability to take measurements without perturbing the flow fields in interest. Particle Image Velocimetry (PIV) is one of the most popular optical techniques for measuring the instantaneous velocity field in a flow, by imaging and cross-correlating the tracer particles seeded into the flow.

A typical PIV measurement resolves the velocity field within a two-dimensional plane. For turbulent flows in which flow field structures are highly three-dimensional, single-plane measurements cannot acquire essential out-of-plane information. Many efforts have been made to extend PIV to three-dimensional (3D) measurements. Scanning PIV is a straightforward approach, but may restrict the application to moderate flow rates and turbulence levels. Tomographic PIV uses multiple cameras simultaneously taking images from different perspectives for a 3D flow field reconstruction. In a device where optical access is limited, deploying a camera array for an accurate tomographic reconstruction with similar spatial resolution to single-plane PIV could be challenging or impossible.

Alternatively, researchers attempted simultaneous multi-plane measurements by using the polarisation and wavelength differences of the light. Simultaneous measurements with high spatiotemporal resolution can be achieved, but the number of measurement planes is limited by the polarisation/wavelength differences of the laser sheets.

Orthogonal linear polarisations could permit a pair of planes to be distinguished. Further increasing the number of measurement planes means introducing more laser sheets with different wavelengths, which is costly and adds experimental complexity. To the best of the author's knowledge, by employing the polarisation/wavelength approach, quad-plane PIV is state-of-the-art [3].

In this thesis, a new multi-plane PIV method based on an image splitting device and defocusing is proposed. As an inexpensive and compact add-on, the image splitting device can be used alone or combined with the polarisation/wavelength method, to increase the number of measurement plane(s) of single/multi-plane PIV setups. The high in-plane spatial resolution characteristic of conventional single-plane PIV could be retained. Potentially, any standard single-plane PIV system can be modified using the device, to achieve simultaneous PIV measurements on at least two planes. This technique would be advantageous in a practical flow device where optical access is limited. The velocimetry accuracy of the proposed defocusing based method is studied using a laminar flow rig test. The proposed method is applied for a simultaneous two-plane PIV in an optically-accessible internal combustion engine (optical engine), to simultaneously measure the instantaneous tumble and swirl vortex structures during the engine compression stroke. Due to cycle-to-cycle variation (CCV), typical single-plane PIV is not able to simultaneously resolve the instantaneous tumble and swirl vortex structures in individual cycles.

Fundamentally, the PIV technique records and processes the Mie scattering of light from seeded particles carried in the flow. Due to the temperature change from the unburned to the burned regions in a combusting flow, the sharp gradient in the particle number density in the Mie-scattering images could be used for marking the thin chemical reaction layer (i.e. flame front) of turbulent premixed combustion. **In this thesis**, the proposed image splitting method is applied for simultaneous two-plane flame front detection, using a single PIV laser and a single camera. By using a novel two-step filter, the out-of-focus particle images are effectively removed, while the in-focus particle images remain, allowing the turbulent flame fronts on two planes to be detected

simultaneously. Furthermore, this thesis shows a laser splitting setup for simultaneous four-plane flame front tracking based on a single PIV laser, by exploiting the polarisation difference of the laser beams from a typical two-cavity laser. Four-plane flame front tracking is demonstrated in the optical engine. A change in scattered light polarisation is reported, which is shown to be related to the sealing pressure applied to the fused silica cylinder liner. The inability to apply polarisation discrimination led to the use of defocusing separation and temporal separation (2 μs) in the four-plane flame front measurement. On the other hand, this problem emphasises the significance of the defocusing method. In cases where polarisation separation is challenging, defocusing separation and wavelength separation would become the only two methods for simultaneous multi-plane measurement. Based on the four-plane combustion images, this thesis explores the local CCV of combustion. It is shown that the overall burn duration calculated using the engine pressure trace cannot describe the local combustion characteristics on the four planes, which might itself be strongly influenced by in-cylinder flow structures. Enabled by the multi-plane measurement technique, correlations between local combustion CCV, in-cylinder flow CCV, and overall engine performance can be further investigated in the future.

1.2 Thesis Structure

Following this introductory chapter, Chapter 2 explores the technical background of flow field visualisation and measurement. A general introduction to the terminology and working principle of PIV is provided. The key focus of the chapter is to discuss and evaluate different existing approaches for extending PIV to multi-plane and 3D flow/flame measurements.

Chapter 3 details the design and principle of the image splitting optics. The setup and data analysis of the laminar flow rig test are explored, which is the first systematic evaluation of macroscopic defocusing PIV.

Chapter 4 describes how the image splitting device was applied to a simultaneous

two-plane PIV test in the optical engine. A general introduction to internal combustion engines and optical engines is given. The experimental setup and test condition are shown. The evaluation of two-plane cross-talk is discussed in detail, followed by demonstrating the simultaneous measurement of instantaneous swirl flow and tumble vortex structures.

Chapter 5 starts by presenting the experimental setup and test condition of a simultaneous two-plane flame front measurement in the optical engine. The two-step image filter design for effectively removing out-of-focus particle images is the key outcome of the chapter. An evaluation of two-plane flame front tracking error is performed.

Chapter 6 presents a four-plane flame front measurement in the optical engine. It begins by discussing the laser splitting optics design, which generates four laser sheets based on a single PIV laser. In principle, the laser splitting optics and the image splitting optics enable simultaneous four-plane flame front tracking based on defocusing separation and polarisation separation. In this chapter, the change in scattered light polarisation is presented, which is shown to be related to the sealing pressure applied to the fused silica cylinder liner. Because of the inability to use polarisation discrimination, four-plane flame front tracking based on defocusing separation and temporal separation (2 μs) was performed. At the end of this chapter, the local CCV of combustion is proposed, and evaluated using the four-plane combustion images.

Chapter 7 summarises the contribution made by this thesis. Future extensions of this work are discussed.

1.3 Peer-reviewed Publications

- (In preparation) Qichi He, Christopher Willman, Richard Stone, Martin Davy, Benjamin Williams. Four-plane Flame Front Detection Using a PIV laser and Image Splitting Optics. *Optics Express*.
- Qichi He, Christopher Willman, Benjamin Williams. Simultaneous Two-plane Flame Front Detection Using PIV Based on Defocusing. *Optics Letters*, 49(3),

pp.422-425, 2024.

- Qichi He, Christopher Willman, Richard Stone, Benjamin Williams. Inexpensive Multi-plane Particle Image Velocimetry Based on Defocusing: Proof of Concept on Two-component Measurement. *Physics of Fluids*, 35(6), 2023 **(Featured Article of the Journal)**.
- Christopher Willman, Qichi He, Benjamin Williams, Richard Stone, Matthew McAllister. Multi-plane PIV Using Depth of Field for In-cylinder Flow Measurements. *WCX SAE World Congress Experience. SAE International*, 2023-01-0213, 2023.

1.4 Presentation and Poster

- Oral Presentation: Qichi He, Christopher Willman, Benjamin Williams. Simultaneous Two-plane Flame Front Detection Using Defocusing Based PIV. *Current Research in Combustion: A Forum for Research Students and Early Career Researchers. Institute of Physics Combustion Physics Group*, 2023.
- Poster: Qichi He, Christopher Willman, Benjamin Williams. Simultaneous Two-plane Particle Image Velocimetry (PIV) Using a Single Camera. *Oxford Photonics Day 2023*, 2023.

Chapter 2

Literature Review

This Chapter begins by briefly reviewing flow field visualisation and measurement techniques, followed by a general introduction to the working principle of PIV. Different existing approaches for extending PIV to multi-plane or 3D measurements are discussed, centering on their advantages and shortcomings (Section 2.3). The application of the defocusing principle in microscopic PIV (μPIV) is introduced, and how the defocusing principle could be applied to macroscopic multi-plane PIV is discussed (Section 2.4).

The application of PIV to turbulent flame front detection is then introduced, and compared with laser-induced fluorescence (LIF), another common approach for flame front measurement (Section 2.5). Similar to flow velocimetry, different approaches for multi-plane or 3D flame front measurement are reviewed and discussed.

2.1 Flow Field Visualisation and Measurements

Dating back to the 1880s, Osborne Reynolds used ink to visualise the streamlines in pipe flows to illustrate the laminar/turbulent transition [4]. In the 1900s, Étienne-Jules Marey built a smoke machine with 58 channels to visualise the bending of streamlines around objects [5]. In the 1930s, Ludwig Prandtl used film cameras to qualitatively

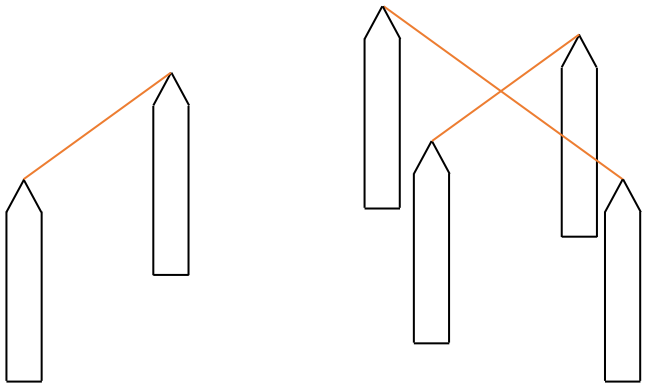

Figure 2.1: Hot Wire Anemometry (HWA) probes for one-component (a) and two-component (b) measurements.

illustrate the vortex motions in turbulent flows using particle path lines [6]. The qualitative visualisation of flows gives valuable insight into the global flow processes and the early-stage development of fluid mechanics. However, in order to prove analytical models and to validate numerical flow simulations, quantitative velocity field measurements are required.

Before the development of high-power lasers, Hot Wire Anemometry (HWA) was one of the most popular techniques for flow velocity measurement. It works by measuring the heat transfer from a small length of wire to the surrounding fluid. Careful calibrations under known flow velocities are needed, to provide the relationship between the flow velocity and heat transfer. A probe with a single wire could measure one component of the flow velocity in the vicinity of the wire (itself typically with a diameter of $\sim 5\ \mu m$ and a length of several millimetres [7]). Normally, multi-component measurement would require a probe with perpendicular wires. Examples of HWA probes are shown in Fig. 2.1. To simultaneously measure flow velocities at more than one location, a probe array is required.

One of the biggest advantages of HWA is that the sensor output is an analogue signal, which means the measurement can be made with a very high temporal resolution, which

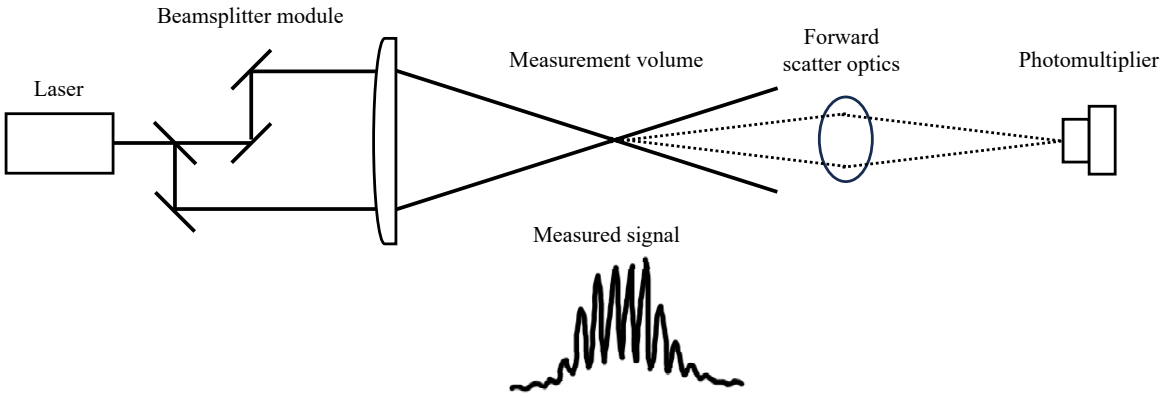

Figure 2.2: Optical arrangement for Laser Doppler Anemometry (LDA) (adapted from [8] with permission).

could be very useful in highly-turbulent flow study. However, the HWA is an intrusive measurement technique which would disturb the flow of interest, especially when multi-point measurement is performed. The development of high-power lasers in the 1970s made non-intrusive optical diagnostics become much more available. Among them, Laser Doppler Anemometry (LDA) is one of the most common laser-based techniques for point-wise velocity measurements and has been used extensively in experimental fluid mechanics research.

In a typical LDA setup (Fig. 2.2), two coherent laser beams are used to create an interference pattern in the measurement location. The fluid is seeded with particles which randomly pass through the interference fringe pattern and scatter light, which is recorded by a photodetector. The frequency of the scattered light is a function of the fringe spacing (which itself depends on the beam angle and the incident light wavelength), and the particle (flow) velocity [9].

Although being non-intrusive, LDA is a point-wise measurement technique, and the extension of LDA to multi-point measurement is not trivial. On the other hand, the instantaneous flow field structure over a large domain (i.e. either a plane or a volume)

is essential information for fluid mechanics research. Particle Image Velocimetry (PIV) is a technique which is capable of measuring instantaneous multi-component velocity fields within a plane or a volume, as described as follows.

2.2 PIV for Flow Field Measurements

It has been demonstrated that particles are well suited for labeling fluid elements [10]. Tracer particles need to be chemically and electrically neutral and make negligible changes to the flow properties. They should be able to follow the flow, ideally even at high accelerations and gradients, so they should have small sizes. In practice, particles that have a diameter of the order of visible light wavelengths are used ($\sim$1 μm), so that a high tracer fidelity could be maintained, and the relatively strong Mie scattering can be used for particle detection. To detect the particles' positions, a laser sheet is used for illumination and a camera records the Mie scattered light. In the very early application of flow velocity measurements with particles, very large seeding densities were used, so the images showed speckle patterns instead of individual particles [11, 12]. This was done on purpose because speckle analysis for solid material deformation was proven back then, which is why the early particle-image-based velocimetry is also called Laser Speckle Velocimetry (LSV). However, the multiple scatter caused by the high seeding density could result in signal blur. Therefore, Ronald Adrian, Christopher Pickering, and Neil Halliwell introduced PIV (Particle Image Velocimetry), in which individual tracer particles were imaged and distinguishable [13, 14]. Once digital recordings with double-frame acquisition and fast cross-correlation processing became available, the global rise of this technique began.

Fig. 2.3 shows a sketch of a standard double pulse PIV system. In PIV, the flow with tracer particles is illuminated twice, separated by a known time interval, leading to a pair of images in which the particles have moved. By using a statistical interrogation technique (cross-correlation), the displacements of groups of particles are determined. The flow velocity field is then determined based on particle displacements and the

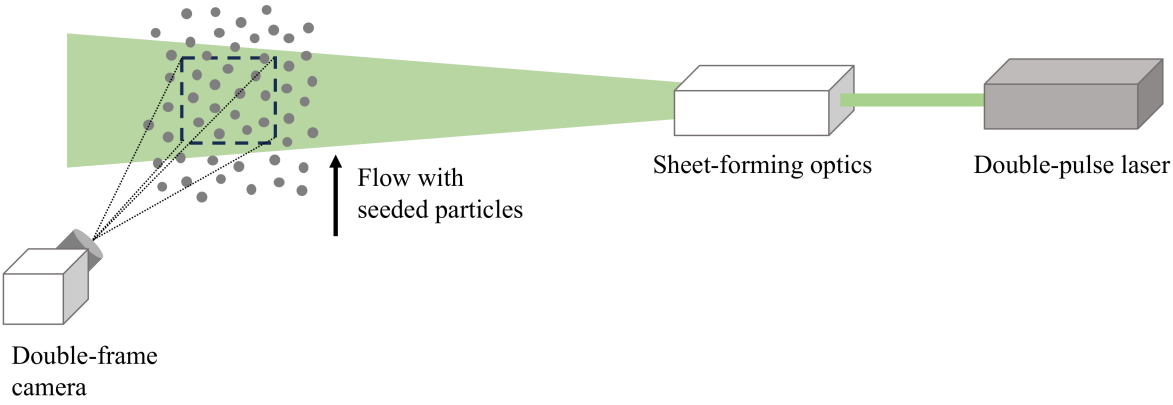

Figure 2.3: Layout of a typical planar PIV setup. The flow is seeded with tracer particles, illuminated twice by a laser sheet. A digital double-frame camera records the scattered light.

known time interval between frames.

The velocity field mapping begins by dividing PIV images into square interrogation windows. Each window in the two frames is cross-correlated to yield a peak in the cross-correlation function, therefore producing the displacement of local flow motion (Fig. 2.4). A calibration grid is then typically used to convert the displacement unit from pixels into metres.

In practice, the spatial resolution of the velocity field is determined by the size of the cross-correlation window, which is mostly limited by the particle number and particle displacement within the window. The two parameters jointly determine the cross-correlation peak strength and signal to noise ratio of the measurement. Richard D Keane and Ronald J Adrian [15, 16] pointed out that for an optimum PIV measurement, the particle number in a cross-correlation window should be larger than 10, and the particle displacement should be less than one-fourth of the window width. While increasing the particle number is straightforward, accommodating particle displacement is more challenging since it is related to the flow velocity field. In a high-speed flow, the particles could "escape" a cross-correlation window, leading to a very weak correlation signal. To address that, the so-called "multi-pass" approach is adapted by most

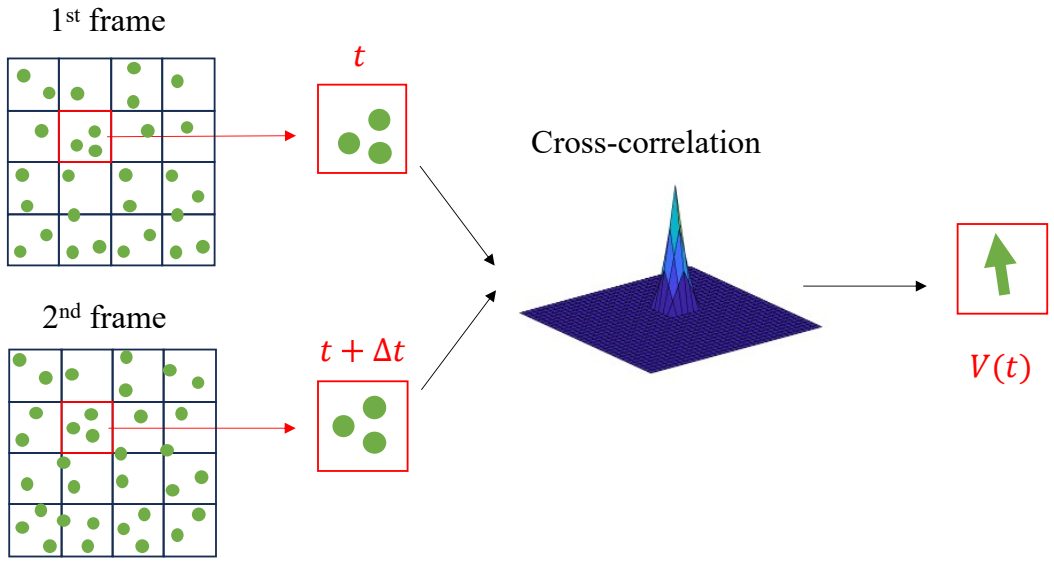

Figure 2.4: Illustration of the PIV cross-correlation for determining local flow motion.

PIV algorithms nowadays, to decouple the correlation window size from flow speed. Fig. 2.5 shows the principle of the multi-pass scheme. The first interrogation pass uses a large correlation window size to ensure sufficient particle pairs for a strong correlation peak. The subsequent pass (passes) could then use smaller correlation windows, pre-shifted with the displacements inferred from the previous pass. In the subsequent pass (passes), some PIV algorithms adopt the "window deformation technique", in which the correlation windows are deformed based on the neighbouring velocity vectors inferred from the previous pass (see Fig. 2.6), so that the cross-correlated sections of the windows are most likely to hold the identical particles. It is verified that the window deformation technique could improve the robustness and accuracy of the multi-pass algorithm [17, 18].

With two cameras in a stereoscopic configuration, the planar PIV technique can recover three-component velocity measurement within the two-dimensional plane [19]. As shown in Fig. 2.7, particle displacement along the optical axis (z) causes a difference

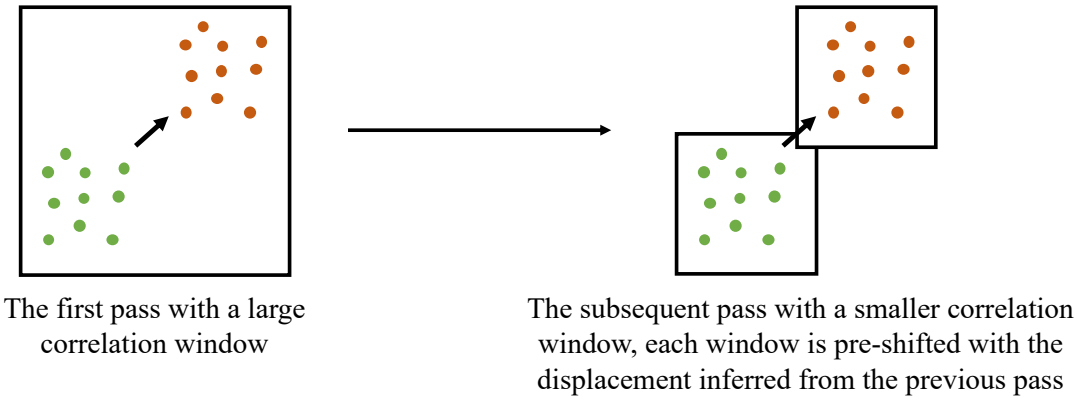

Figure 2.5: Illustration of the PIV multi-pass scheme.

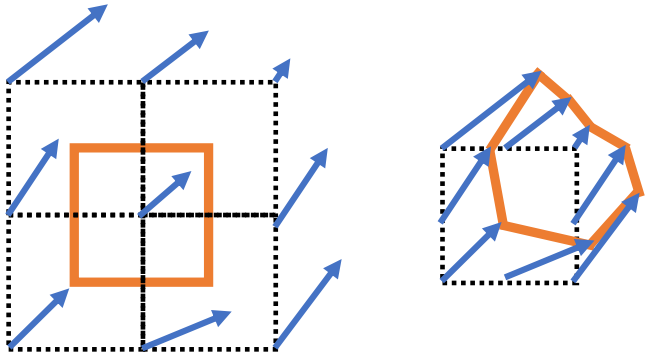

Figure 2.6: Illustration of the window deformation technique. The blue arrows indicate velocity vectors produced from the previous pass.

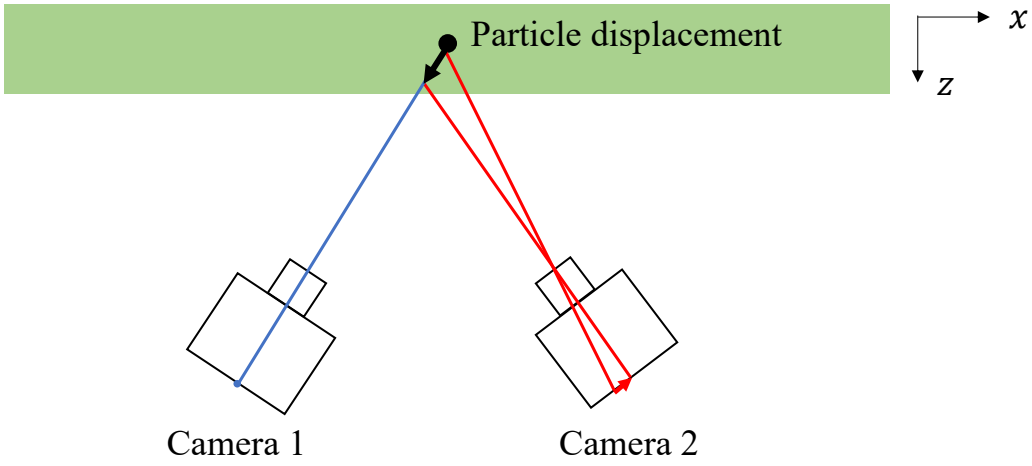

Figure 2.7: Illustration of stereoscopic PIV. The parallax of the two cameras is used to derive the out-of-plane velocity.

in the horizontal displacement (x) measured by the two cameras. By calibrating the parallax of the cameras, the three velocity components (dX, dY, dZ) of the particles could be obtained by combining the two vector maps (dx_1, dx_2, dy_1, dy_2) generated from the two cameras:

$$\begin{cases} \mathrm{A}_{11}\ dx_1 + A_{12}\ dx_2 + A_{13}\ dy_1 + A_{14}\ dy_2 = dX, \\ \mathrm{A}_{21}\ dx_1 + A_{22}\ dx_2 + A_{23}\ dy_1 + A_{24}\ dy_2 = dY, \\ \mathrm{A}_{31}\ dx_1 + A_{32}\ dx_2 + A_{33}\ dy_1 + A_{34}\ dy_2 = dZ, \end{cases} \tag{2.1}$$

in which the the matrix $A_{i,j}$ is obtained from calibration.

2.3 PIV for More Than a Single Plane

In most practical flow devices, the flow field structures are highly three-dimensional. To capture the essential out-of-plane information, many efforts were made to extend PIV to 3D velocity measurement. This Section serves as an overview of the typical approaches.

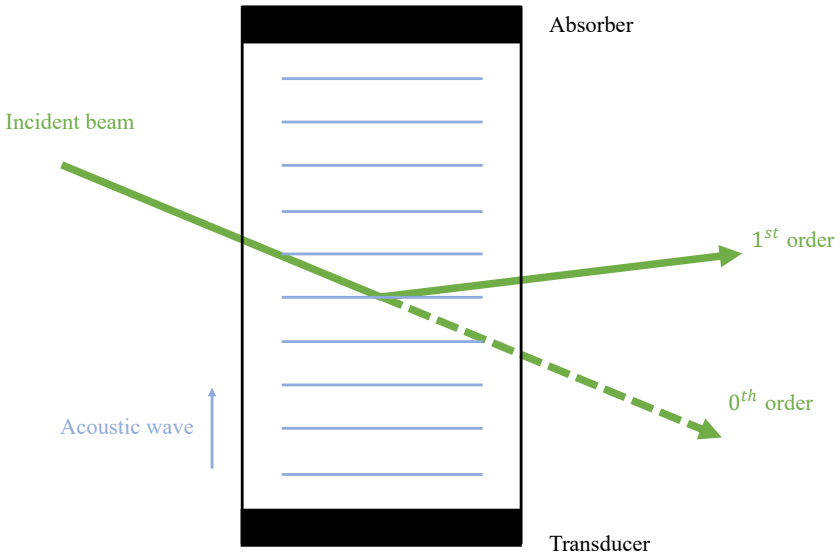

Figure 2.8: An acousto-optical deflector (AOD). The light deflection angle is adjusted by the acoustic frequency.

2.3.1 Scanning PIV and Time-average PIV

Temporal separation is the most straightforward way to record PIV images on different planes. In scanning PIV, the laser sheet is rapidly scanned by a mechanism such as a rotating mirror or an acousto-optical deflector (AOD) [20, 21, 22]. An AOD is a device which uses the interaction between sound waves and light waves to deflect a laser beam. Under the same acoustic amplitude, the acoustic frequency is varied to change the diffraction angle of the laser beam (Fig. 2.8). Scanning frequencies from several hundred to several thousand Hertz have been reported. Although it is conceptually straightforward, the sequential nature of scanning PIV may restrict the application to moderate flow rates and turbulence levels. Time-average PIV involves using translation stages to position the laser sheet at different depth planes [23, 24]. At each depth, the average in-plane velocity field is generated independently. The overall flow field structure is then analysed, which does not include any information on the instantaneous flow field.

2.3.2 Tomographic PIV

A common practice for 3D flow measurement is tomographic PIV. By simultaneously taking images using multiple cameras from different perspectives, 3D particle locations within the volume of interest are reconstructed [25]. The 3D reconstruction of an intensity field attempts to solve an under-determined problem described by:

$$\mathbf{f}_{(I,1)} = H_{(I,J)}\ \mathbf{g}_{(J,1)}, \tag{2.2}$$

in which $\mathbf{f}_{(I,1)}$ and $\mathbf{g}_{(J,1)}$ represent sensor pixel and volume voxel intensity distribution respectively, in the form of column vectors. The weight matrix H, which is also called the measurement matrix, determines the contributions of each discrete voxel to the intensity of each pixel on the camera sensor. The weight matrix is obtained by either ray tracing simulation or experimental calibration [26, 27, 28]. Since the number of pixels (equations) is much less than the number of voxels (unknown variables), solving voxel intensity distribution $\mathbf{g}$ with known $\mathbf{f}$ and H is a highly ill-posed problem, which cannot be solved by directly inverting the equation. Such a problem is typically solved by an iterative algorithm. A first guess ($\mathbf{g}^0_{(J,1)}$) is proposed randomly or based on prior knowledge of the volume of interest, then corrections are made based on the difference between real projections and the projections created by the estimated field. The Multiplicative Algebraic Reconstruction Technique (MART) is a common iterative correction algorithm, which updates the guess as follows:

Algorithm 1 The iteration scheme of MART

1. for each pixel i:

2. for each voxel j:

$$g^{k+1}_{(j,1)} = g^{k}_{(j,1)} \cdot \left(\frac{f_{(i,1)}}{H_{(i,J)}\ \mathbf{g}_{(J,1)}}\right)^{\lambda \cdot H_{ij}} \tag{2.3}$$

end loop 2

end loop 1

where λ is a relaxation factor ≤ 1 [29].

The iterative nature of solving a 3D particle field leads to the reconstruction being sensitive to the input and noise. The consensus is that the tomographic reconstruction accuracy is directly related to the particle number seen by the cameras, which is typically quantified using the metric Particles Per Pixel (PPP). As the cameras register more particles, more fake particles (so-called "ghost particles") are generated in the reconstruction process. A typical tomographic reconstruction algorithm could nowadays handle a PPP around 0.2, with a three-camera system [25, 30]. Since the PPP is determined jointly by both the particle seeding density and the reconstruction volume size, a tomographic PIV experiment needs to consider a balance between spatial resolution, volume size, and accuracy of the measurement. For a simple example, consider a tomographic reconstruction with a pixel (voxel) resolution as 0.1 mm/pixel (voxel). Correlation windows with a size of 16 $\times$ 16 $\times$ 16 voxels and 50 % overlap are used for generating velocity maps, leading to a spatial resolution as 0.8 mm per vector. A 0.2 PPP means that for each 16 $\times$ 16-pixel window in a 2D image, 51.2 particles exist along the line of sight of the window. In order to maintain sufficient cross-correlation peak signal, at least 10 particles are needed for each 16 $\times$ 16 $\times$ 16-voxel window, leading to about 5 windows along the optical access and thereby a modest total reconstruction volume depth of about 8 mm.

Generally, the maximum PPP could be increased by using more cameras. The configuration of the cameras would also make a difference. [25] reports that the aperture angle of the cameras should be at least larger than 60 degrees for a optimum reconstruction, otherwise the "particle elongation" effect would appear, corresponding to a low depth resolution. Here aperture angle is the measurement angle formed by the pair of cameras at the margins. Also, a "cross-like" configuration would yield more accurate reconstructions than a "linear" one with the same camera number and aperture angle. In a "cross-like" configuration, cameras look at the reconstruction volume from different heights, while in a "linear" configuration all cameras are at the same height (readers may refer to Figure 8 of [25] for a diagram of aperture angle and the

two configurations). In a practical flow device where optical access is limited, deploying a camera array with optimised angles to achieve a similar spatial resolution to single-plane PIV could be challenging, or likely impossible.

2.3.3 Simultaneous Multi-plane PIV Based on Polarisation and Wavelength

To acquire more out-of-plane information, while maintaining high in-plane spatial resolution of the measured velocity field, simultaneous multi-plane PIV has been attempted. Conventionally, measurement planes are distinguished by different laser polarisation directions or/and laser wavelengths [3, 31, 32]. An advantage of the polarisation and wavelength methods is that the measurement planes can be closely spaced, which allows the complete velocity gradient tensor to be measured within a plane. However, the number of measurement planes is limited by the wavelength/polarisation differences of the laser sheets. Orthogonal linear polarisations could allow a pair of planes to be distinguished. Further increasing the number of measurement planes means introducing more laser sheets with different wavelengths, which is costly and adds experimental complexity. To the best of the author's knowledge, quad-plane PIV is state-of-the-art [3].

2.4 Defocusing Method

In microscopic PIV (μPIV), where generally the thickness of the volume of interest is smaller than the thickness of a laser sheet ($\sim$0.5 mm), the entire flow volume is inevitably illuminated [33, 34]. Due to the finite size of the laser sheet, both in-focus particles on the nominal object plane and out-of-focus particles are illuminated and imaged. Michael G. Olsen and Ronald J Adrian [33] defined the Depth of Correlation (DOC) parameter as twice the distance from the object plane to the nearest plane in which a particle image becomes sufficiently defocused to no longer contribute sig-

nificantly in the PIV cross-correlation process. After making approximations such as modeling an optical system as a single thin lens, depth of correlation may be calculated [33, 35, 36]. Inevitably, in many practical μPIV implementations, a deviation of the actual depth of correlation from its theoretically predicted value can be expected [34].

In μPIV, another routine to accommodate the effect of defocusing, is to perform 3D particle tracking velocimetry, by inferring particle depth based on their defocusing patterns (shapes) [37, 38]. In principle, this is similar to a tomographic reconstruction process in terms of its nature of solving an under-determined problem. Therefore, a similar issue on the particle number would be encountered.

The larger spatial scale involved in **macroscopic** PIV enables users to selectively choose a set of planes to illuminate, instead of mitigating against volumetric illumination as in most μPIV experiments. In macroscopic multi-plane PIV, only discrete classes of defocused particle images would appear, instead of a continuous range of defocused images as in μPIV. By leveraging a shallow depth of field, the interference from the out-of-focus images reduces drastically as the out-of-focus plane is further away from the plane of focus. In the past, Alexander Liberzon *et al.* [39] performed three-plane PIV by distinguishing particles at three depths (12.5 mm displaced) based on the particle shapes in the images, which restricted their application to a very low particle number. Before this thesis, [39] was the only application of defocusing-based macroscopic PIV (to the best of the author's knowledge).

For the first time, the author of this thesis leverages the defocusing-based macroscopic PIV method based on the DOC concept, aiming for a similar particle seeding density to typical single-plane PIV. In μPIV, it is assumed that velocity variation along the depth direction is small that the effect of the defocused particles on the PIV cross-correlation process is "nudging" the correlation peak of the in-focus particles. On the other hand, in macroscopic PIV, the "correct" correlation peak produced by the in-focus particles and the "wrong" correlation peak produced by the defocused particles can be at any location in the cross-correlation map, depending on the flow field. Therefore, the characterisation of crosstalk between in-focus and defocused particles

in macroscopic PIV needs to consider different combinations of "correct" and "wrong" peak locations.

2.5 Turbulent Flame Front Detection

Turbulent combustion is one of the most complicated physical phenomena in nature, which involves the coupling of fast chemical reactions, turbulent fluid dynamics, heat transfer and species transport. While turbulent combustion is a complex process, heat and kinetic energy released thereby are major sources of power for propulsion and electricity generation, making it important to study and understand its properties.

Recently, turbulent premixed combustion is of greater interest for industrial applications where low emissions are sought [1]. It is well-established that most premixed turbulent flames that have been studied to date are composed of wrinkled "flamelets" [40]. In the so-called flamelet regime, the thickness of the chemical reaction layer (flame front) is smaller than the Kolmogorov scale, which is the smallest turbulent scale in the flow [41]. The flame can be regarded as behaving similarly to the laminar case and described independently of the turbulent flow field. Fundamental parameters such as the flame surface density, flame brush thickness, and turbulent burning velocity are calculated based on the turbulent flame front [42]. These parameters are not only significant to a better understanding of the underlying mechanisms of turbulent premixed combustion, but also useful for directly validating computational models. The measurement of flame front position relies on laser based optical diagnostics techniques. The two common approaches employ Laser-induced Fluorescence (LIF) and PIV.

2.5.1 Laser-induced Fluorescence (LIF)

All molecules have a unique distribution of energy levels, corresponding to discrete rotational, vibrational and electronic frequencies of motion. Following exposure to

light at a specific wavelength corresponding to an absorption feature of the molecule, a transition of the molecule from a "ground state" to an "excited state" occurs. After photon absorption, excited molecules undergo a number of competing energy transfer processes to relax towards the ground state again. Fluorescence is one of these processes, which involves spontaneous emission of photons.

During combustion, intermediate short-lived radicals such as OH and CH are generated, which are typically used for marking the burned region [43, 44, 45, 46]. These radicals can be excited by specific wavelengths (e.g. 283 nm for OH, 390 nm for CH), and emit fluorescence photons, which can be imaged with a camera.

Conventional LIF imaging for flame front tracking is on a single plane. By exploiting the polarisation difference of light, two-plane LIF of a certain radical could be performed [47]. Simultaneous two-radical tracking could also be achieved by using two wavelengths [46]. For three-dimensional flame front reconstruction, volumetric LIF imaging based on multi-camera tomographic reconstruction was attempted [48, 49].

2.5.2 PIV (for Flame Front Tracking)

Due to the large temperature change between the unburned and burned regions, a sharp number density gradient of the PIV seeding particles can be detected at the region boundary. Therefore PIV was used as a low-cost and reliable alternative for flame front detection, and has been applied widely [50, 51, 52, 53, 54, 55]. Besides, the PIV method can achieve simultaneous measurement of flame front position and flow velocity field, enabling a relatively simple determination of flow-flame interaction without needing an additional LIF system [52, 53].

In principle, radicals such as OH and CH are post-flame species (slightly towards products), while the region boundary measured by PIV is in the preheat layer (slightly towards reactants). As illustrated in Fig. 2.9, the offset between PIV and LIF measurement is mostly dependent on the magnitude of the reaction zone thickness and the preheat zone thickness. In the flamelet regime, the preheat zone plus reaction

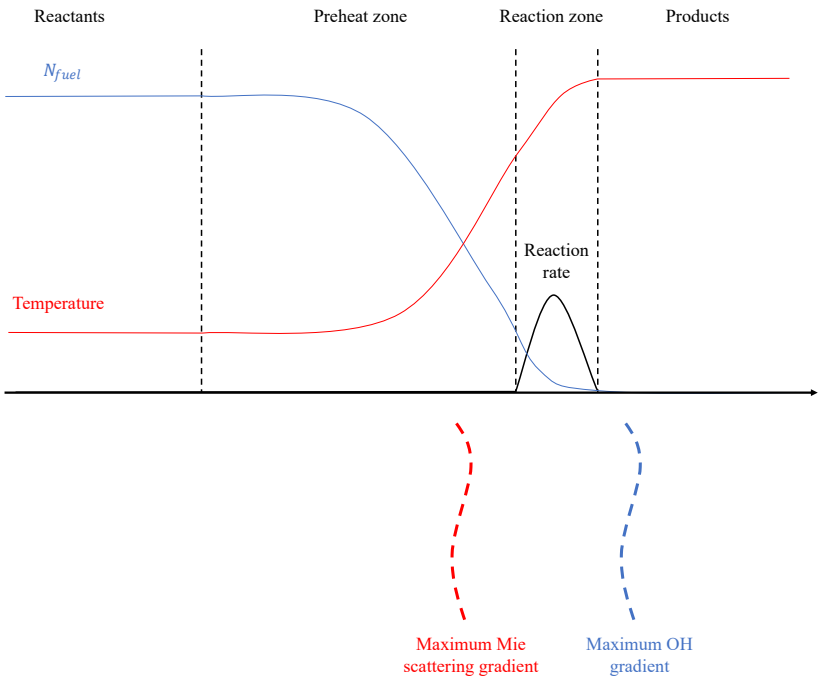

Figure 2.9: Illustration of the offset between flame front measured by PIV and OH LIF.

zone thickness is smaller than the Kolmogorov scale, such that the small eddies of the Kolmogorov scale do not penetrate the flame. Recently, Yi Gao *et al.* simultaneously used OH LIF and PIV to measure the flame fronts of premixed dimethyl ether (DME)/air flames stabilized on a two-dimensional bluff body [51]. The comparison between OH LIF images and PIV images indicate that the flame front curvature distributions measured using the two techniques match very well in all working conditions studied. When the flame is stable (with an equivalence ratio ranging from 0.8 to 0.7), the displacements between OH LIF flame fronts and PIV flame fronts are less than 1 mm. They pointed out that as the flame approaches lean blow-off and becomes unstable (with an equivalence ratio of 0.65), the displacements between OH LIF flame fronts and PIV flame fronts are two times larger on average, and could be up to about 4 mm. The applicability of the PIV method for flame front tracking at unstable conditions and very lean conditions is worth further investigation.

Due to the discrete nature of particle images, window-based methods are typically

used for evaluating combustion PIV images and generating flame front contours. To study the spatial resolution of the combustion PIV method, Yutao Zheng *et al.* compared simultaneous PIV and OH PLIF measurements of flame fronts in a low turbulence Bunsen fame [54]. They found that once the seeding density and window size are well-tuned so that the average measured number density in each window converges and does not vary with increasing window size, the average spatial differences between Mie scattering images and OH-PLIF images are of the order of or smaller than the laminar flame thickness. They also showed that the different window sizes make minor differences to the spatial locations of the measured flame fronts, but could make noticeable differences to the measured smoothness (curvatures) of the flame fronts.

Similar to multi-plane flow velocimetry, multi-plane flame front detection based on PIV was achieved by exploiting the polarisation and wavelength difference [56]. In [56], three-component quantities such as curvature and flame displacement speed were evaluated on a premixed methane flame on the intersection line of four crossing laser sheets. Dominik Ebi and Noel T Clemens performed a four-camera tomographic PIV and flame front reconstruction in a swirl combustor [57]. They measured a volume of about $30 \times 15 \times 4.5$ mm^3, with a voxel resolution about 0.064 mm. A sliding $16 \times 16 \times 16$ voxels^3 interrogation volume with 50% overlap was used to evaluate and mark the burned/unburned voxels, with an average seeding density of 12 particles in an interrogation volume in the fully unburned region. Similar to the simplified example in Section 2.3.2, such a tomography based reconstruction had to carefully balance the measurement volume size, particle seeding density and measurement accuracy, not to mention the optical access needed for deploying a camera array.

In this thesis, the first simultaneous two-plane and four-plane flame front detection using defocusing based PIV are demonstrated. Similar to defocusing based multi-plane velocimetry, this work explores the potential for increasing the number of measurement planes of current single-plane and multi-plane combustion PIV setups, while maintaining a similar seeding density and thus in-plane resolution to single-plane PIV. The two-plane and four-plane flame front detection in this thesis were performed in an op-

tical engine. As will be shown in the following chapters, a tomographic reconstruction based on camera arrays is not possible in those contexts, due to the limited optical access and space.

Because the defocusing approach takes advantage of the unique discrete characteristics of PIV, it is not suitable for LIF, which is a so-called "continuous field" measurement [26].

Chapter 3

Defocusing Based PIV With An Image Splitting Device

This chapter begins by introducing the design and alignment of the image splitting device, proposed for performing defocusing based macroscopic PIV on two planes using one camera. A laminar flow test was set up to systematically evaluate the three different types of measurement uncertainty caused by two-plane cross-talk. The evaluation was based on numerically adding in-focus images to out-of-focus images with different laminar flow profiles and at different plane separations. The contributions of each type of measurement uncertainty are quantified in Section 3.6. Approaches for mitigating the cross-talk are put forward, including using a new correlation peak search routine based on peak shape, and high-pass filtering the particle images.

The work in this chapter is published in [58]. All the raw data used in this chapter are openly available in the Oxford University Research Archive at [59].

3.1 Image Splitting Device

Fig. 3.1 presents the image splitting optics design. To allow images from two parallel depth-offset planes to be focused on a single camera sensor, a 2-inch 50/50 non-

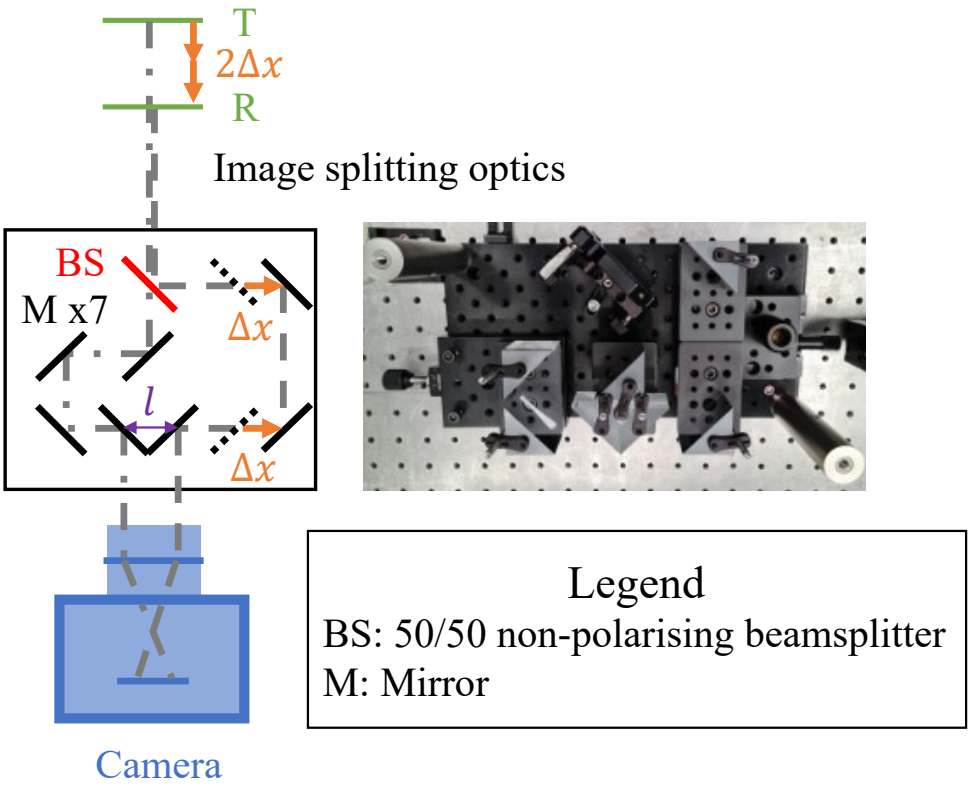

Figure 3.1: The image splitting device design.

polarising beamsplitter (Thorlabs BSW42-532) is used to split scattered light from the two planes into two paths, namely the transmitted-side path (T) and the reflected-side path (R). By using multiple mirrors, the light travelling along each path is directed to a different half of the camera sensor. Since light from either plane is 50/50 split into the two paths without bias, each half of the camera sensor receives light from both planes. In order to distinguish images from the two planes, the optical path lengths of the two paths can be adjusted independently: although both optical paths share the same camera lens and image distance, by adjusting the positions of the mirrors (Δx in Fig. 3.1), the two parallel planes can be placed at different depths along the optical axis and have an adjustable separation ($2\Delta x$ in Fig. 3.1). Therefore, for either side of the camera sensor, the image from one plane is in-focus, while the other plane's image is out-of-focus. By using a large aperture camera lens ($f = 85$mm, $f/2$, in this thesis), a shallow depth of field is achieved.

Due to image overlapping, the maximum width of the field of view on the two

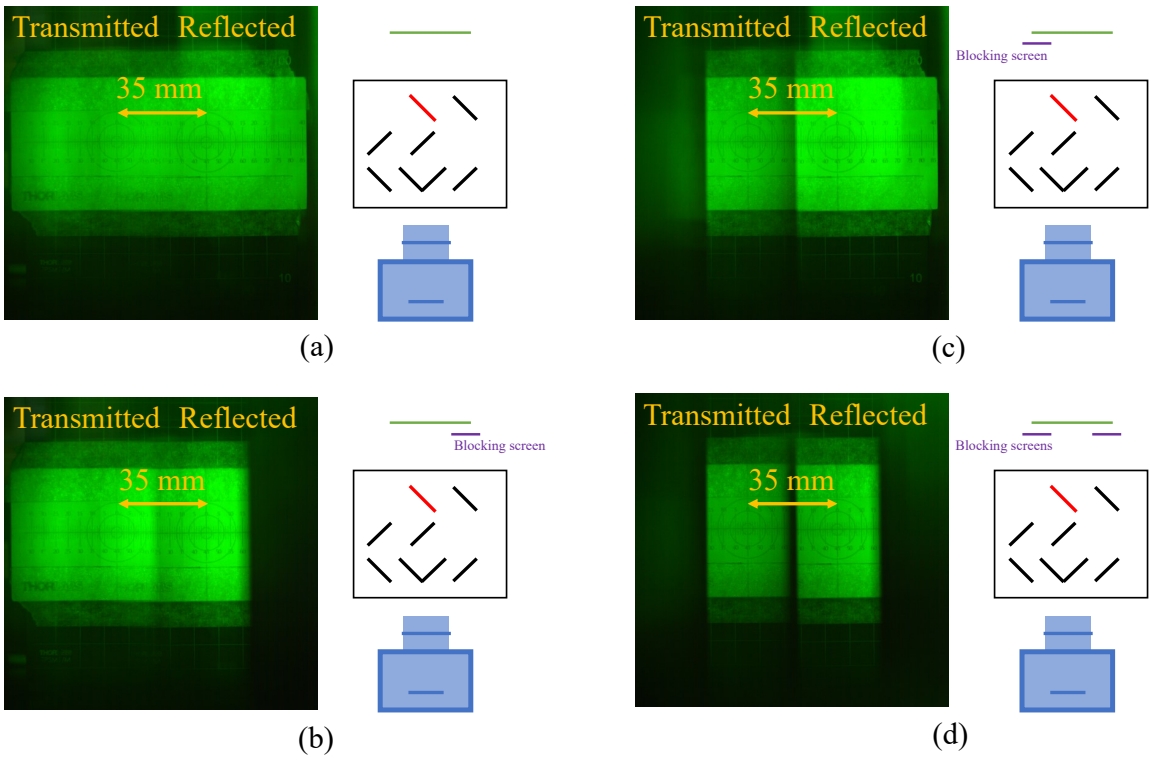

Figure 3.2: An example of image overlapping caused by image splitting. The four images were taken from the same ruler card with: (a) no screening; (b) a screen blocking from the right; (c) a screen blocking from the left; (d) two screens blocking from both sides. By changing the working distance of the camera, one is able to adjust how many pixels are used on each side of the view (i.e. to control the width of the "black regions" on the margin). The physical distance between the centres of the two views (35 mm in this work) is limited by the optics size.

measurement planes is determined by the distance (l in Fig. 3.1) between the centres of the two mirrors closest to the camera lens. That distance determines how far the two images on each side are separated. Fig. 3.2 shows an example of the image overlapping issue. Fig. 3.2 shows four images of the same ruler card, which was illuminated by a green LED from above. Fig. 3.2 (a) was taken without using any blocks. Fig. 3.2 (b) was captured when the view was blocked by a screen approaching from the right. Fig. 3.2 (c) was when the view was blocked by a screen approaching from the left. Fig. 3.2 (d) was when the view was blocked by two screens. By changing the working distance of the camera (i.e. how close the camera is to the region of interest), one is able to adjust how many pixels are used on each side of the view (i.e. to control the width

of the "black regions" on the margin), thereby the pixel resolution of the measurement. However, the physical distance between the centres of the two views is limited by l. In this work, since 35 mm×35 mm prism mirrors (Edmund Optics 49-406) are used, the width of the field of view is set to be 35 mm, the maximum with this setup. In Fig. 3.2, the pair of screens was positioned very close to the ruler card, so the distance between the left edge of the right screen and the right edge of the left screen was about 35 mm. It is also noted that in Fig. 3.2 (c), there is some background light on the left of the transmitted image, and the contrast between the two-side images in (b) and (c) are different. These should be because in this demonstration imaging setup, the stray light was not minimised. As will be shown later, when used for flow/flame measurements, the image splitting device was carefully enclosed to remove the contributions from stray light.

Because of image overlapping, in a real PIV experiment using this device, the field of view needs to be cut. There are three ways for cutting the field of view. One is to control the widths of the laser illuminated regions on the measurement planes, by sending the laser sheets vertically instead of on the same horizontal plane where the image splitting optics is placed. This method is applied in Chapter 4, 5 and 6. In an experimental setup where optical access is limited and the laser sheets cannot be sent vertically, two blocking screens can be used to narrow the illuminated region seen by the camera sensor, as indicated in Fig. 3.2 (d). This method is applied in this chapter. The third approach is to arrange the image splitting optics in such a way that the images are split in the vertical direction.

The image splitting based PIV method can be extended to stereoscopic measurement. As discussed in Section 2.2, stereoscopic PIV recovers the out-of-plane component by calibrating the parallax of two cameras looking at the same measurement plane in a stereoscopic configuration. In practice, because the cameras are tilted (typically by 15 to 45 degrees) relative to the measurement plane, the object plane of each camera is tilted as well. If the depth of field of the imaging setup is not deep enough, a part of the image would be significantly defocused. The way to overcome this problem is to

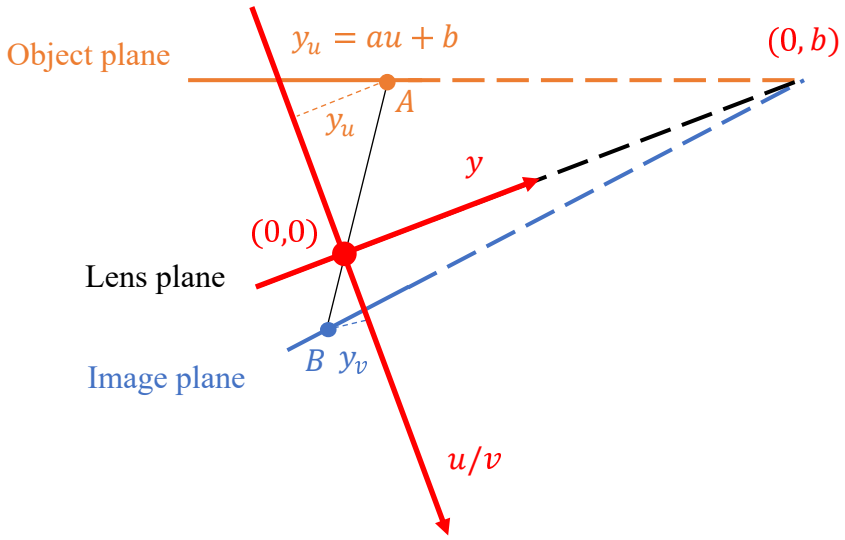

Figure 3.3: The Scheimpflug condition.

use a Scheimpflug adaptor which independently controls the tilting of the camera lens, so that the object plane (i.e. the measurement plane), the lens plane, and the image plane (i.e. the sensor plane) intersect at a single point. Fig. 3.3 shows the Scheimpflug condition for stereoscopic imaging. In Fig. 3.3, the y axis is attached to the lens plane, and the u/v axis is on the optical axis. To begin with, we have the equation of the object plane:

$$y_u = a\,u + b\ (u \leq 0), \tag{3.1}$$

in which a, b are constants. According to the thin lens equation:

$$\frac{1}{f} = \frac{1}{-u} + \frac{1}{v}, \tag{3.2}$$

we have:

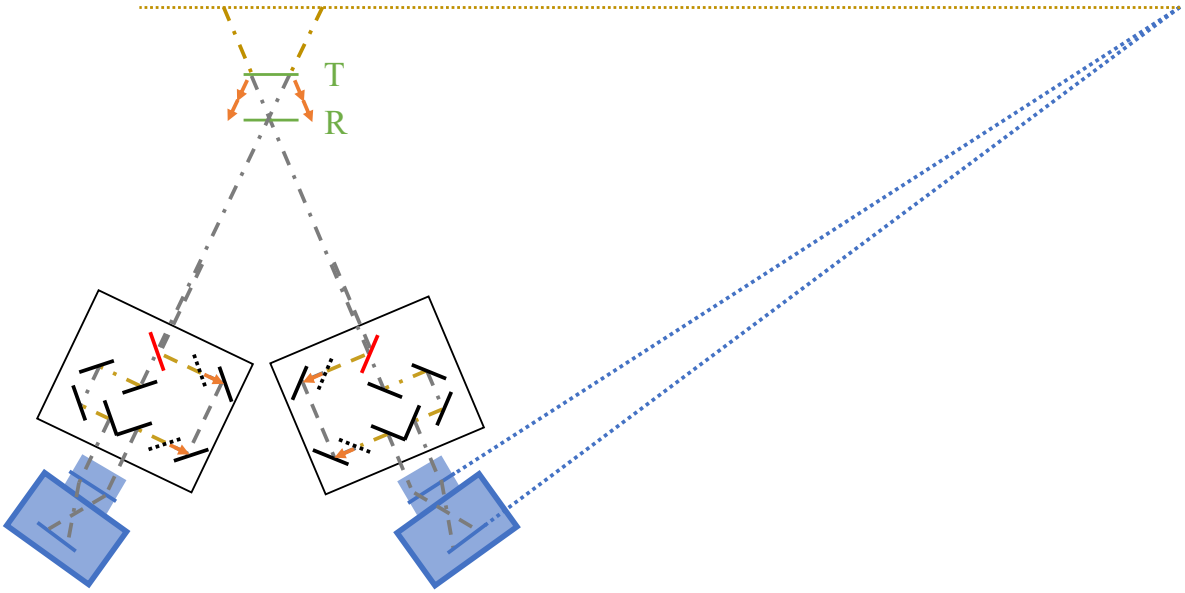

Figure 3.4: Two-plane stereoscopic PIV based on the image splitting device.

$$y_u = a\,\frac{f\,v}{f-v} + b. \tag{3.3}$$

The magnification ratio can be calculated by:

$$m = \frac{-y_v}{y_u} = \frac{-v}{u} = \frac{v-f}{f}. \tag{3.4}$$

Based on Equation 3.4, the image plane equation is derived:

$$y_v = (a - \frac{b}{f})\,v + b\ (v \geq 0), \tag{3.5}$$

which intersects with y_u at point $(0,b)$. This indicates that the Scheimpflug condition is inherently a requirement that the object plane and the image plane locations satisfy the thin lens equation.

Fig. 3.4 demonstrates the application of the image splitting device for two-plane stereoscopic PIV. Because the two object planes of the transmitted-side and the

reflected-side images actually have the same total distance to the camera lens, a camera lens with a Scheimpflug adaptor can bring objects on the two parallel object planes into sharp focus simultaneously. That means two-plane stereoscopic PIV is feasible in principle. But it is also worth pointing out that due to the different view angles of the two camera systems, the effective field of view on the two planes will be further limited. As an estimation of the limiting field of view effect, consider a two-plane stereoscopic measurement with a 15 mm plane separation and a camera tilting angle of 15 degrees (using the same image splitting optics), the effective field of view will be reduced from 35 mm to 31 mm. About two-plane crosstalk, Equation 2.1 suggests that the out-of-focus crosstalk error of the out-of-plane component should consist of two parts: the crosstalk errors of the in-plane components, and the uncertainty caused by camera calibration and linear equations solving. This chapter focuses on quantifying the measurement accuracy of two-plane two-component PIV. Questions about whether the uncertainty caused by camera calibration and linear equation solving would significantly increase the measurement error of the out-of-plane component are worth investigating in future.

3.2 Construction and Alignment

The image splitting device is built on top of a Thorlabs 150 mm × 300 mm × 12.7 mm aluminum breadboard (MB1530/M), which makes it a compact and readily portable device to pair with different cameras in different experiments. Fig. 3.5 presents a closer look of the device. The 50/50 beamsplitter is mounted using a Thorlabs KM200 kinematic mirror mount. Due to the limited space, a Thorlabs Mini Series clamping fork MSC2 and a Thorlabs 12 mm pedestal post (TRP14/M) are used to hold the KM200 mount. Two Thorlabs dovetail 50 mm translation stages (DTS50/M) are used for adjusting the prism mirror positions (i.e. the optical path length on the two light paths). In the whole setup, the seven prism mirrors sit on top of four Thorlabs 50 mm × 75 mm × 9.5 mm breadboards (MSB5075/M). The prism mirrors are mounted

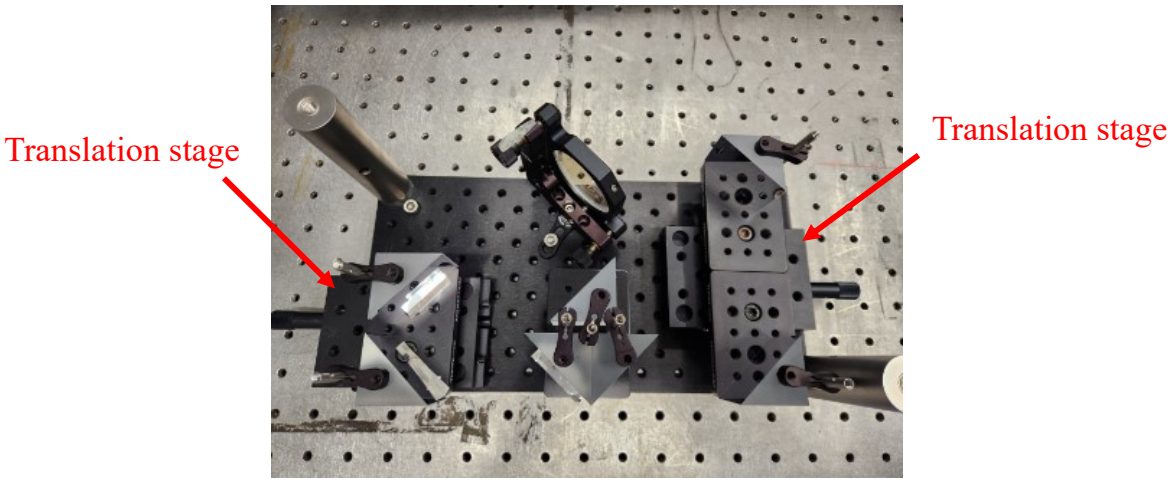

(a)

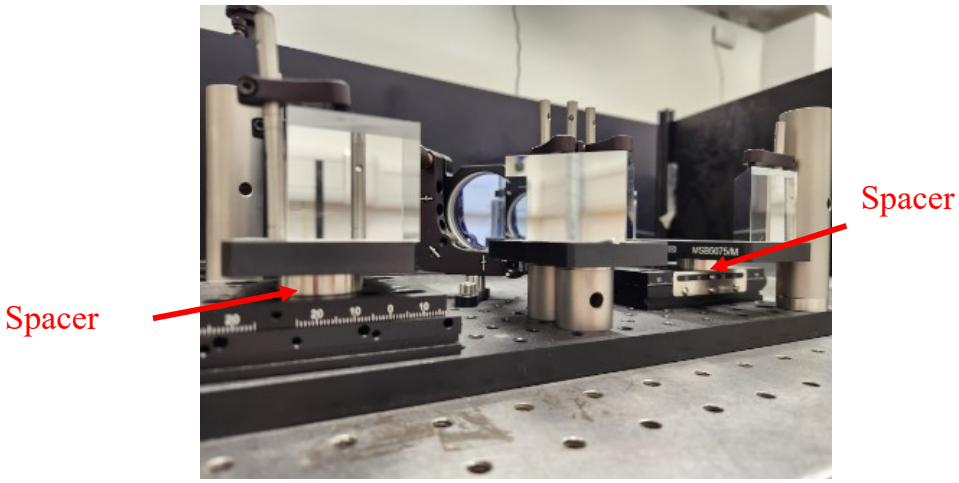

(b)

Figure 3.5: The image splitting device hardware, view from (a) top and (b) side.

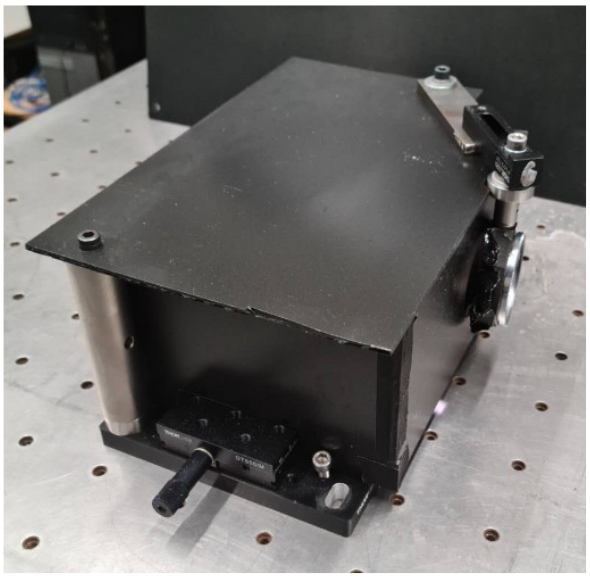

Figure 3.6: The image splitting device enclosed.

using Thorlabs PM3/M prism mounts. The height of the optical centre is 54 mm above the base board, defined by the height of the KM200 kinetic mirror mount and the TRP14/M pedestal post. To make the centre of each optic on the same height, spacers and posts with different heights are used accordingly. The two big posts mounted at the margins of the 150 mm $\times$ 300 mm base board provide supports/mounts for any protective screens or external components. As shown in Fig. 3.6, the image splitting device can be made into a compact "box" pairing for any typical camera in different test environments. The box shown in Fig. 3.6 was used in Chapter 4, 5 and 6. The protective screens prevent engine oil and dust from contaminating the optics. In Chapter 4, the circular mount at the front of the box was used for a 2-inch plain window, to protect the optics from oil and dust. In Chapter 5 and 6, it was used to mount a dichroic filter, which will be discussed at that point.

The alignment of the optics was performed by using a Thorlabs CPS532-C2 532 nm laser diode module (hereafter "laser pointer"). The laser pointer was mounted

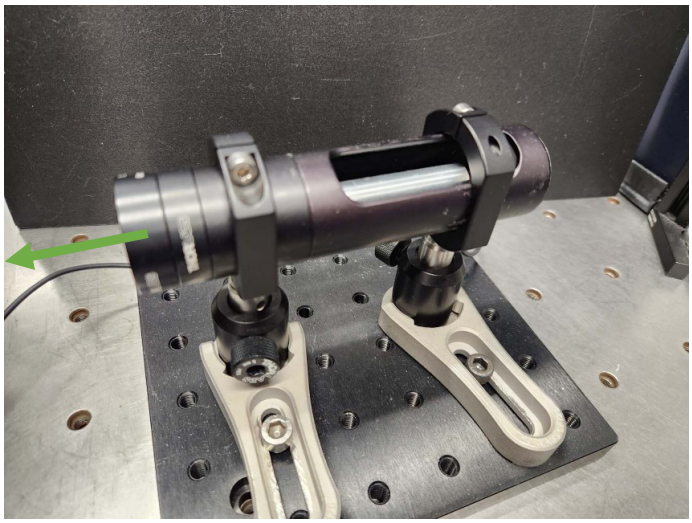

Figure 3.7: The Thorlabs CPS532-C2 laser diode module (hereafter "laser pointer"), mounted using Thorlabs one-inch kinematic adapter, lens tube and slip rings.

using a Thorlabs one-inch kinematic pitch/yaw adapter (KAD11NT). The laser pointer and the adapter were then mounted as a whole in a one-inch lens tube and one-inch slip rings (SM1RC/M) with posts (see Fig. 3.7). An absorptive neutral density filter (NE03A-A) and a frosted glass alignment disk (DG10-1500-H1-MD, 1 mm aperture) were mounted in front of the laser pointer to restrict the power and size of the laser beam to an appropriate level for alignment. The setup for the splitting optics alignment is shown in Fig. 3.8. There were two goals to achieve in the alignment process. The first was to make sure the laser beam was at the centre of every optic. For that purpose, two alignment masks were created by drawing the shapes and centroids of the 2-inch beamsplitter and the 35 mm prism mirrors on top of lens tissues (Fig. 3.9). The lens tissues are semi-transparent. By covering them on top of the optics surface, with the aid of the drawn boundaries, the author was able to align the optics' centre with the laser beam. The second goal was to make sure the laser beam was reflected by the correct angle. To achieve that, an alignment target was created by sticking a Thorlabs ruler card to a Thorlabs magnetic stand (seen in the upper right corner of Fig. 3.8 and

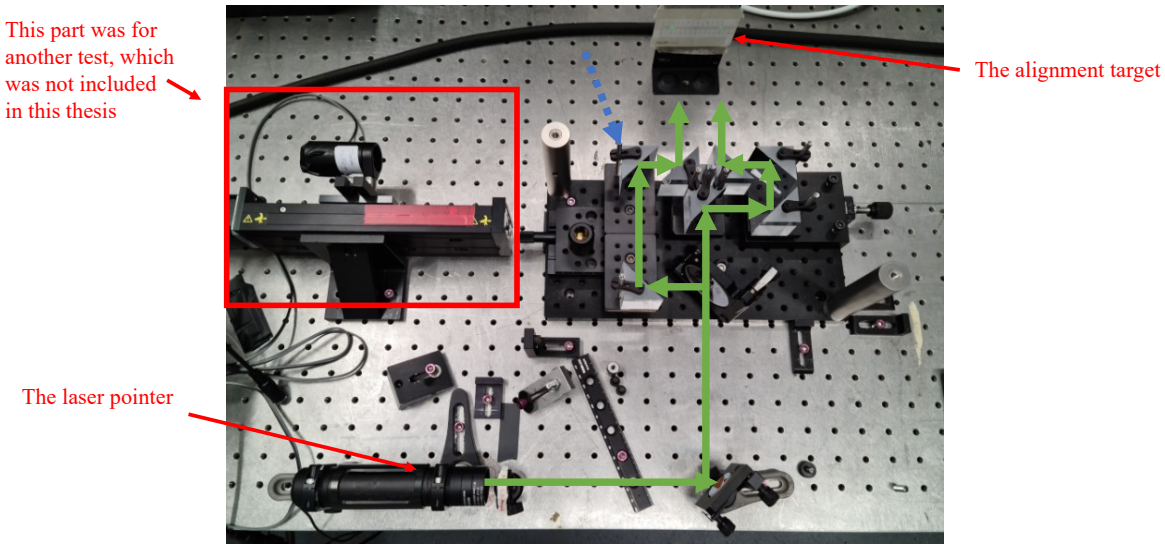

Figure 3.8: The setup for optics alignment. The blue dash arrow points at the prism of which the orientation could not be independently aligned.

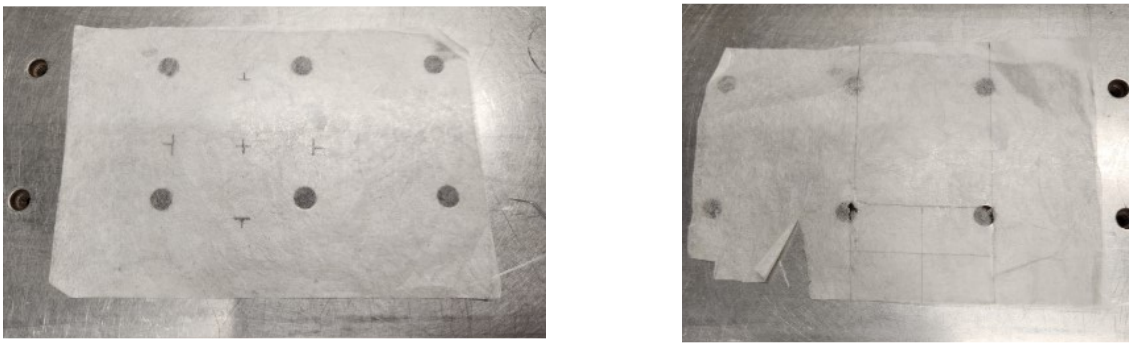

(a) (b)

Figure 3.9: The alignment masks created using lens tissues for: (a) the 2-inch beam-splitter; (b) the 35 mm prism mirrors. The boundaries and centroids were drawn using ruler and pencil.

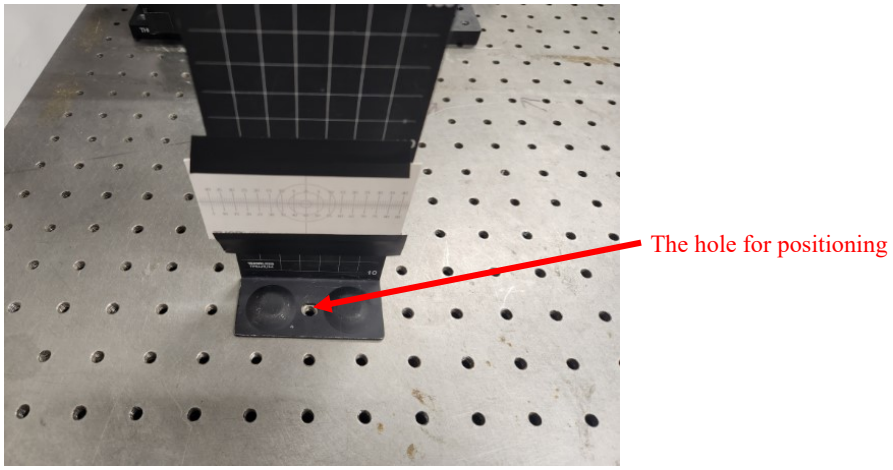

Figure 3.10: The alignment target for beam travelling (i.e. optics orientation).

in Fig. 3.10). In order to confirm whether the laser beam was travelling straight, the alignment target was moved along the optical axis (for ∼600 mm, limited by the optical table size), to check if the laser beam deviated from the original projection location. In this alignment, a beam location offset smaller than 0.5 mm (with ∼600 mm travel along the optical axis) was considered acceptable. This check was done separately for each optic for aligning their orientation, except one of the seven prism mirrors (marked by a blue dash arrow in Fig. 3.8) because the straight light path would be blocked by the other prisms. It was also confirmed that as the prism mirrors travelled along the 50 mm dovetail translation stages, the beam locations on the alignment target did not move by eye. As shown in Fig. 3.10, the positioning of the alignment target along the optical axis was done by checking if the mounting hole of the magnetic stand matched the M6 tapped holes (on the same line) on the optical table. This positioning was by eye, and the accuracy of the alignment was confirmed by the ruler card images in Fig. 3.2, showing a field of view width between 35 to 36 mm. The alignment target positioning method improved in Chapter 6, for the four-plane laser splitting optics, which will be discussed at that point.

When aligning the optics orientations, it was noticed that the laser beam would

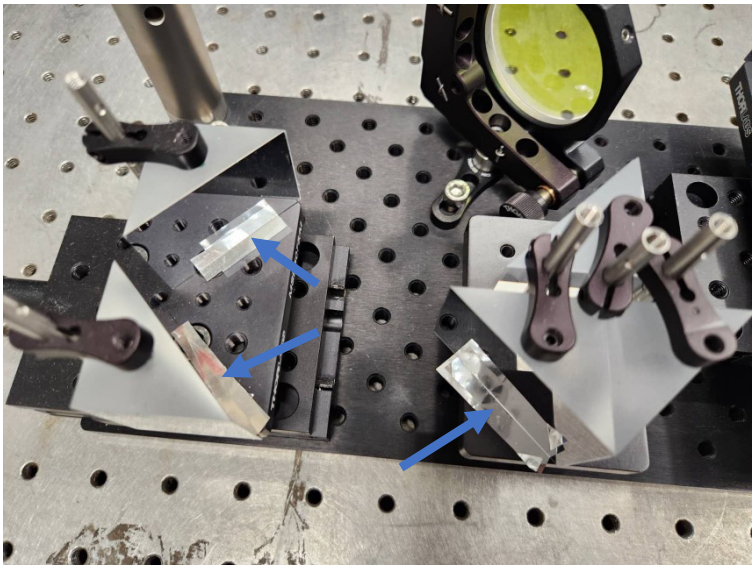

Figure 3.11: The thin mylar foils, indicated by blue arrows, put beneath some prism mirrors to address the vertical deviation of laser beam.

occasionally deviate vertically. This was caused by the non-flat surfaces of the prism mirrors and the bread boards where the mirrors sit. When the mirror was pinned down using the prism mount, a vertical orientation angle of the mirror could occur. To address that, very thin (3 to 27 μm) mylar foils were put beneath some prism mirrors, as shown in Fig. 3.11.

3.3 Experimental Setup for Accuracy Analysis

As discussed in Section 2.4, the crosstalk between in-focus and out-of-focus particles in macroscopic PIV is not only related to how blurry the out-of-focus particles become, but also influenced by the velocity difference of the two types of particles. To systematically study the two-plane crosstalk mechanism, a laminar flow rig test was performed. Fig. 3.12 and Fig. 3.13 present the test setup. A pair of coaxial laser beams was emitted from a dual-cavity Nd:YAG laser (Gemini 200-15, New Wave Re-

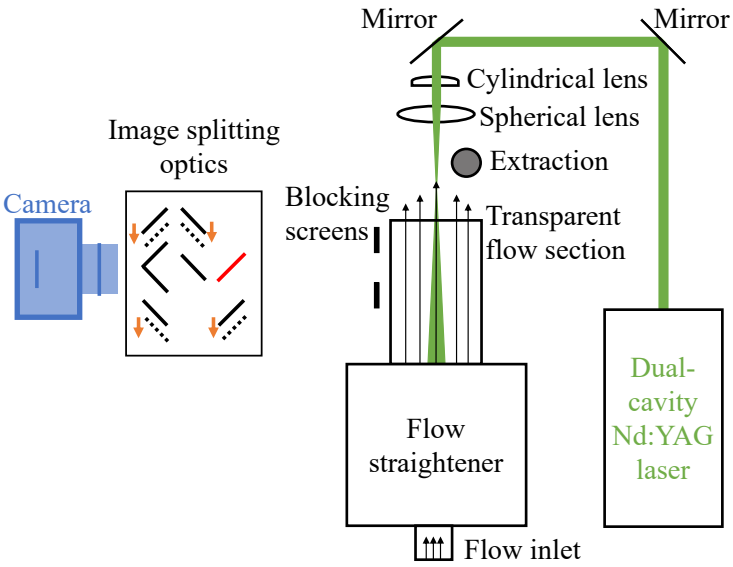

Figure 3.12: Plan view schematic of the laminar flow rig test (horizontal flow direction).

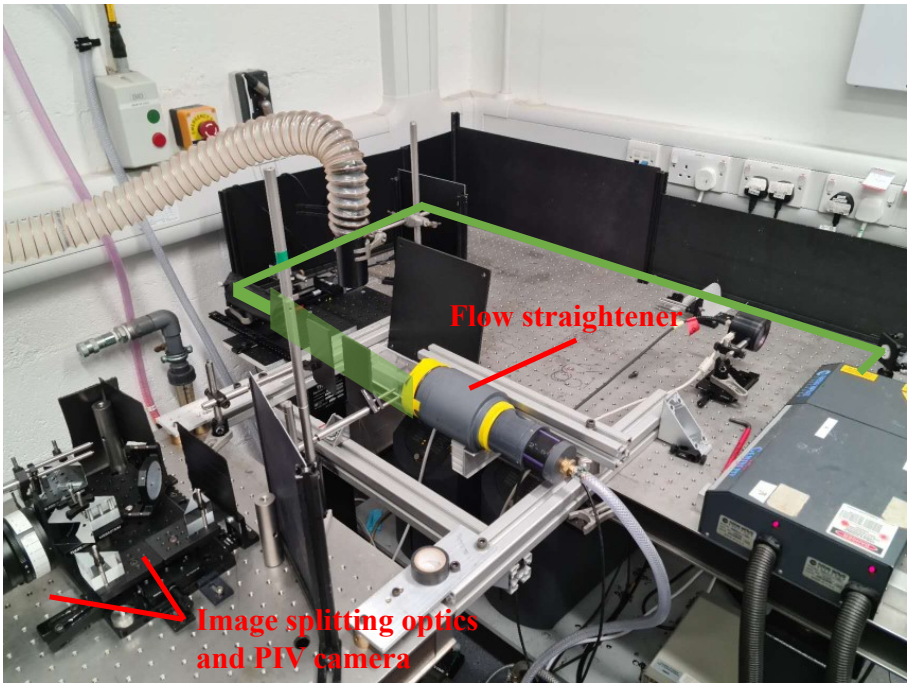

Figure 3.13: Experimental setup of the laminar flow rig test (horizontal flow direction).

Table 3.1: Nd:YAG laser specification.

Wavelength	532 nm
Maximum output power	100 mJ pulse energy (per cavity)
Repetition rate	Up to 15 Hz
Beam diameter	5.5 mm
Pulse width (Full width half maximum)	3-5 ns
Divergence (Full angle for 86% of the energy)	< 2 mrad
Beam Pointing Stability	< 200 μrad
Jitter	± 0.5 ns

search, see Table 3.1 for the specification). The light was directed through a telescope, formed by a $f = 60$ mm cylindrical lens and a $f = 350$ mm spherical lens, which expanded the beam from 5 mm to 35 mm in the vertical dimension, while focusing the beam to a thin sheet at the imaging area, which was the central plane of a rectangular section perspex tube (42×36 mm^2). Developing laminar air flow ($\mathrm{Re}_h = 160$) was generated by a flow straightener (Fig. 3.14) with circular micro channels (ϕ 0.85 mm, 1 mm spacing between each channel centre), and entered the perspex tube. The air flow was seeded with Di-Ethyl-Hexyl-Sebacate (DEHS) droplets (with a $\sim$0.4 μm mean diameter), generated by a LaVision aerosol generator (Fig. 3.15). The flow inlet system is shown in Fig. 3.16. Because the seeding particle number generated by the aerosol generator is largely determined by the inlet flow rate, an independent bypass with a separate mass flow controller (MFC) was employed to achieve independent control of total mass flow rate and seeding particle number. The flow rig can be placed horizontally or vertically to generate flows with different directions (see Fig. 3.13 and Fig. 3.17). As will be discussed later, measurement uncertainties of the horizontal (u) and vertical (v) components of flow velocity are different, due to the characteristic shapes of the out-of-focus particle images.

PIV images were taken by an Imperx B1621 double-frame CCD camera, with a large aperture camera lens ($f = 85$ mm, $f/2$) for a shallow depth of field. The double-frame mode of the camera enabled acquiring two images within a very short time between each other. The exposure duration for the first frame was adjustable, while

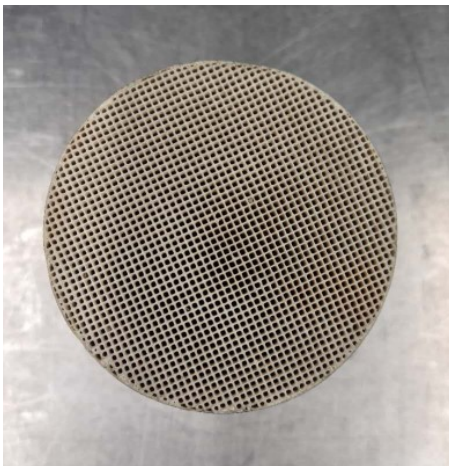

Figure 3.14: The flow straightener with circular micro channels (ϕ 0.85 mm, 1 mm spacing between each channel centre).

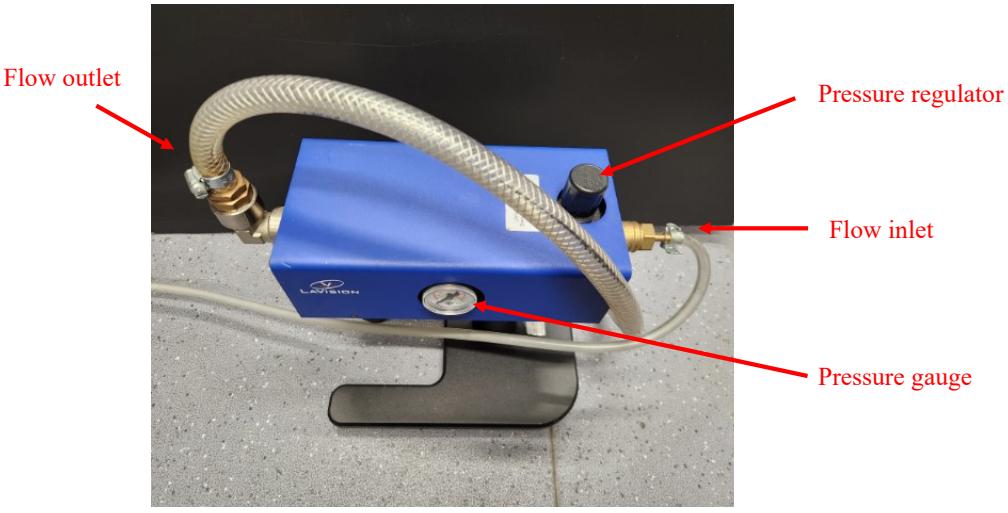

Figure 3.15: The LaVision aerosol generator. The pressure regulator is for coarse adjustment of the particle seeding number.

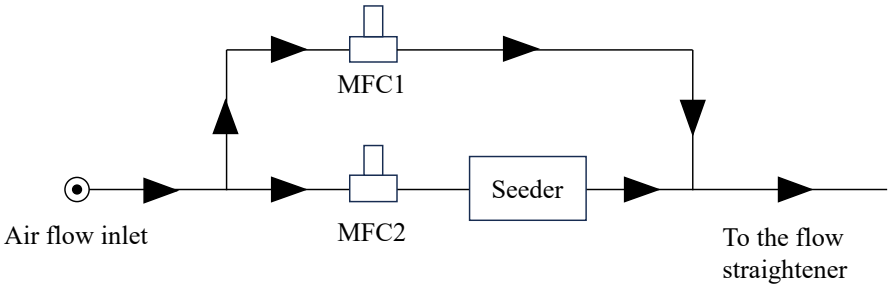

Figure 3.16: The flow inlet system.

Figure 3.17: The laminar flow rig with vertical orientation.

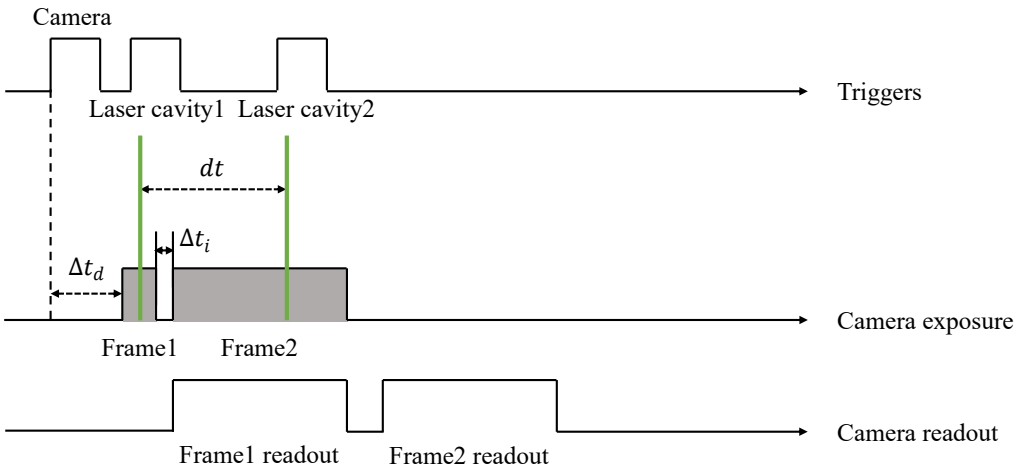

Figure 3.18: The timing diagram for laser and camera synchronisation. The inter-pulse time dt is determined by flow velocity. The fixed delay Δt_d between the camera trigger and the beginning of the first frame exposure is 11.4 μs. The fixed inter-frame time Δt_i is 200 ns. The exposure time for the first frame is adjustable. The second frame exposure depends on the time needed for reading out the first frame. The overall imaging rate of image pairs (33 per second for this camera) is determined by the time needed for reading out the second frame.

the second frame exposed for as long as it took to read out the first frame, with a fixed inter-frame time of 200 ns (Δt_i). A digital pulse delay generator (Berkeley Nucleonics 575) was used to synchronise the camera with the laser pulses. Fig. 3.18 presents the timing diagram for laser and camera synchronisation. There is an fixed 11.4 μs delay (Δt_d) between the camera trigger and the start of the first frame exposure. The inter-pulse time dt was determined based on the flow velocity, for optimisation of particle displacements on the images. The minimum inter-pulse time is the inter-frame time ($\Delta t_i = 200\ ns$) of the camera.

As discussed in Section 3.1, since the laser sheets travelled on the same horizontal plane as the image splitting optics, two blocking screens were used to narrow the illuminated region seen by the camera sensor. The field of view on each side of the image is 35 mm $\times$ 54 mm.

Table 3.2: Test variables in the laminar flow rig test. For the transmitted-side and the reflected-side image independently, 250 image pairs were collected at every combination of the test variables listed.

Flow direction	Plane separation/mm	dt/ms
Horizontal	0 (in-focus)	2.71 ($\sim$ 8-pixel displacement)
Vertical	10	2.32 ($\sim$ 7-pixel displacement)
	15	1.94 ($\sim$ 6-pixel displacement)
	20	1.55 ($\sim$ 5-pixel displacement)
	25	1.16 ($\sim$ 4-pixel displacement)
	30	0.77 ($\sim$ 3-pixel displacement)
	35	0.39 ($\sim$ 2-pixel displacement)
	40	0.19 ($\sim$ 0-pixel displacement)

3.4 Test Points

To evaluate crosstalk between the in-focus images and the out-of-focus images at different plane separations, the PIV measurement results of in-focus images are compared to the results of "two-plane" images, which were generated by **numerically adding in-focus images with out-of-focus images**, where "numerically adding" means that the pixel counts from individual images were added in Matlab. Different plane separations were achieved by translating the mirrors on the transmitted and the reflected optical paths of the image splitting setup (indicated by arrows in the image splitting optics drawing in Fig. 3.12). Crosstalk at different plane separations was studied respectively on the transmitted-side and the reflected-side image, since the out-of-focus particles have different shapes and degrees of defocus on the two sides, which will be discussed later.

Table 3.2 summarises the variables in the test. For the transmitted-side and the reflected-side image independently, 250 image pairs were collected at every combination of the test variables listed (with a 10 Hz repetition rate). In an actual PIV measurement, the laser pulse delay time dt within an image pair is fixed. Here, controlling dt is used to simulate flow fields with different flow velocities, while the laser energy and the particle seeding density remain the same. By numerically adding in-focus

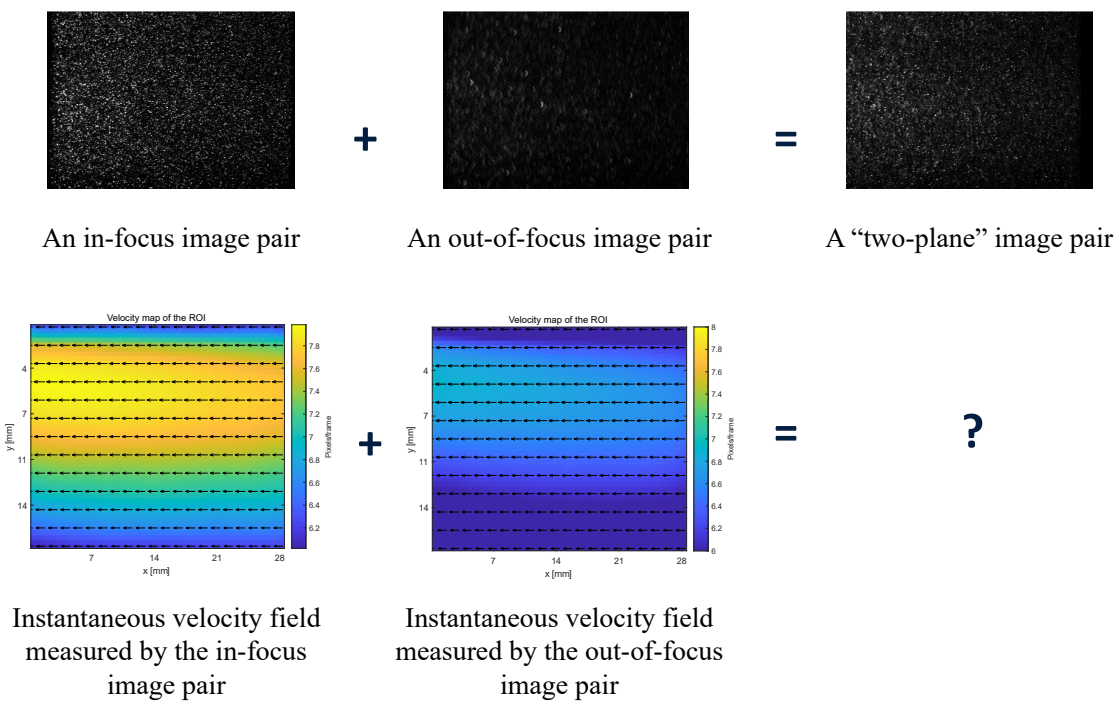

Figure 3.19: Illustration of the numerical addition of in-focus images to out-of-focus images having different particle displacements.

images with out-of-focus images having different velocities (particle displacements), different combinations of locations of the “correct” and “wrong” correlation peaks can be simulated (see Fig. 3.19 for an illustration).

PIV vector calculation was performed with a Matlab toolbox PIVlab (v2.56) [60]. A window deformation based multi-pass algorithm was applied, with a modified correlation peak search procedure to prevent outliers, which is discussed in detail in Section 3.6.2. Decreasing interrogation windows from 96 × 96 pixels to 64 × 64 pixels with a 50% overlap were used, resulting in a vector spacing of 1.4 mm. Here, the final interrogation window size was determined so that the particle image density is about 30 particles per final interrogation window, which is similar to the one in the engine flow measurements (Chapter 4). The PIV regions of interest are indicated in Fig. 3.20. The characteristics of the in-focus/out-of-focus particle images are discussed

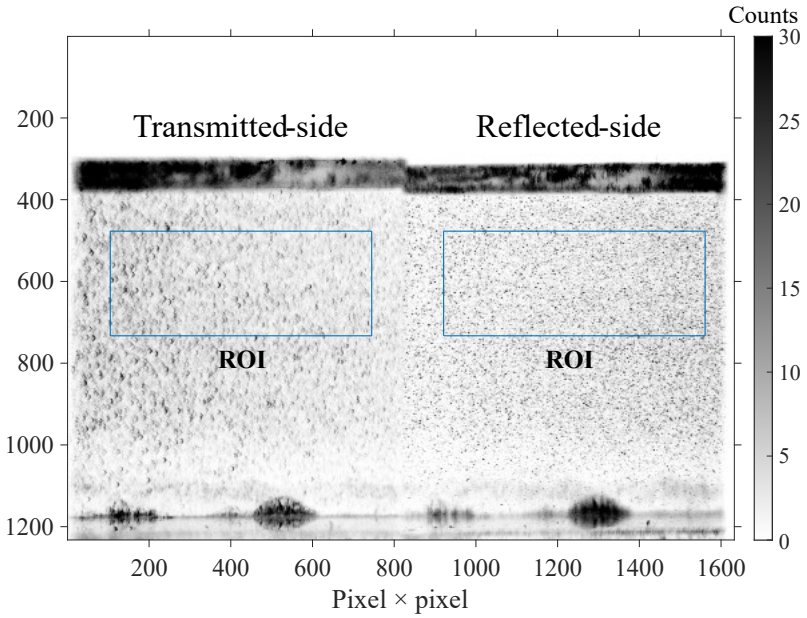

Figure 3.20: An example raw image (black and white inverted) in the horizontal flow test, overlaid with rectangles indicating the PIV regions of interest (ROI). In this image, the reflected-side image is in-focus, while the transmitted-side image is defocused, with a 15 mm plane separation. The horizontal bar along ∼340 pixels is scattered light from the flow section surface.

as follows.

3.5 Optical Characteristics of The Split Images

The degree of defocus of particles at different plane separations largely determines the measurement uncertainty. Fig. 3.21 shows examples of in-focus and defocused particle images in the PIV regions of interest. The particle images are black and white inverted, for a better visualisation of the particle image patterns. There are several observations we can make. Firstly, the out-of-focus particles have elliptical shapes, looking like arcs. This is due to each optical path using a half of the camera lens for imaging. Because the shape of the particle images largely determines the shape of the PIV cross-correlation peak, an asymmetric particle shape would result in the horizontal and vertical velocity component having different extents of crosstalk even at the same plane separation. Secondly, asymmetric defocus along the optical axis

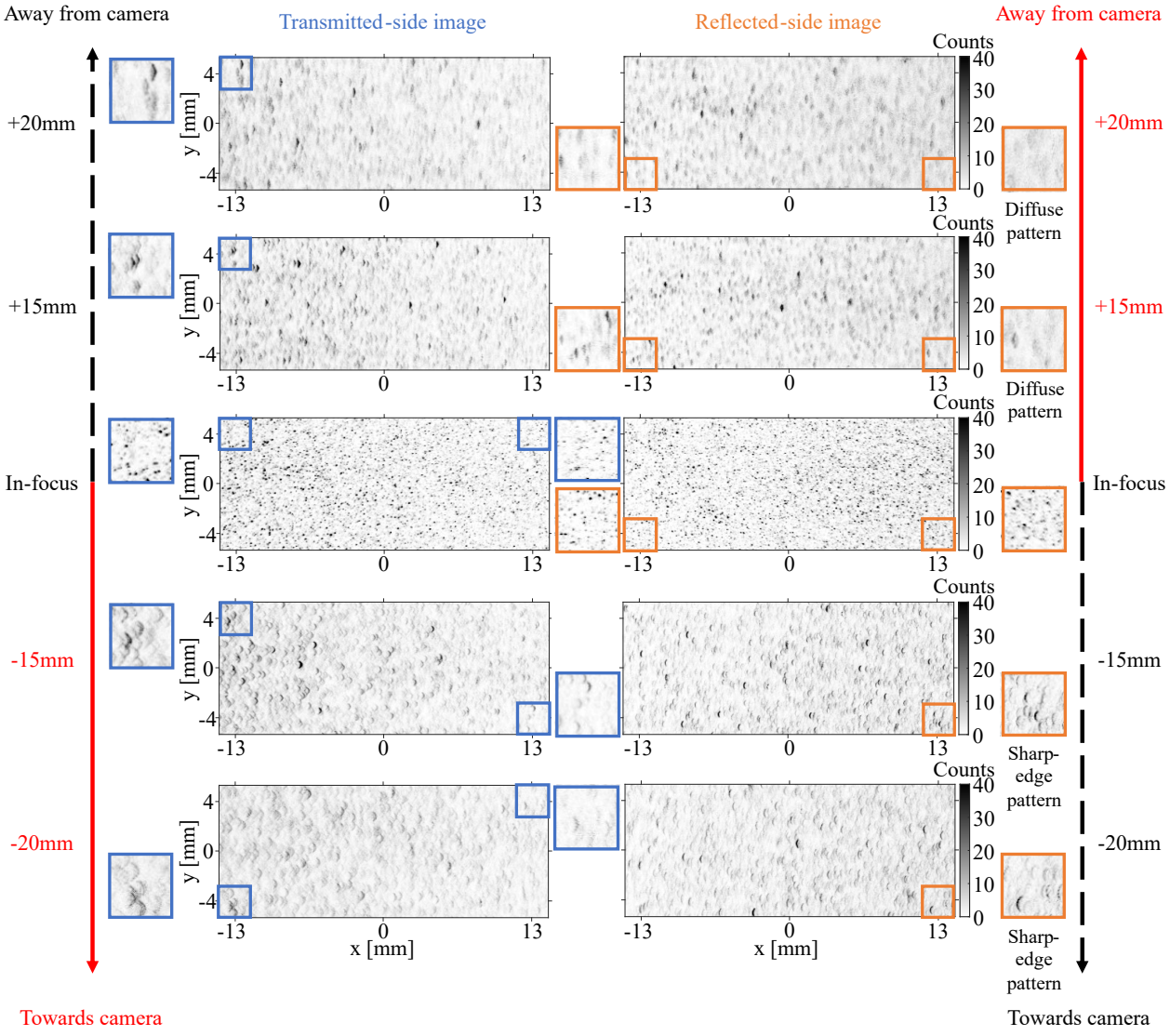

Figure 3.21: Examples of raw images (black and white inverted) in the PIV regions of interest.

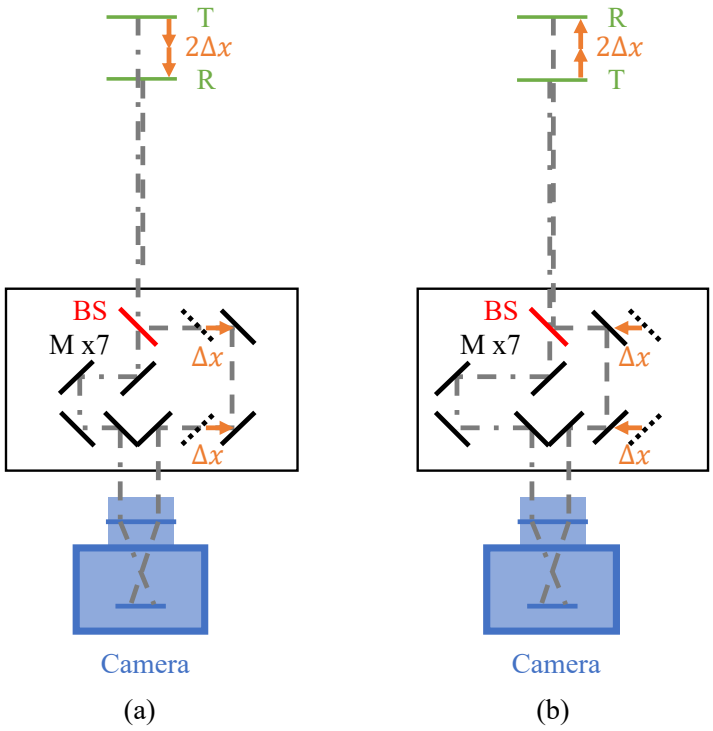

Figure 3.22: The two object plane configurations. (a) The object plane of the transmitted-side image is further away from the camera. This is the object plane configuration used for all tests in this Thesis. (b) The object plane of the reflected-side image is further away from the camera.

exists in either-side image, and it is more noticeable in the reflected-side image. This should be due to the asymmetry of optical aberration behind and in front of the plane of focus. For the reflected-side image, it can be noticed that when the out-of-focus particles are closer to the camera (i.e. the direction of the black dash arrow), the defocused particle images tend to have a distinct sharp-edged pattern, with intensity concentrated at their edges. The diffuse pattern on the other side of the plane of focus (i.e. the direction of the red solid arrow) is preferred, because diffuse particle images with spread intensity result in less sharp correlation peaks with lower height, which is beneficial for reducing cross-talk. Therefore, throughout this thesis, the object plane configuration has been chosen such that the transmitted-side measurement plane is further away from the camera lens, i.e. the setup (a) in Fig. 3.22).

Thirdly, it is also observable that the shapes of the defocused particle images are changing at different horizontal locations. It might be because for those particles

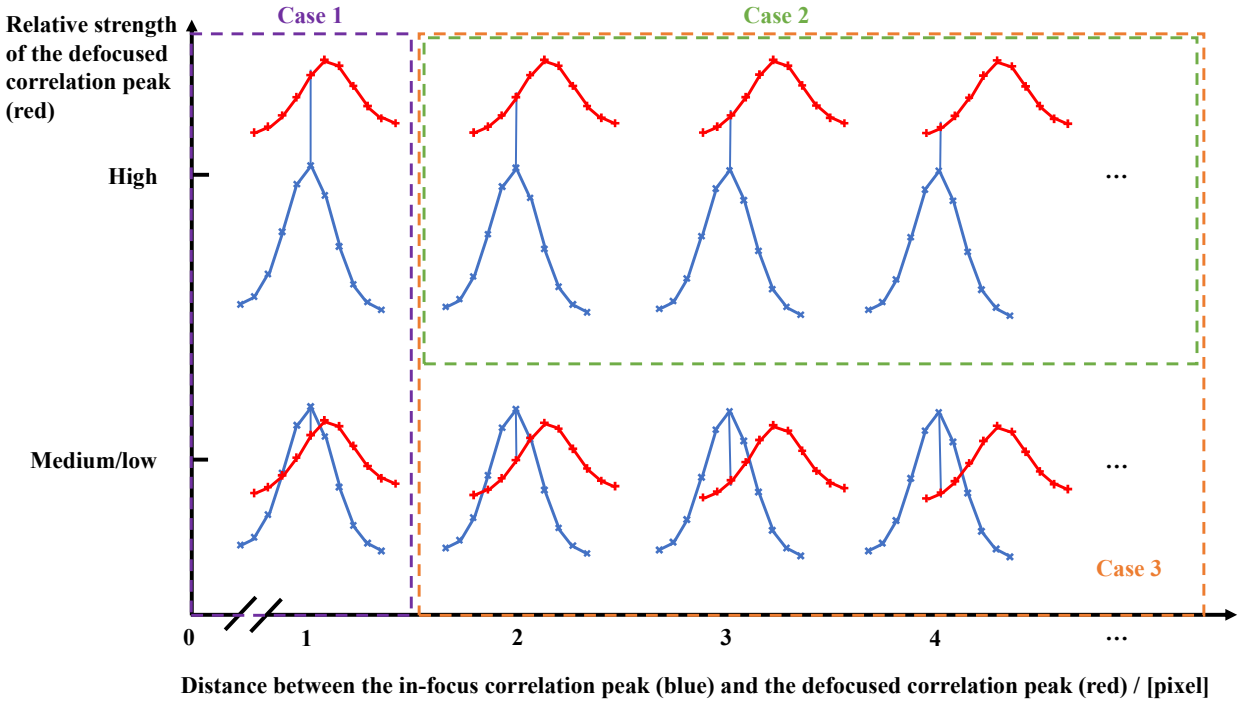

Figure 3.23: A principle sketch of the three types of measurement cross-talk. Case 1: the "correct" and "wrong" correlation peaks merge; Case 2: the "wrong" correlation peak has a larger height, leading to the PIV algorithm choosing the "wrong" peak; Case 3: the shape of the "correct" peak is changed, resulting in measurement uncertainty in terms of sub-pixel displacement estimation.

horizontally far away from the optical axis, the incident angle of light is large, leading to worse aberrations due to each optical path using only a horizontal half of the camera lens. The extent of such non-uniformity of defocusing might change if a different camera lens is used. In the measurement uncertainty analysis in Section 3.6, crosstalk at different horizontal locations will be discussed.

3.6 Uncertainty Sources

Fig. 3.23 summarises the three types of measurement crosstalk caused by the out-of-focus particles. In μPIV, velocity variation along the out-of-plane direction is assumed to be small, so that the "correct" and "wrong" correlation peaks "merge" into one, resulting in a mix peak biased towards the "wrong" peak (Case 1). This type of

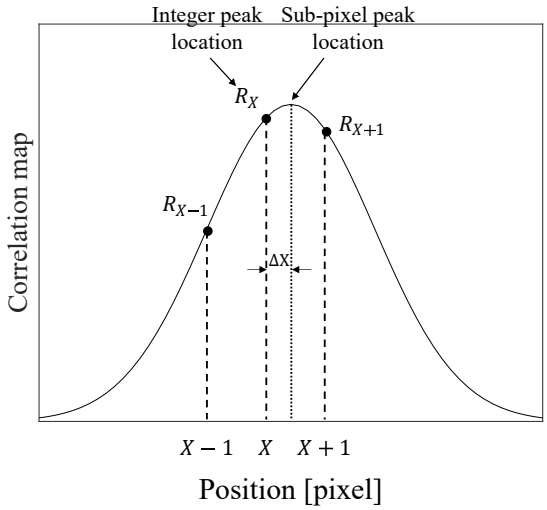

Figure 3.24: Principle of the Gaussian 2·3-point fit. Sub-pixel estimation is made based on fitting an one-dimensional Gaussian curve separately to the x and y axis of the cross-correlation function.

crosstalk can be modelled based on the curvature difference of the in-focus and out-of-focus correlation peaks.

In macroscopic PIV, different combinations of "correct" and "wrong" peak locations can occur. If bright/saturated out-of-focus particles exist within the interrogation window, a "wrong" correlation peak with a large height could be generated, so that a conventional correlation peak search routine based on maximum peak height search would pick the "wrong" peak (Case 2). This thesis proposes a cross-correlation peak search routine based on peak curvature to mitigate this issue. However, even if the "correct" correlation peak can be distinguished, its shape is still inevitably changed, having an impact on sub-pixel displacement estimation (Case 3). This is because PIV sub-pixel estimation is based on fitting two-dimensional or one-dimensional Gaussian functions using the peak pixel and its adjacent pixels [61]. For example, Fig. 3.24 shows the "Gaussian 2·3-point fit" method, which fits a Gaussian curve separately to the x and y axis using either the adjacent vertical or adjacent horizontal pixels of the correlation peak pixel. In the case of two-dimensional fitting, all the adjacent pixels are used together. The change of the correlation peak shape (i.e. relative

difference between peak pixel and adjacent pixels) would result in a change of sub-pixel measurement.

To better illustrate the three types of crosstalk, correlation maps from some interrogation windows in the laminar flow rig test are chosen as examples. The central rows of these maps are plotted in Fig. 3.25.

For a quick summary, being different from μPIV, macroscopic defocusing PIV encounters three types of measurement crosstalk. The first one, "peaks merging", dominants when the velocities of in-focus particles and out-of-focus particles are similar. The second one, "selecting wrong peak", could happen due to particularly bright out-of-focus particles. The third one, "peak shape change", describes the sub-pixel error caused by correlation peak distortion. The three cases will now be discussed in detail.

3.6.1 Correlation Peaks Merging (Case 1)

Uncertainty caused by peaks merging has been discussed and analysed in μPIV. The measured velocity can be seen as a weighted average of the velocities at different depths:

$$\boldsymbol{u_0} = \frac{\int \boldsymbol{u(z)} W(z) dz}{\int W(z) dz}, \tag{3.6}$$

in which $W(z)$ is a weighting function, quantifying the relative contributions of PIV particles at different depths. Bourdon *et al.* [62] proposed a method to experimentally measure the weighting function. It starts by recognising that the component of the overall correlation function related to the particle displacement is composed of the summation of individual correlation functions at each depth in the flow. In our case, finite depth is involved, and the correlation function R_D can be written as:

$$\langle R_D \rangle = \sum_{k=1}^{n} \langle R_D \rangle_k. \tag{3.7}$$

The overall measured velocity is at the location $\boldsymbol{s_0}$ where the slope of the overall correlation function is zero:

(a)

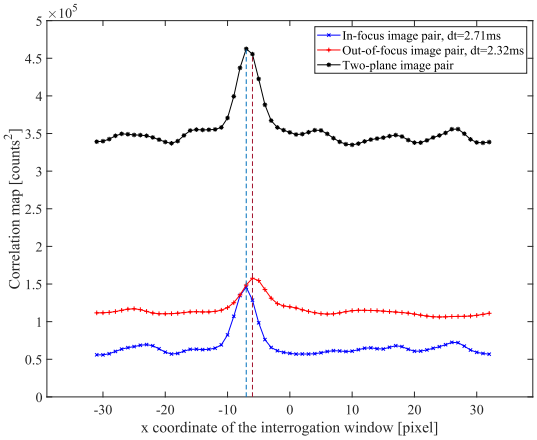

(b)

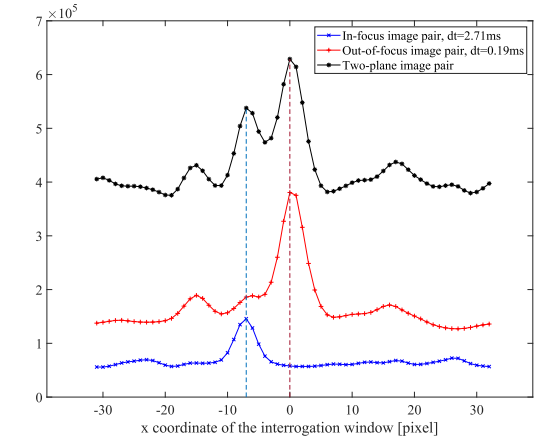

(c)

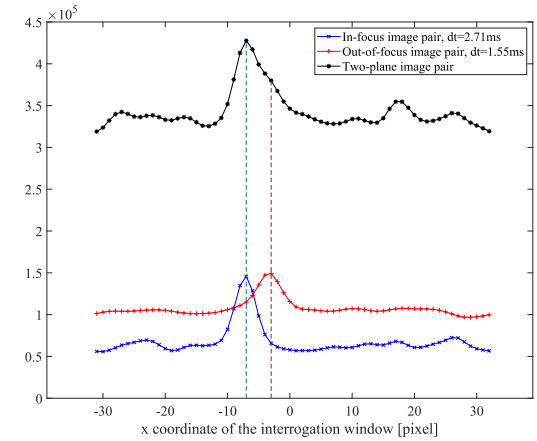

Figure 3.25: Examples of the central row of representative PIV cross-correlation maps, from the horizontal flow test, transmitted-side image, 15mm plane separation. (a) The "correct" and "wrong" correlation peaks merge (Case 1). (b) The "wrong" correlation peak has a larger height (Case 2). (c) The shape of the "correct" peak is changed (Case 3).

$$\frac{\partial \langle R_D \rangle}{\partial \boldsymbol{s}}(\boldsymbol{s_0}) = \sum_{k=1}^{n} \frac{\partial \langle R_D \rangle_k}{\partial \boldsymbol{s}}(\boldsymbol{s_0}) = 0. \tag{3.8}$$

By assuming that the location of the peak of each individual correlation differs from $\boldsymbol{s_0}$ by some small distance $\Delta \boldsymbol{s_k}$, the slope of each individual correlation function at the location $\boldsymbol{s_0}$ can be approximated by taking a Taylor series expansion around the location of each individual correlation peak:

$$\begin{aligned} \frac{\partial \langle R_D \rangle_k}{\partial \boldsymbol{s}}(\boldsymbol{s_0}) = \quad & \frac{\partial \langle R_D \rangle_k}{\partial \boldsymbol{s}}(\boldsymbol{s_0} - \Delta \boldsymbol{s_k}) \\ & + \frac{\partial^2 \langle R_D \rangle_k}{\partial \boldsymbol{s}^2}(\boldsymbol{s_0} - \Delta \boldsymbol{s_k}) \Delta \boldsymbol{s_k}. \end{aligned} \tag{3.9}$$

The first term on the right hand side of Equation 3.9 is zero, because $\boldsymbol{s_0} - \Delta \boldsymbol{s_k}$ is the location of the peak of each individual correlation. Substituting Equation 3.9 into Equation 3.8 leads to:

$$\begin{aligned} \frac{\partial \langle R_D \rangle}{\partial \boldsymbol{s}}(\boldsymbol{s_0}) = \quad & \sum_{k=1}^{n} \frac{\partial^2 \langle R_D \rangle_k}{\partial \boldsymbol{s}^2}(\boldsymbol{s_0} - \Delta \boldsymbol{s_k}) \Delta \boldsymbol{s_k} = 0 \\ = \quad & \sum_{k=1}^{n} W(z_k) \Delta \boldsymbol{s_k} = 0. \end{aligned} \tag{3.10}$$

Therefore Bourdon *et al.* [62] proposed that, by measuring the average curvature at the peak of the individual correlation function, the relative contribution of particles at each individual depth can be quantified.

In this test, the transmitted-side and the reflected-side images were divided into 64×64 windows with a 50% overlap. The correlation function of each window with itself has a peak at the centre. In our case, because the out-of-focus particle images have elliptical shapes, instead of being symmetric "circles" as in μPIV, the curvature evaluation was performed separately on the x and y axes. Two Gaussian functions

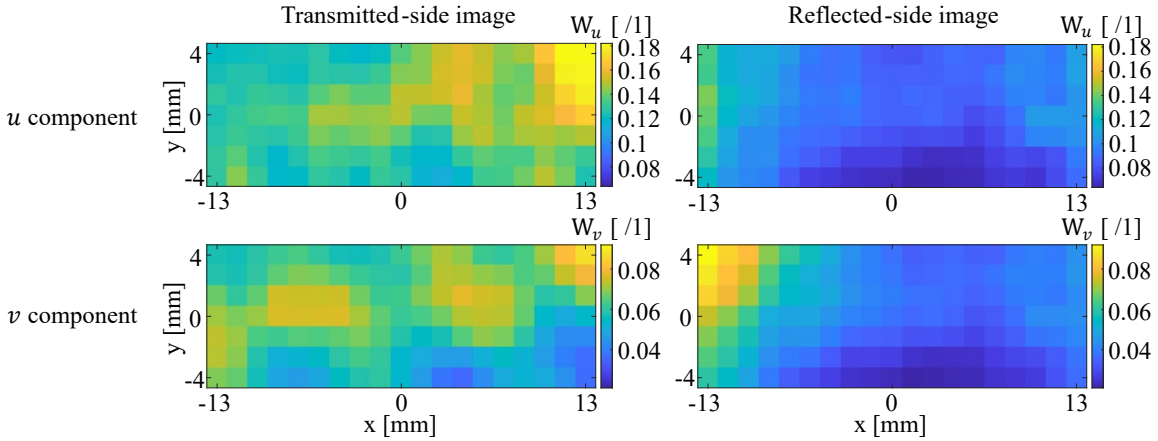

Figure 3.26: The weighting functions in the PIV regions of interest, at 15 mm plane separation. Note that the defocused particles closer to the centre of the camera sensor have larger weights. The colourbar scales of the u and v component are different, due to the non-circular shapes of the defocused particle images. The weighting functions are calculated based on 250 images.

were fitted respectively on the central row and the central column of the correlation function of each window. Curvatures were then calculated based on the fitted functions. For each interrogation window, the curvatures calculated based on 250 images were averaged and then used to calculate the weighting functions.

Fig. 3.26 shows the weighting functions calculated in the PIV regions of interest at the 15 mm plane separation. Differences in the weighting functions across the sensor width can be noticed: the out-of-focus particles generally have larger contributions in the central region of the camera sensor, due to the change of the defocused particle image shape at different horizontal locations (first shown in Fig. 3.21). The elliptical shapes of the defocused particle images lead to the measurement uncertainty of the vertical component being smaller, because the particle images are more "spread" along the y axis and more "concentrated" on the x axis.

Fig. 3.27 plots the weights of the defocused particle images in each interrogation window at different plane separations. Several observations need to be made. Firstly, even at the same plane separation, difference in the weighting functions of different interrogation windows can be noticed (as visualised in Fig. 3.26). It is also noticed that in the weighting function distributions of the reflected-side images (Fig. 3.27 (b)),

(a)

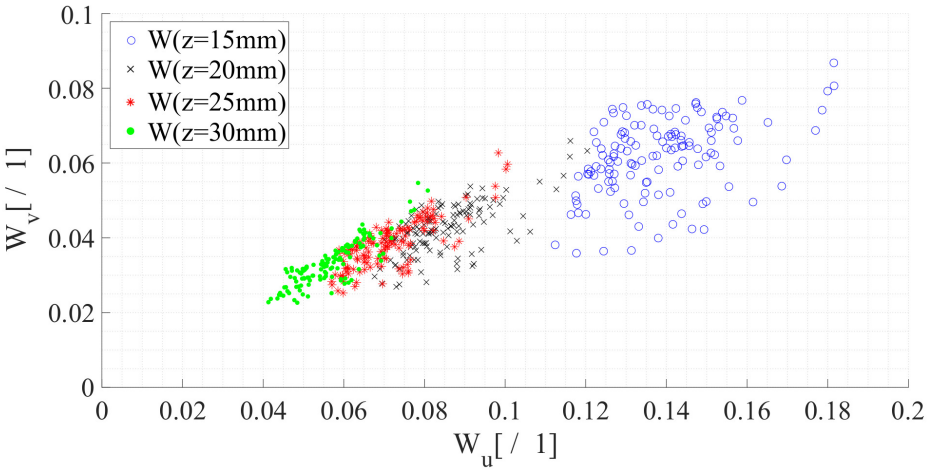

(b)

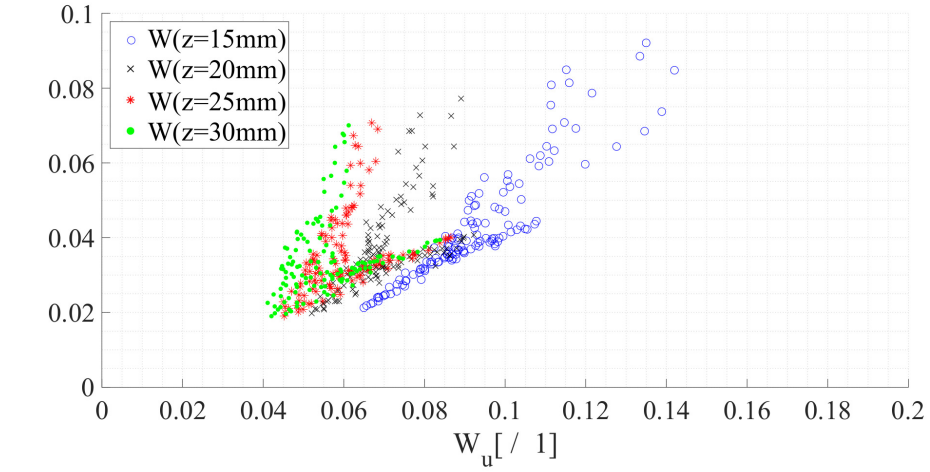

Figure 3.27: The weighting functions in the PIV regions of interest of the: (a) transmitted-side image; (b) reflected-side image. Each scatter point corresponds to one interrogation window.

there are trends which are more "vertical" in the plot, suggesting that the change of the out-of-focus particle shapes on the vertical direction in the images (i.e. the height of the "arc shapes") is larger in each individual reflected-side image. Secondly, the relative contribution of the defocused particles on the u component of velocity is larger, because of the characteristic arc shape of the defocused particle images. Thirdly, as the plane separation further increases, the reduction of the weights becomes slower. This indicates a limit of minimum cross-talk caused by "peaks merging". The limit should be dependent on the effective aperture size of the optical system, which limits the size of the out-of-focus particle images. However, since the weighting function calculation is based on the assumption that the "correct" and "wrong" correlation peaks are close to each other ($\Delta \boldsymbol{s_k} \rightarrow 0$), the absolute measurement error caused by "peaks merging" is actually limited. This will be shown by the PIV measurement results in Section 3.6.3.

3.6.2 Correlation Peak Search Based on Peak Shape: Outlier Removal (Case 2)

In PIV, seeding particles that have a diameter of the order of the wavelength of the incident light are used, so that strong Mie scattering is used for particle detection. The Mie signal is proportional to the square of the particle diameter. PIV particles generated by practical seeding devices have a certain size distribution, instead of being monodisperse. Therefore, in PIV images, some particles are brighter than others due to their sizes. The spatial distribution of the laser sheet intensity is another source of the brightness difference of particles, because a laser sheet has a finite thickness, generally having the peak intensity at the centre. As can be noticed in Fig. 3.21, although most of the defocused particles have weak intensities, some very bright blurry particles still occasionally appear.

Generally a PIV algorithm determines the statistical displacement of particles by searching for the maximum of the cross-correlation function. However, the correlation peak produced by bright out-of-focus particles can occasionally have a larger height,

resulting in outliers occurring.

Inspired by the curvature difference of the correlation peaks produced by the in-focus and the out-of-focus particles, the author has proposed a correlation peak search routine taking advantage of the correlation peak shape difference. When searching for the correlation peak, instead of directly choosing the peak with the maximum height, the location having the maximum directionally-averaged second derivative is picked:

$$(x_c, y_c) = \arg\max \frac{\frac{\partial^2 R(x_i,y_j)}{\partial x^2} + \frac{\partial^2 R(x_i,y_j)}{\partial y^2}}{2}. \tag{3.11}$$

Then the pixel (x_p, y_p) having the maximum correlation function value among the neighbouring pixels of (x_c, y_c) is chosen to be the correlation peak. Sub-pixel estimation is then applied.

To test the effectiveness of the proposed "sharp peak search" procedure, the laminar flow test data from an extreme test point is used here. The in-focus image pairs have a laser pulse delay time $\mathrm{d}t = 2.71$ ms, corresponding to a particle displacement of $\sim$8 pixels. The out-of-focus image pairs have $\mathrm{d}t = 0.19$ ms, corresponding to a particle displacement of $\sim$0 pixel. Due to the existence of certain bright out-of-focus particles, a PIV algorithm based on the conventional high peak search routine could output 0 pixel instead of 8 pixels as the measurement results, leading to outliers. Fig. 3.28 presents the percentages of outliers out of 250 image pairs, to compare the effect of the proposed sharp peak search routine with the conventional high peak search routine. Here, the conventional high peak search routine is also applied to image pairs pre-processed with a high-pass filter, which is a typical image filter for removing noise with low spatial frequency. The high-pass filter used in this test is that implemented in the PIVlab package and it works based on subtracting the images' low-frequency content generated from a 2D Gaussian smoothing kernel (15×15 pixels in this test). Fig. 3.28 shows that the high-pass filter is able to help with reducing the outlier occurrence, but that the proposed sharp peak search routine can even more effectively prevent outliers. In this case, it can be noticed that the outlier occurrence is actually not frequent even when the proposed sharp peak search routine or high-pass filtering is not applied. It is

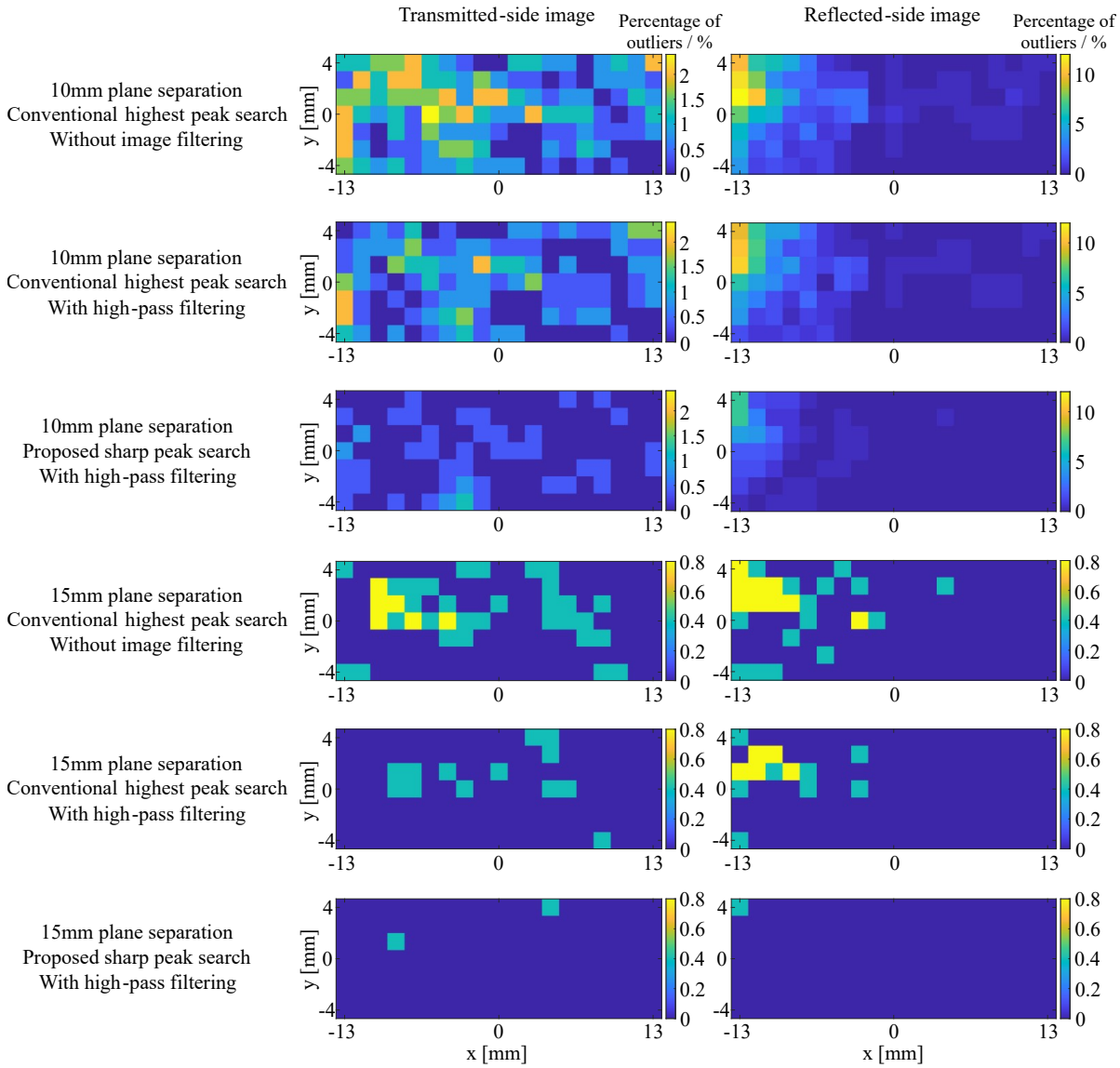

Figure 3.28: Percentages of measurement outliers: comparison between the conventional high peak search routine and the proposed sharp peak search routine. (Test condition: in-focus image pairs have a particle displacement of ∼8 pixels, out-of-focus image pairs have a particle displacement of ∼0 pixel. Due to the Case 2 error, the conventional high peak search routine is prone to generate 0-pixel as the measurement results.) The effect of high-pass filtering is also compared. Note the different colourbar scales used for different plane separations and the different sides of image.

expected that in experiments where solid PIV particles are used and particle clumps exist, the proposed sharp peak search routine would play a more significant role.

Throughout this thesis (except in Appendix A), the PIV vector calculations of all two-plane image pairs, including the numerically added ones and the simultaneous ones, were performed based on the proposed sharp peak search routine.

3.6.3 Correlation Peak Shape Change (Case 3)

In the presence of the defocused particles, the shape of the "correct" correlation peak of the in-focus particles would inevitably change, resulting in uncertainty in terms of sub-pixel displacement estimation. The influence of the peak shape change would largely depend on the slope of the "wrong" correlation peak at the location where the "correct" peak is. The absolute correlation function values of the two peaks would also make a difference. For a real PIV setup, it is not easy to accurately model the measurement uncertainty caused by peak shape change, due to camera noise, the non-uniform distribution of PIV particles within the flow, and the brightness difference of the particles. However, it is expected that the influence of the peak shape change would reach the maximum when the "correct" peak is located at the steepest part of the "wrong" peak, and then reduce as the "correct" peak approaches the margins of the "wrong" peak. This is because the overall cross-correlation consists of three components [33], the first is correlation due to particle displacements, the second is correlation due to noise (from background, camera, etc.), the third is correlation produced by particles but not due to displacement. As in Section 3.6.1, the correlation component caused by particle displacements can be modelled as the summation of the displacement correlation at each depth.

In this test, in-focus image pairs having the same $dt = 2.71$ ms ($\sim$ 8-pixel displacement) were numerically added with different out-of-focus image pairs having different dts, to generate "two-plane" image pairs with different combinations of "correct" and "wrong" peak locations. For each combination, 250 image pairs are analysed. Considering the characteristic arc shape of the defocused particle images, the measurement

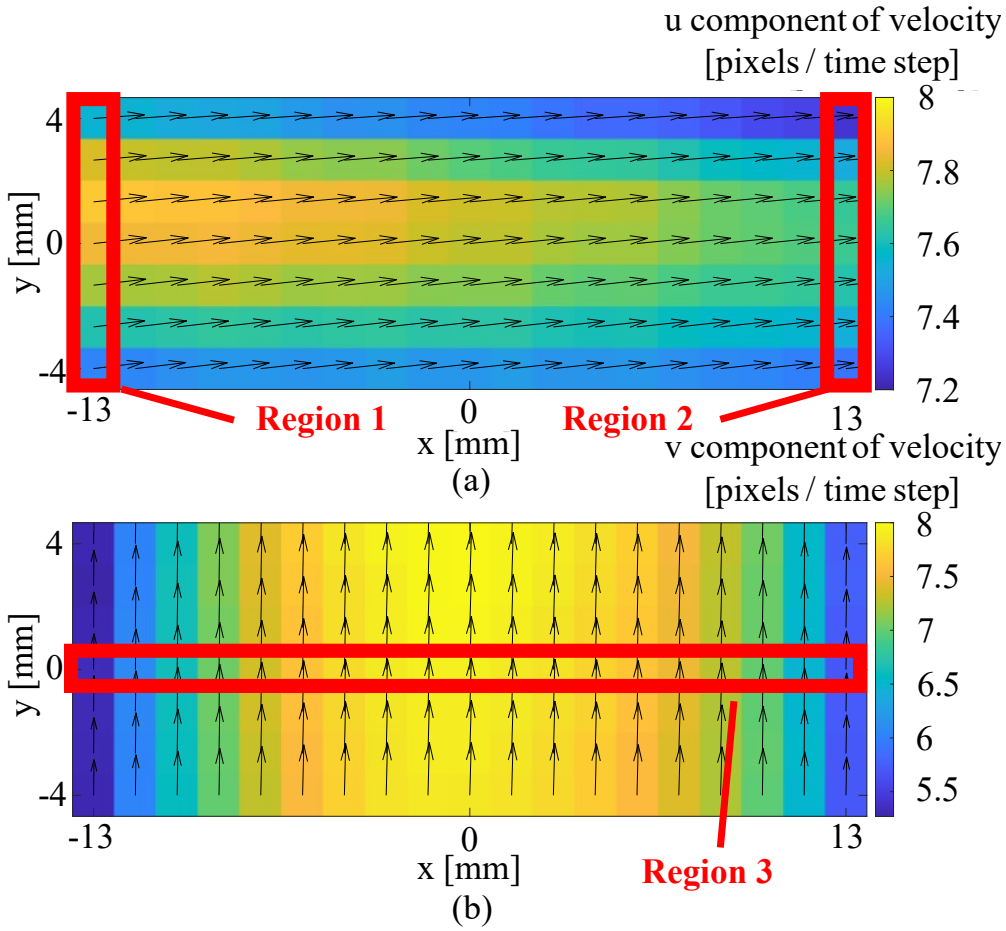

Figure 3.29: The average velocity fields of 250 in-focus image pairs of: (a) the horizontal flow, (b) the vertical flow.

uncertainty is evaluated separately on the horizontal and vertical component of velocity, by switching the orientation of the flow rig. It is noted that **throughout this chapter**, no vector post-processing/corrections were applied to the measured velocity fields.

Fig. 3.29 shows the average velocity fields of the in-focus image pairs. To examine the measurement uncertainty, the flow profiles of the three marked regions in Fig. 3.29 are analysed. Two regions are investigated for the horizontal flow, in order to look into the difference caused by the change of the defocused particle image shape at different horizontal locations (first shown in Fig. 3.21). As an example, Fig. 3.30 shows the average flow profiles of the in-focus image pairs, the defocused image pairs and the

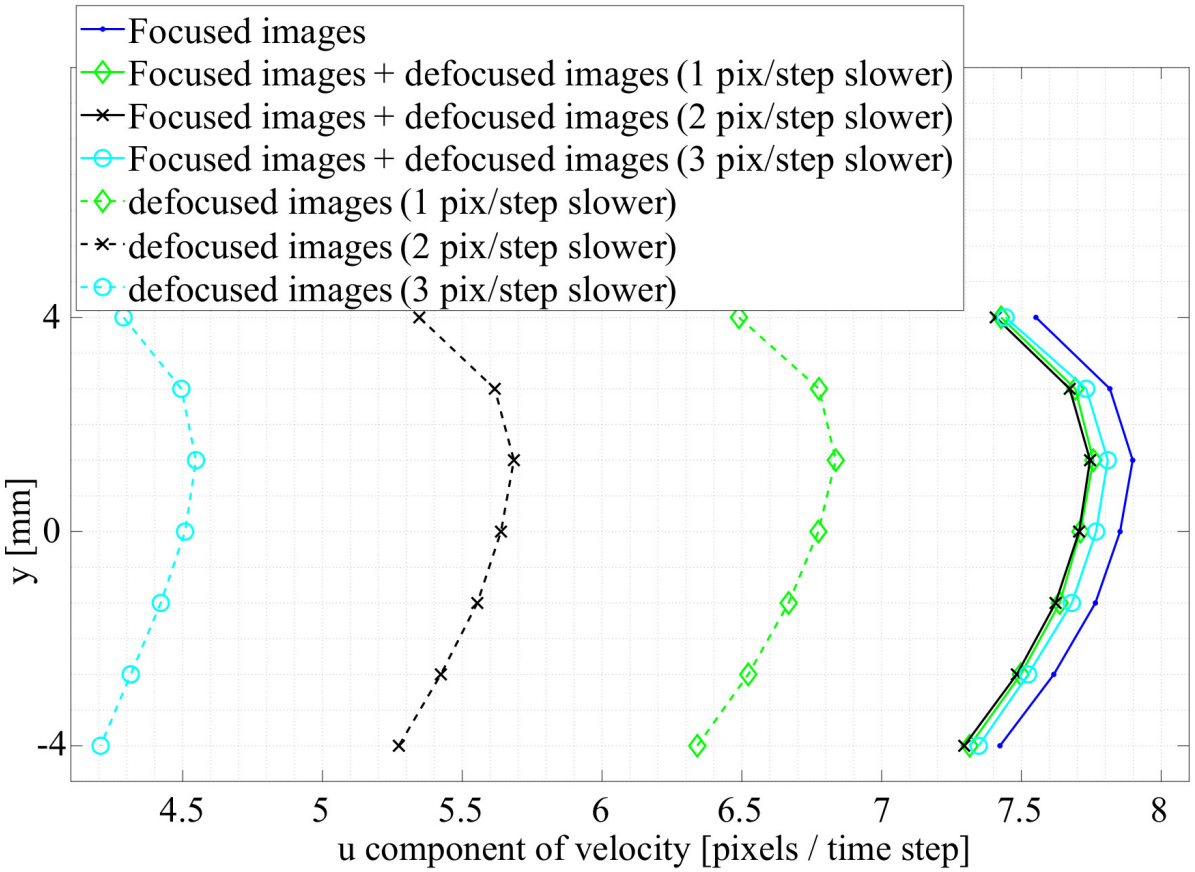

Figure 3.30: The average flow profiles of Region 1 of the reflected-side image. The defocused images were taken with a 15 mm plane separation. Note that the two-plane measurement error first increases and then reduces as the difference between the "correct" velocity and the "wrong" velocity increases.

numerically added two-plane image pairs in Region 1 of the reflected-side image at 15 mm plane separation. The different dts of the defocused image pairs were chosen so that the velocity difference between the "correct" velocity and the "wrong" velocity includes: ∼1 pixel per time step (green, diamond), ∼2 pixels per time step (black, cross), ∼3 pixels per time step (cyan, circle). As the difference between the "correct" velocity and the "wrong" velocity increases, the bias of the measurement result firstly increases, and then reduces. As discussed earlier, this could be explained if setting the distance between the peaks to ∼2 pixels causes the "correct" correlation peak to be located around the highest gradient part of the "wrong" correlation peak.

To closely inspect the measurement crosstalk, the absolute error of each component of each vector was calculated:

$$E_u = |U_n - U_s|\,, \tag{3.12}$$

$$E_v = |V_n - V_s|\,, \tag{3.13}$$

where U and V are the horizontal and vertical components respectively, and the subscript n and s are "numerical two-plane" and "single-plane". Fig. 3.31 and Fig. 3.32 plot the average absolute errors of the vectors in the three regions, at the 15 mm and the 20 mm plane separations. An obvious difference in the measurement error of Region 1 and 2 can be observed in the reflected-side image, but not in the transmitted-side image. This is related to the change of the defocused particle image shape across the sensor width. The difference between the reflected-side and the transmitted-side images is likely to be caused by the camera lens and the beamsplitter, and is worth further study by using different camera lenses and optics. In terms of magnitudes of the errors, at 15 mm plane separation, the average absolute error of either the horizontal or the vertical component is smaller than 0.2 pixels per time step; at 20 mm plane separation, the average absolute error of either the horizontal or the vertical component is smaller than 0.1 pixels per time step. For a specific experiment, the minimum plane separation can be determined based on the requirement of measurement accu-

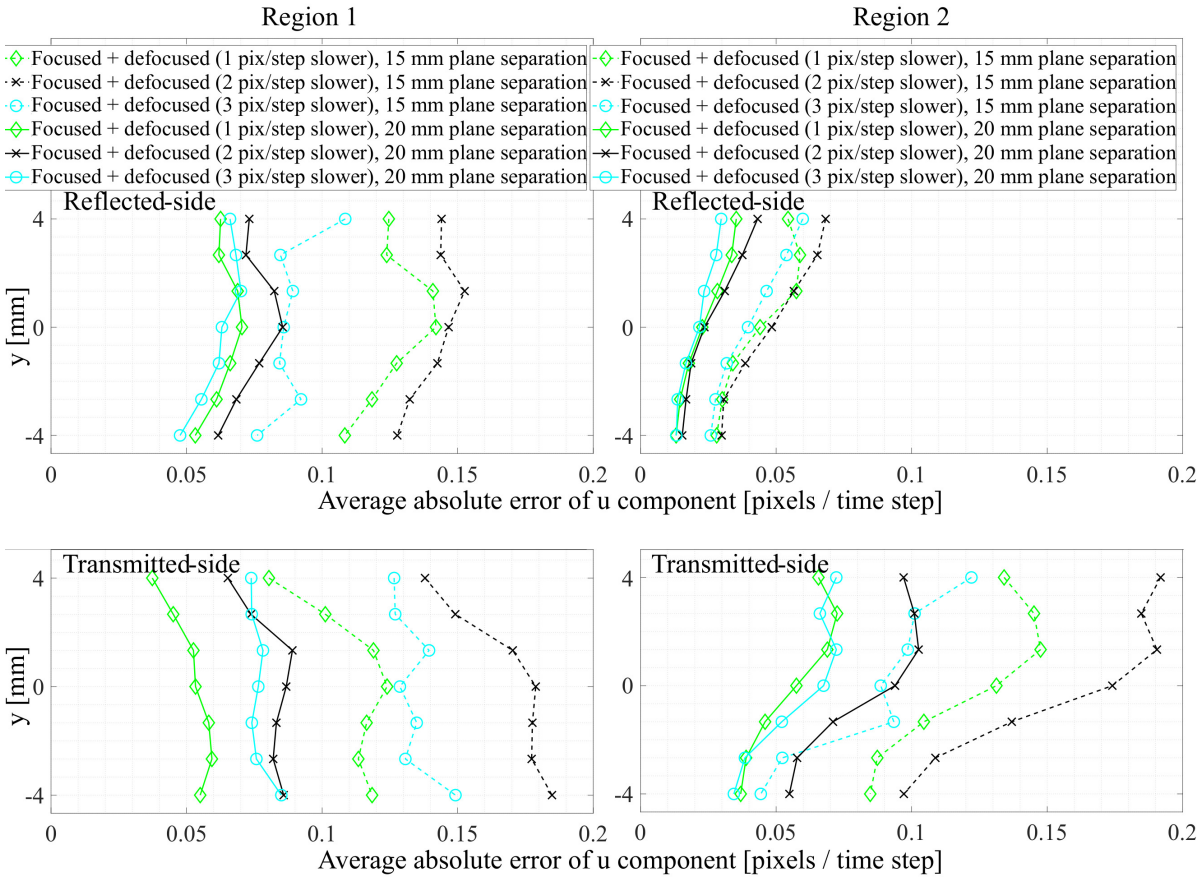

Figure 3.31: The average absolute errors of the horizontal velocity component in Region 1 and 2.

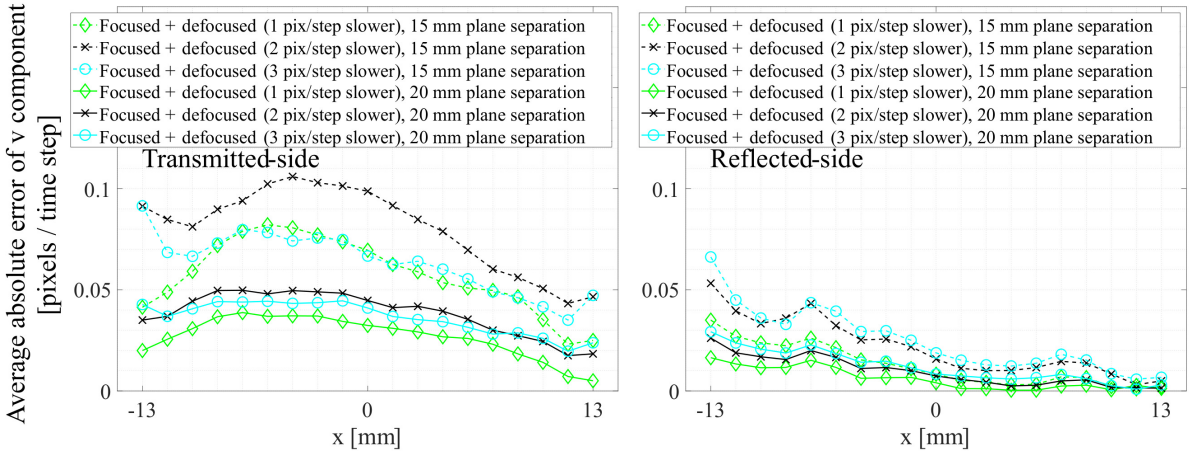

Figure 3.32: The average absolute errors of the vertical velocity component in Region 3.

racy. It is also noted that, if the flow field being measured is known *a-priori*, a smaller plane separation might be achievable, because the two-plane cross-talk is affected by the flow conditions on the two planes. For example, the measurement error of the vertical velocity component is smaller, which is beneficial for measuring a flow which is dominantly flowing vertically. (It is also worth noting that, if the measurement is performed with separate cameras instead of using a single camera with the image splitting device, the differences of the uncertainties for the two velocity components could be avoided.)

Now refer back to error Case 1 (Section 3.6.1). Consider a Case 1 cross-talk with a peak distance smaller than 1 pixel, the bias error caused by Case 1 can be estimated as smaller than '1 pixel multiplied by the weighting function'. Referring to Fig. 3.27, the largest local weighting function of the 15 mm plane separation is less than 0.2. Then, the maximum bias error caused by Case 1 for 15 mm plane separation can be estimated as $<$ (1 pixel multiplied by 0.2). This estimate lies within the bias error range indicated by Fig. 3.31 and Fig. 3.32, which are for the Case 3 cross-talk. The same method could also be applied to 20 mm plane separation, for an estimation of the bias error caused by Case 1 cross-talk, which is less than about 0.1 pixel per time step.

3.6.4 Uncertainty of Single-plane and Tomographic PIV

It would be useful to compare the measurement crosstalk caused by out-of-focus noise, to the measurement uncertainty in typical single-plane and tomographic PIV. Markus Raffel *et al.* stated that the precision in determining the location of the correlation peak maximum is typically larger than 0.05 pixel [11]. Andrea Sciacchitano showed that the evaluation of the actual uncertainty in a PIV experiment should also consider the effects of laser alignment, camera calibration, and so on, which could vary in different experiments [63]. In the 4th International PIV Challenge [64], a case study based on real experimental data was shown. A tomographic reconstruction of the three-component velocity field in a sheet slicing through a laminar vortex ring was performed

using five cameras. Different participant teams attempted stereoscopic PIV based on the particle images from two of the five cameras. The stereoscopic PIV results were compared to the tomographic PIV result, which was considered to be the "ground-truth" result based on the notion that a tomographic PIV system measures the three-dimensional velocity field within a laser sheet more accurately than traditional stereo PIV measurements. The comparisons showed that the average absolute errors of the in-plane components calculated by the different participant teams were between 0.03 to 0.05 pixel per time step, and the average absolute errors of the out-of-plane component were about 3 times the in-plane component errors. Ning Liu *et al.* performed a controlled tomographic PIV experiment by embedding tracer particles in solid samples, and showed that for a six-camera system with a particle seeding density between 0 and 0.2 ppp (particles per pixel), the reconstructed vector uncertainty is between 0.8 and 1.4 voxels, where the voxel:pixel resolution is 1:1 [65].

3.6.5 Effect of High-pass Filtering

Section 3.6.2 mentions that a high-pass filter is able to suppress the influence of bright out-of-focus particles, therefore reducing the outlier occurrence. Here the effect of high-pass filtering on the Case 3 error (i.e. sub-pixel displacement estimation) is presented. Details of the high-pass filter are given in Section 3.6.2. As an example, Fig. 3.33 shows the same test points as in Fig. 3.31, but now the average measurement errors of the horizontal velocity component are presented after high-pass filtering the particle images. It is noticed that at 15 mm plane separation, the average measurement error is now reduced to be smaller than 0.1 pixels per time step. Section 3.6.2 and this section show the capability of a high-pass filter reducing the Case 2 and Case 3 errors. The effect of high-pass filtering on Case 1 error, which was evaluated in Section 3.6.1 by calculating the self-correlation peak curvature, needs further assessment in future, because high-pass filtering defocused images would lead to artificially sharp self-correlation peaks. The optimal design and parameter of high-pass filter for defocusing PIV are also topics for future research.

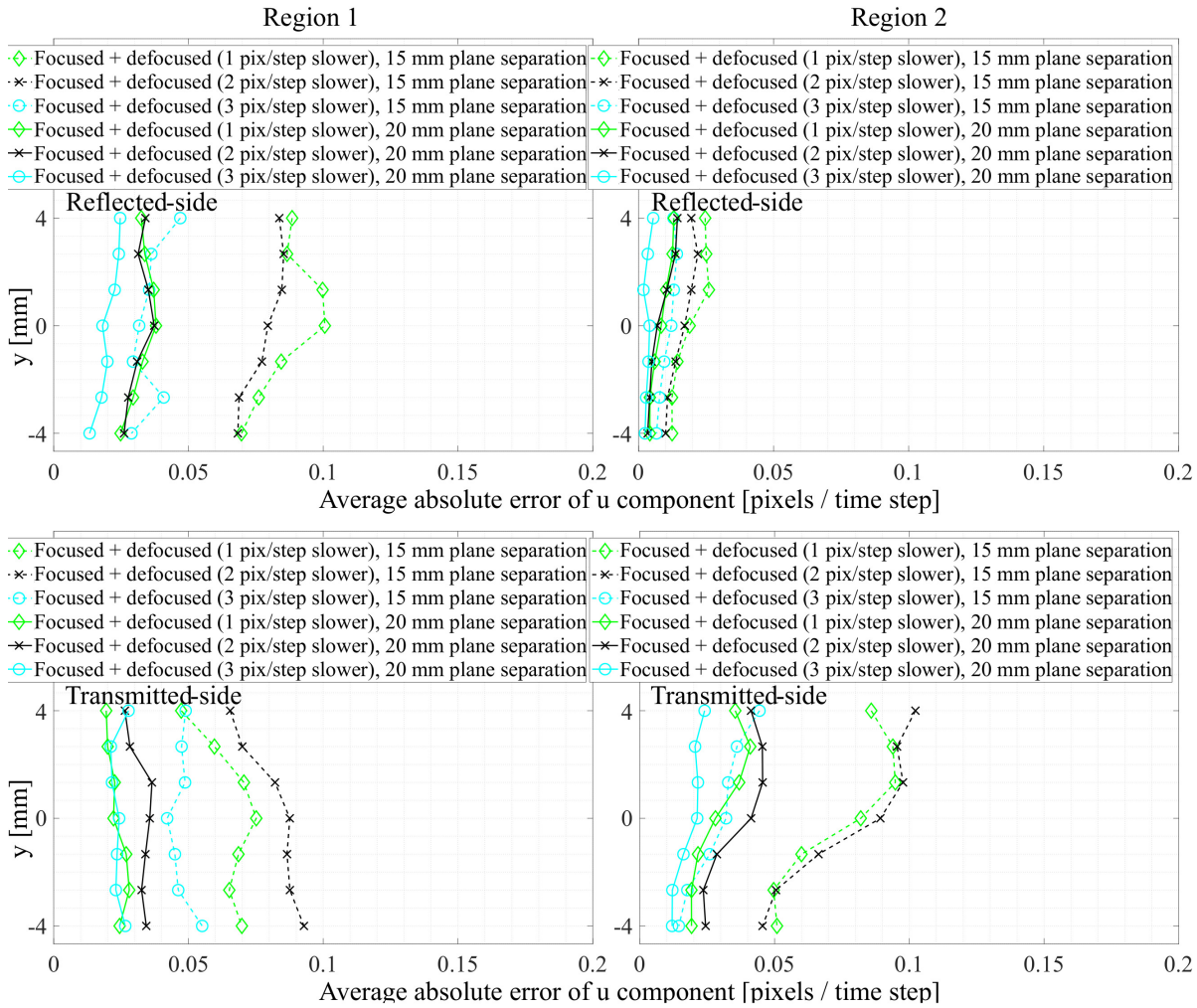

Figure 3.33: The average absolute errors of the horizontal velocity component in Region 1 and 2, high-pass filtered images.

3.7 Summary

This chapter introduces the design of the image splitting device, and illustrates that it is compatible with the Scheimpflug condition and could in principle be used for two-plane stereoscopic PIV. The device hardware and alignment are introduced. A laminar flow test was set up for analysing crosstalk caused by defocused particles. The three types of measurement crosstalk observed are: Case 1: when the "correct" correlation peak and the "wrong" correlation peak are close to each other, they merge into a combined peak. In this case, the relative contribution of the defocused particles on the measured velocity can be estimated by the curvature of the correlation peak they produce. Case 2: when bright out-of-focus particles exist due to reasons such as non-uniform particle sizes, the "wrong" correlation peak can be higher than the "correct" one, resulting in the conventional "highest peak" search routine picking up the "wrong" peak. A "sharp peak search" routine is proposed here to effectively prevent such outliers. Case 3: due to the existence of the "wrong" correlation signal, the shape of the "correct" peak is inevitably changed, leading to uncertainty in terms of sub-pixel displacement estimation.

The three types of cross-talk indicate that the measurement uncertainty depends not only on the extent of defocusing of the particles, but also on the flow fields. In the laminar flow test, in-focus image pairs having the same dt were numerically added with out-of-focus image pairs having different dts, to simulate "correct" and "wrong" peaks with different distances. With the current imaging setup, at 20 mm plane separation, the average measurement error of each velocity component is lower than 0.1 pixels per time step. It is expected that with a smaller field of view (i.e. a smaller working distance), the depth of field of the imaging system will become even more shallow, so that crosstalk can be further reduced, and a smaller plane separation could be achieved. The effect of image pre-processing on suppressing the influence of the defocused particles has been preliminarily tested using a high-pass filter. It effectively lowers the measurement uncertainty in terms of sub-pixel estimation. The optimal pre-processing filters and settings will be further investigated in future. The optical

distortions reported in Section 3.5 also worth more study, by using different camera lenses and optics.

The work in this chapter is the first systematic evaluation of macroscopic defocusing PIV, and established the foundation for the two-plane flow velocimetry work in the next chapter.

Chapter 4

Two-plane Flow Velocimetry

The defocusing based PIV technique was applied for simultaneous PIV measurements on two swirl planes of an optically accessible internal combustion engine (or "optical engine" for short). The technique was able to simultaneously reveal the instantaneous tumble and swirl vortex structures in individual cycles, which was not achievable by typical single-plane PIV due to cycle-to-cycle variation (CCV).

This chapter begins with a brief introduction to the working principle and terminology of internal combustion engine, tumble and swirl flow study in engine cylinder, the history of optical engine, and the optical engine used in this thesis. The experimental setup and test condition for the two-plane flow velocimetry are then introduced, followed by a description of image processing and PIV calculation routines. The two-plane crosstalk is then evaluated, by numerically adding single-plane illuminated images. The instantaneous swirl flow and tumble vortex structures are then measured and presented.

The work in this chapter is published in [58].

4.1 Internal Combustion Engines

The working principle of Internal Combution Engine (ICE) is based on combustion of an air-fuel mixture to raise the temperature and pressure within a sealed chamber (the cylinder). The high pressure gases do work as they expand and displace a piston, which constitutes a moving wall of the cylinder. The linear motion of the piston is transformed to rotational motion of a crank shaft, via a connecting rod. The rotational motion can then be used to drive machinery or generate electricity.

"Gasoline/petrol" and "diesel" are the two typical designs of ICEs. Gasoline engines typically mix fuel and air into a homogeneous mixture before compression. The compressed mixture is then ignited by a spark. Therefore gasoline engines are more generally called Spark Ignition (SI) engines. In contrast, diesel engines use Compression Ignition (CI), where fuel is injected as the air is compressed. The injected fuel is ignited by the hot compressed air without needing a spark.

In this thesis, the optical diagnostics were performed on a SI Direct-injection (DI) 4-stroke engine. A four-stroke engine reciprocates with a period defined by two full rotations of the crankshaft. The progression of an engine cycle is measured using 720 Crank Angle Degrees (CAD), which are divided into four strokes. The cycle begins with the intake stroke, in which the piston travels downwards to draw a fresh air-fuel mixture into the cylinder. In contrast to Port Fuel Injection (PFI) which injects fuel upstream of the intake valves, a DI engine injects fuel directly to the cylinder at some point during the intake stroke. At the end of the intake stroke, the piston reaches the bottom of its stroke, the so-called Bottom Dead Centre (BDC). The second stroke is the compression stroke. The piston travels back up towards the cylinder head with the intake valves closed. The quasi-adiabatic compression process causes the mixture pressure and temperature to rise. The spark plug at the roof of the cylinder will typically produce a discharge arc some CAD before the piston arrives at the top of the stroke, Top Dead Centre (TDC). The spark ignites the mixture, producing rapidly-expanding hot gases which press the piston back down and turn the crankshaft. This is the expansion stroke in which the cylinder does work. The fourth stroke is the exhaust

stroke, which happens following the BDC event of the expansion stroke. The piston travels upwards again with the exhaust valves open, expelling exhaust gases from the cylinder.

Typically, ICEs in laboratories have the crankshaft connected to a dynamometer, which is a device for dissipating the work produced by the engine driving it. Normally, a dynamometer can measure engine speed and torque, and can also drive the crankshaft without combustion, by employing electric motors. This is the so-called "motored" condition and can be useful when researchers would like to isolate effects of combustion event (e.g. to study turbulent flow motion in the cylinder). In contrast, when combustion occurs in the cylinder, the engine is said to be running under "fired" condition. In this chapter, the optical engine ran under a motored condition, while it operated at fired condition in the next chapter.

4.2 In-cylinder Charge Motion

In-cylinder charge motion is an essential consideration in the design of engine induction and combustion systems. In an ICE, the interaction between in-cylinder air and injected fuel determines the homogeneity of the air-fuel mixture when ignited. The in-cylinder charge motion also has a significant influence on early flame structure and flame propagation speed. Due to the high-speed motion of the piston, the in-cylinder flow field is highly three-dimensional and turbulent. It consists of both small-scale turbulence and large-scale flow structures determined by the cylinder geometry. The large-scale flow structures are typically separated into swirl and tumble, according to their rotation axis (see Fig. 4.1): swirl refers to motion around the axis of the cylinder and tumble is motion around an axis perpendicular to the cylinder driven by titled intake valves' orientation. In the compression stroke, the bulk flow is compressed by the piston going upwards with a high speed. The large-scale swirl and tumble become unstable and break down into smaller turbulent structures. When the air-fuel mixture is ignited, some residual bulk flow motion could still persist and interact with the early

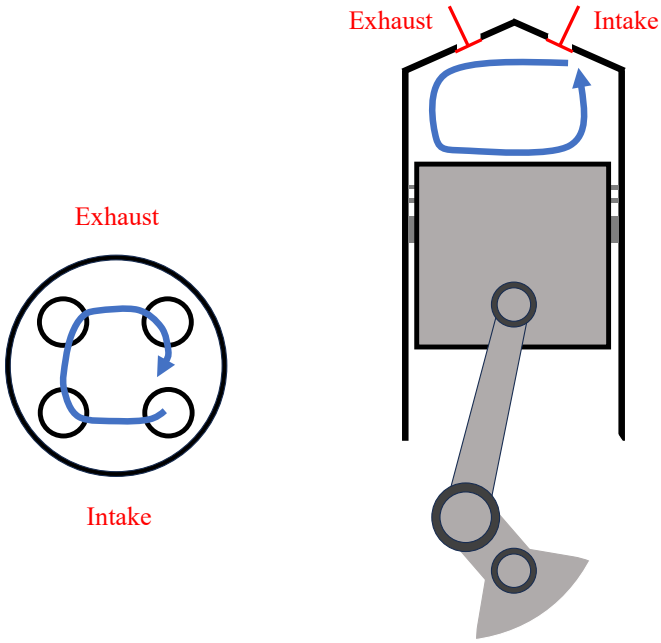

Figure 4.1: The two large-scale in-cylinder flow structures: (a) swirl; (b) tumble.

flame kernel.

In SI engines, the variations of the large-scale flow structures from cycle to cycle are believed to be one of the major sources of the cycle-to-cycle variation (CCV) [66], which indicates that consecutive cycles are not exactly the same even under a constant condition. The combustion process in every individual cycle does not proceed in the same way, leading to a varying in-cylinder pressure curve in different cycles. CCV is directly responsible for variations in output torque. A literature survey [67] by Nir Ozdor *et al.* pointed out that if CCV were eliminated, engine brake power could improve by ∼10% for the same fuel consumption.

In order to reduce CCV and achieve fast/complete combustion, modern DISI engines typically use an induction system which can produce strong and repeatable tumble flow [68], which is achieved by careful design of the intake valves, tumble flaps [69, 70], and Variable Valve Actuation (VVA) systems [71, 72]. The interaction/overlay of tumble and swirl is also found to be relevant for mixture preparation, burn dura-

tion and thereby CCV [73]. For characterising the in-cylinder large-scale tumble and swirl flows, PIV on swirl planes (Fig. 4.1 (a)) and tumble planes (Fig. 4.1 (b)) in optically-accessible engines (which will be reviewed and discussed in the next section) is a typical and effective method [74, 75, 76]. However, a typical single-plane PIV setup could only measure one plane at a time. Study on tumble or swirl typically needs independent setups. Non-simultaneous 3D reconstruction could be achieved by scanning or rotating the measurement plane and averaging the PIV results on each plane location independently [77]. Instantaneous 3D PIV could be used for full 3D flow structure investigation, but the particle seeding number is the primary limiting factor, especially in the pent-roof region close to the valves where optical access is very limited. In this chapter, the defocusing based PIV technique is applied for a two-plane PIV measurement on two swirl planes. In addition to the swirl flow structure which could be typically measured on a swirl plane, simultaneously imaging an additional swirl plane provides extra information on the tumble vortex structure. This measurement is based on a typical single-plane PIV system with the image splitting optics, and with a particle seeding density typical of a single-plane PIV measurement.

4.3 Optical Engine History

From the very early stages of ICE development, visualisation of the in-cylinder mixing process and the combustion process has been essential. It is said that the earliest trial of using an optical engine to better understand the flow and mixing phenomena was by Nicolaus Otto himself [78], the father of practical SI engines. He built a hand-cranked model engine employing a glass cylinder, using hand-rolled cigarettes to provide smoke for visualisation studies. In the 1920s, Harry Ricardo reported an optically accessible side-valve engine to measure flame travel speed, in which a removable engine head was fitted with a row of 6 windows placed at equal intervals from the spark plug [79]. Later, researchers at General Motors Research Laboratories employed an engine with a rectangular quartz window (127 mm long and ∼10 mm wide) that traversed the

length of the combustion chamber [80]. The window was mounted in a special retainer to minimise stresses.

A milestone of optical engine measurement was established in 1936, the optical access of the General Motors Research Laboratories engine was significantly improved by Gerald M RassWeiler and Lloyd Withrow, by cementing a quartz plate on the top of the cylinder allowing an unobstructed view of the entire combustion chamber [81]. They also developed a drum camera with an imaging rate of 5000 frames per second, corresponding to every 2.4 CAD at an engine speed of 2000 rpm. By correlating cylinder pressure and volume with the flame images, they pointed out that the mass of the burned charge could be deduced from cylinder pressure and volume [82], which was the origin of quantitative analysis of the combustion process from cylinder pressure trace. This work again demonstrated the significant power of optical diagnostics in engine research.

To further extend the available optical access, a motored engine equipped with a 12.7 mm thick glass liner, supported by a steel casting, was reported in 1939 by researchers of the National Advisory Committee for Aeronautics (NACA, which transformed into NASA later) [83]. In 1958, Frederick W Bowditch applied for a patent on the revolutionary, optically accessible piston [84], which is called the Bowditch piston in the optical engine research community. The Bowditch piston is a hollow extended piston with a quartz window on the top, allowing the cylinder to be viewed from beneath using a 45-degree mirror in the piston void. Since optical access from above is typically not achievable in modern overhead-valve engines, the optical liner plus Bowditch piston became the mainstream of optical engine design, providing the largest possible degree of optical access without significantly modifying the cylinder geometry.

4.4 Optical Engine Used in This Thesis

The optical engine used in this work is a single-cylinder engine based on a Jaguar Land Rover petrol engine of the Ingenium family. Fig. 4.2 shows a diagram of the

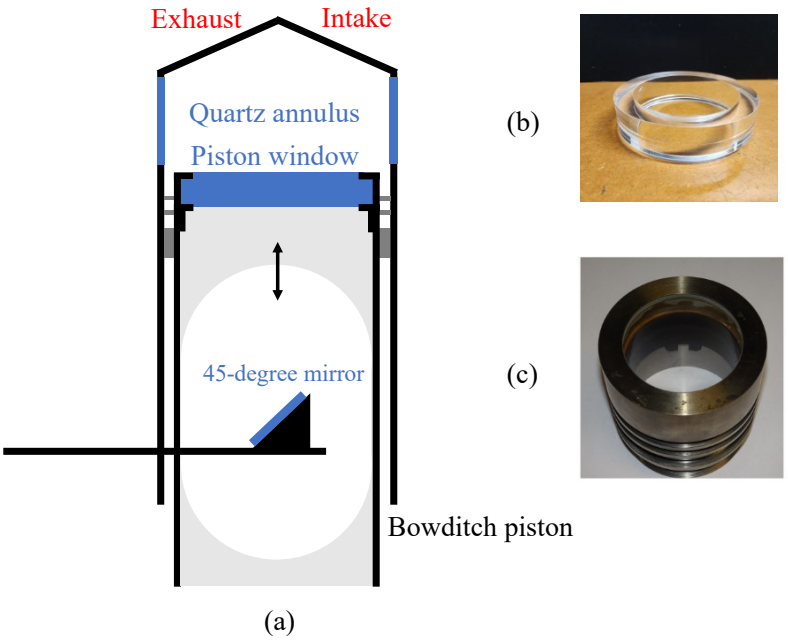

Figure 4.2: (a) A diagram of the optical engine cross section; (b) The fused silica annulus; (c) The optical access piston with window (this photo is kindly provided by Dr. Christopher Willman).

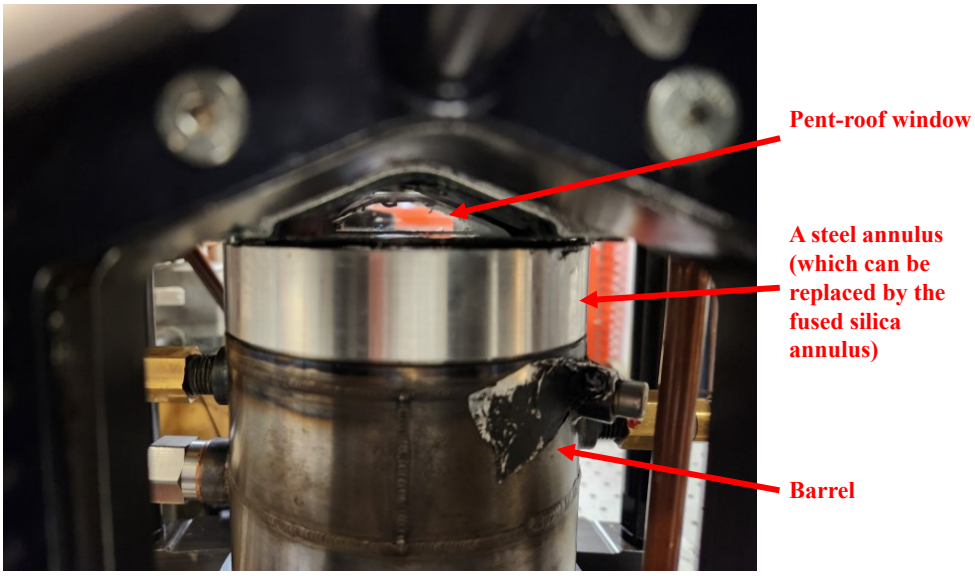

Figure 4.3: A closer look at the optical engine cylinder.

engine geometry. The optical engine uses a Bowditch piston design, enabling optical access through a piston crown window (60mm diameter) via a stationary 45-degree mirror within the void of the piston. Optical access from the sides is provided by a quartz annulus (24 mm high) at the top of the barrel, which is a metal section through which coolant water flows for temperature control. This engine also has a couple of triangular-shape windows on the sides of the "pent-roof", providing optical access to the small volume of the cylinder remaining at TDC, which accommodates the fuel injector, spark plug, intake valves and exhaust valves (Fig. 4.3). The "pent-roof" windows were used in this chapter.

The crankshaft of the engine is connected to a direct-current dynamometer with a Control Techniques controller. A shaft encoder mounted on the crankshaft measures the engine position in CAD. The encoder signals are sent to the Engine Timing Control System (ETCS) and Data Acquisition (DAQ) system. ETCS is an in-house LabView program (developed by [85]) and is responsible for controlling the engine operation (e.g. controlling the injection and ignition timings). A LaVision Programmable Timing

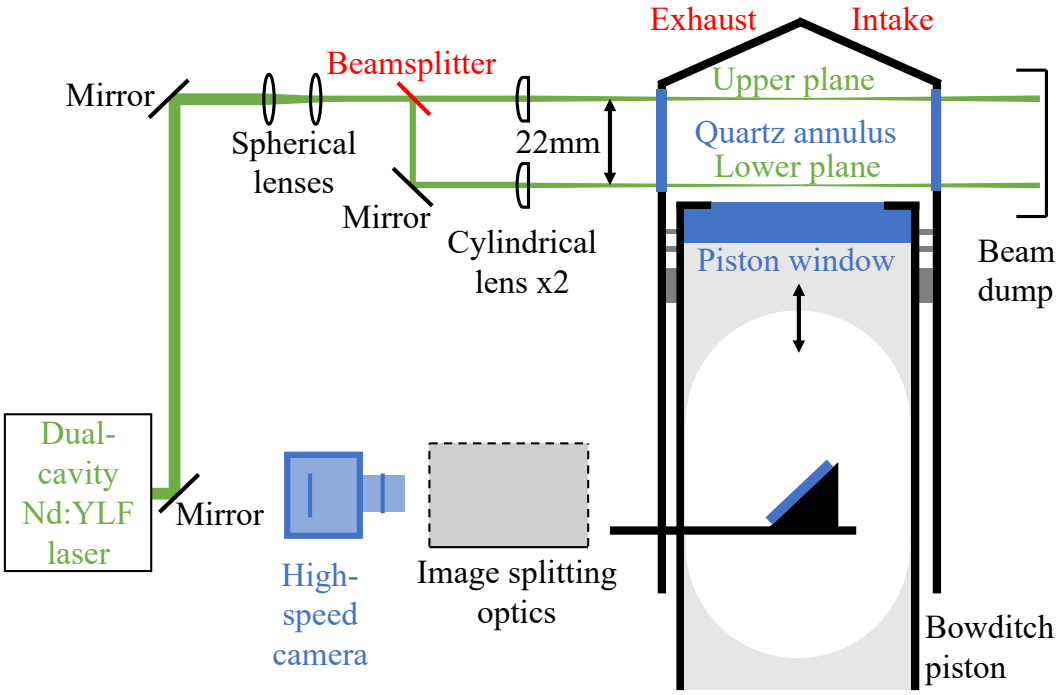

Figure 4.4: Schematic of the in-cylinder two-plane velocimetry setup.

Unit (PTU), X v10, receives pulses from ETCS and triggers the high-speed laser and camera for optical diagnostics. Two National Instruments (NI) DAQ cards were used for monitoring the engine performance. The high-speed DAQ card (NI 6070E) acquires parameters such as cylinder pressure and intake valve lift with a temporal resolution of every CAD. The low-speed DAQ card (NI PCI-6024E) records data such as engine torque and coolant temperature once every engine cycle. More details of the engine can be found in [86].

4.5 Experimental Setup

4.5.1 Hardware

The two-plane PIV setup is shown in Fig. 4.4 and Fig. 4.5. A dual-cavity Nd:YLF laser (Photonics Industries DM20–527-DH, see Table 4.1 for the specification) was used to generate the pair of PIV laser beams. Right in front of the exit aperture of the laser,

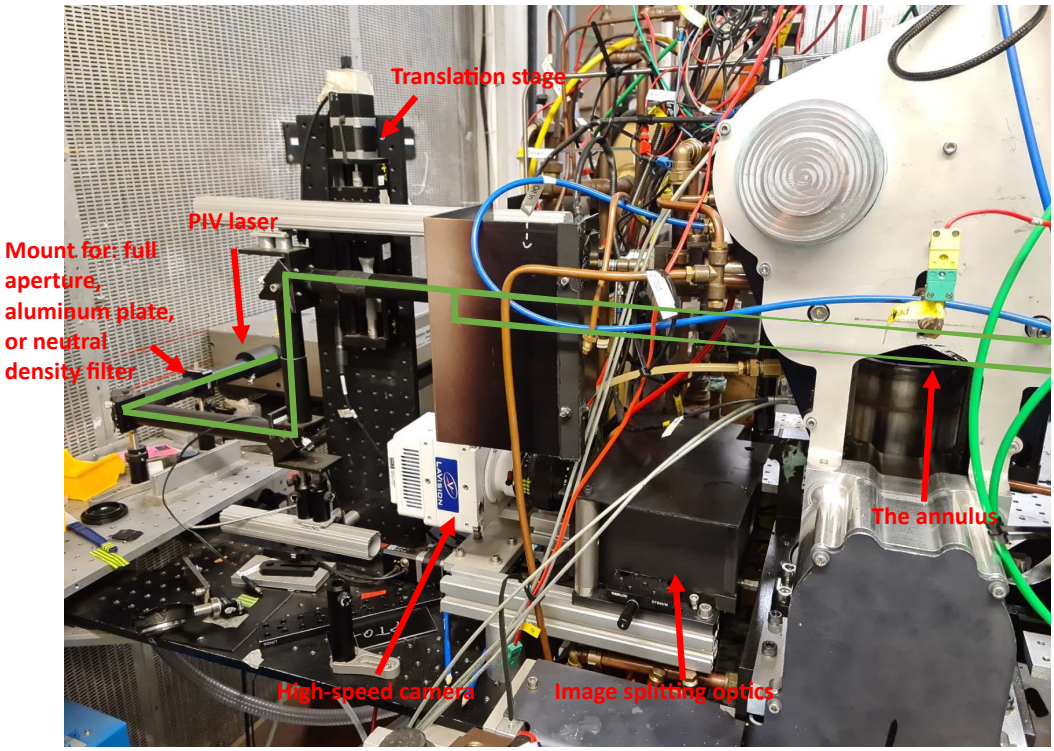

Figure 4.5: Experimental setup of the in-cylinder two-plane velocimetry.

Table 4.1: Nd:YLF laser specification.

Wavelength	527 nm
Maximum output power at 1 kHz	23.8 mJ pulse energy (per cavity)
Maximum output power at 8 kHz	4.3 mJ pulse energy (per cavity)
Repetition rate	up to 8 kHz (each cavity)
Beam diameter	6 mm
Pulse width (Full width half maximum)	403-422 ns
Divergence (Full angle for 86% of the energy)	< 9.2 mrad

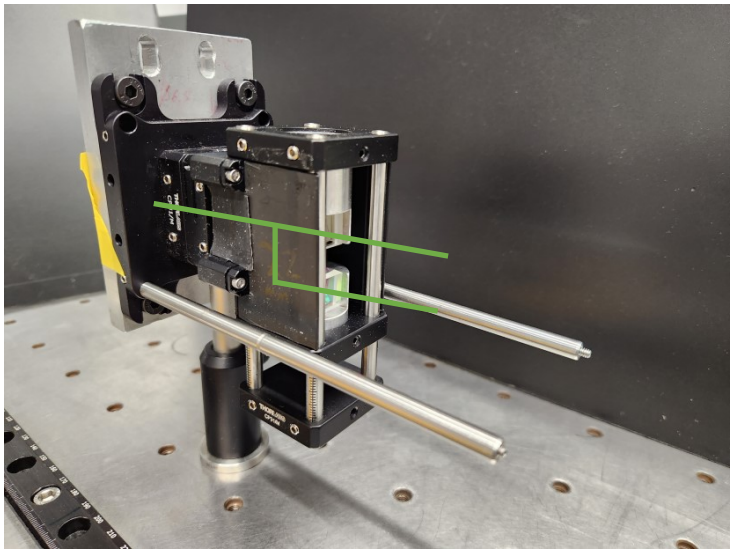

Figure 4.6: The two-plane laser splitting and sheet-forming optics, mounted on a Thorlabs 30 mm cage system. To be specific, the optics were mounted in the cut recesses of home-made one-inch aluminum posts. The posts were mounted in the 30 mm cage plates.

there was a mount (Thorlabs CFH2/M) which can accommodate an aluminum plate, a neutral density filter (OD 3.0), or an one-inch full aperture. The aluminum plate was inserted to the mount to act as a fail-safe shutter for when no laser beams were desired. The neutral density filter was used for laser beams/sheets alignment. The one-inch full aperture was for actual PIV tests. The laser beams were lifted using 45-degree mirrors to the height of the optical liner. A LaVision telescope was used to adjust the sizes of the beams. Right next to the telescope was the laser splitting and sheet-forming optics, consisting of a 50/50 non-polarising beamsplitter (Edmund Optics 35959), a dielectric prism mirror (Edmund Optics 37654) and a pair of anti-reflection coated cylindrical lenses (f = – 50 mm, Edmund Optics 37599), mounted using a Thorlabs 30 mm cage system (Fig. 4.6). Prior to the engine tests, the laser splitting and sheet-forming optics assembly was aligned on an optical table in another lab, to successfully generate two laser sheets with a 22 mm displacement, using the same principle for aligning the image splitting optics. Then the laser splitting and sheet-forming optics assembly was moved to the engine setup as a whole. The telescope and the 30 mm cage system were

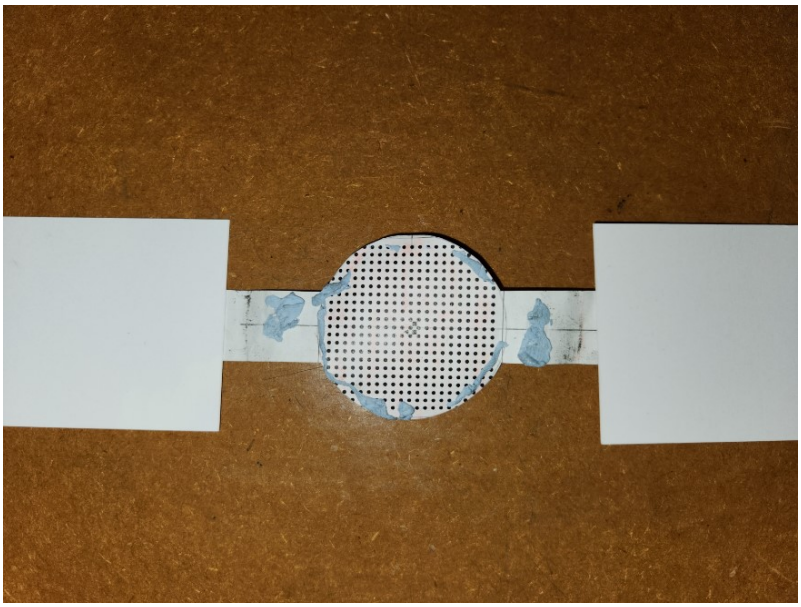

Figure 4.7: The calibration grid on a transparent acrylic disc.

connected using one-inch lens tubes, and were mounted on a vertical translation stage, for fine tuning the heights of the two laser sheets. The two laser sheets illuminated two swirl planes in the cylinder. The upper plane was 2.5 mm below the engine firing deck (i.e. the top of the annulus where the gasket and engine head sit), and the lower plane was 22 mm below the upper plane. The widths of the sheets were about 30 mm in the centre of the image field of view. A high-speed CMOS camera (Phantom VEO 710L, 1024 $\times$ 1024 pixels) and the image splitting optics looked at the two swirl planes from beneath, through the 45-degree mirror (mounted in the void of the Bowditch piston) and the piston window. A LaVision aerosol generator (the same type as used for the laminar flow test in Chapter 3) was used to seed olive oil droplets into the intake plenum.

The camera calibration was performed by imaging a printed dot grid positioned on the two measurement planes. The grid was stick to a transparent acrylic disc (Fig. 4.7) with the same diameter (84 mm) as the piston. The acrylic disc was placed on top of the piston window. By turning the crank shaft by hand using the keyed handle on the dynamometer, the acrylic disk with the calibration grid could be positioned at an

Table 4.2: Engine specification (motored).

Bore	85 mm
Stroke	90 mm
Valves per cylinder	2 intake, 2 exhaust
Engine speed	1000 revolutions per minute (rpm)
Intake pressure	70 kPa
Intake air temperature	316 K
Coolant temperature	296 K
Intake air volume flow rate	1.65 L / s

Table 4.3: Laser pulse delay time (dt) within an image pair at different CAD (bTDC).

120-105 CAD	100-85 CAD	80-55 CAD
60 μs	50 μs	40 μs

appropriate height as needed.

4.5.2 Test Condition

The measurement was performed every 5 Crank Angle Degrees (CAD) during the compression stroke from 120 to 55 CAD before top dead center (bTDC). The engine was operated under motored conditions (see Table 4.2). The temporal resolution was restricted to 5 CAD (i.e. 1200 Hz) due to the laser pulse energy, which reduced with higher repetition rate.

As in single-plane PIV, the laser pulse delay time dt within an image pair needs to be optimised for each crank angle, to minimise loss-of-correlation due to the out-of-plane motion of seeding particles, while retaining as high dynamic range of the velocity measurement as possible. Table 4.3 summarises the dt settings for this experiment. The particle displacements in this test are from $\sim$0 to $\sim$4 pixels.

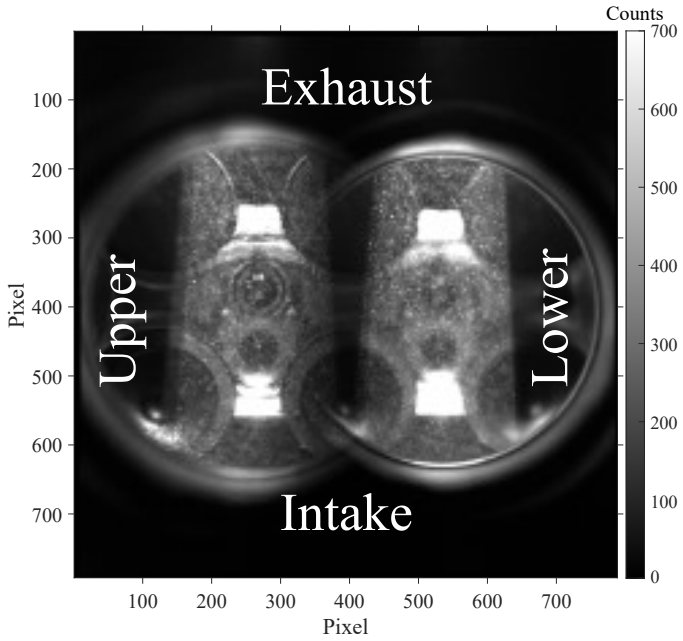

Figure 4.8: A raw image of the two-plane PIV test. The bright background scatter needed to be removed.

4.5.3 Image Processing and PIV Settings

Fig. 4.8 shows a raw image of the two-plane PIV test. In order to remove the bright scatter from the valves, spark plug, fuel injector, and the reflective surface of the cylinder head, a dynamic background subtraction filter was applied: each raw image was subtracted by the average of a summation of images, which are at the same crank angle, but from 11 consecutive cycles, including itself (see Fig. 4.9 for a demonstration). The background subtraction was performed across cycles for each crank angle, because the background scatter changed slightly at different crank angles, as the piston travelled. Fig. 4.10 shows the background subtracted image of Fig. 4.8.

PIV vector calculation was performed with the Matlab toolbox PIVlab (v2.56). The same window deformation based multi-pass algorithm with the proposed "sharp peak" search routine was used, as in Chapter 3. The interrogation windows decreased from 64 $\times$ 64 pixels to 32 $\times$ 32 pixels with a 50% overlap, leading to a vector spacing of about 2.2 mm. The particle seeding density is about 25 particles per final interrogation window, which is about the typical seeding density used in a normal single-plane PIV

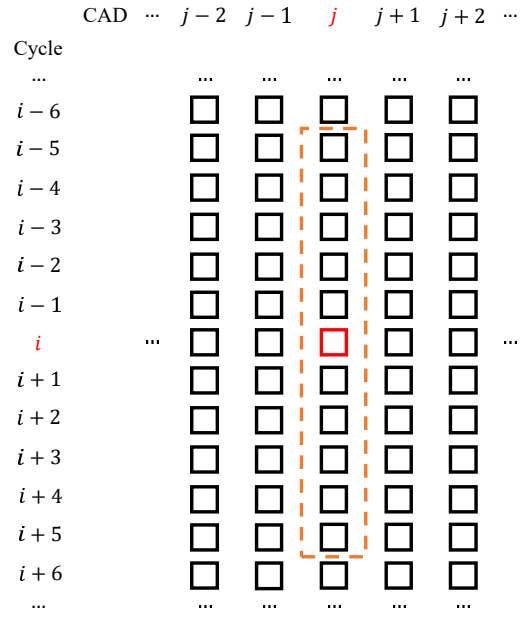

Figure 4.9: Demonstration of the dynamic background subtraction filter. The red rectangle in the centre indicates the raw image being processed. The rectangles enclosed in the orange dash box indicate the group of raw images used for background subtraction.

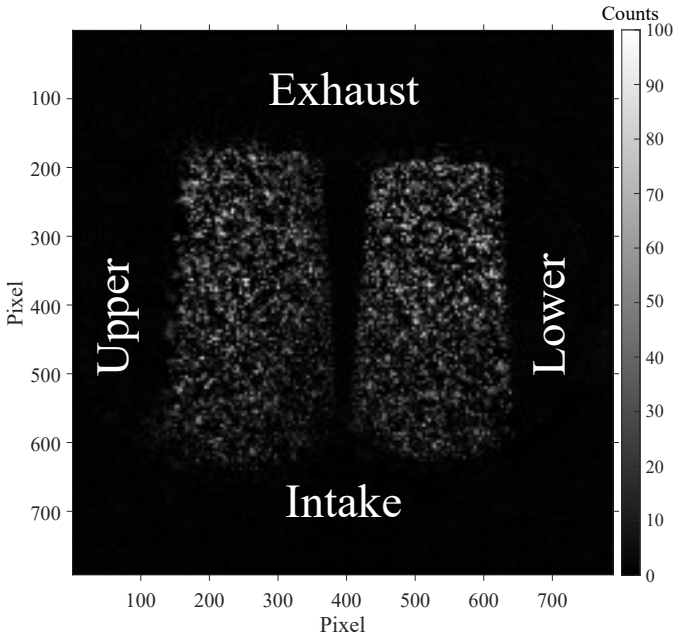

Figure 4.10: The background subtracted image of Fig. 4.8. The colorbar scale is changed.

measurement. In the past, the same seeding density was used in the single-plane PIV experiments on the same engine [87].

4.6 Two-plane Crosstalk Evaluation

In order to evaluate the error caused by the out-of-focus particles, additional single-plane PIV measurements at the same test condition were performed. For clarity, here the author uses "simultaneous two-plane test" to describe the test in which both the upper plane and the lower plane were simultaneously illuminated; "upper-plane test" for the test in which only the upper plane was illuminated; "lower-plane test" for the test in which only the lower plane was illuminated. The latter two are collectively called "single-plane tests". For each test, 450 cycles of data were analysed. By numerically adding images from the "upper-plane test" with the images from the "lower-plane test" (called "numerical two-plane" hereafter), the measurement crosstalk was quantified. As discussed in Chapter 3, the distance between the "correct" and the "wrong" correlation peaks has an influence on the exact measurement error and this is measured with the unit of pixels. Therefore, the velocity unit used in the crosstalk evaluation is "pixels / dt". Real velocity values in m/s will be used for the discussion of the flow velocity fields.

A vector validation process was applied to all PIV vector fields (including the simultaneous two-plane data, the single-plane data, and the numerical two-plane data). Each vector was compared to the median of its surrounding vectors. If the difference in any component of a vector was larger than 1 pixel / dt, that vector was considered spurious and replaced by the median of its surrounding vectors (see Fig. 4.11). In this chapter, a strict data quality requirement was imposed: image pairs in which adjacent spurious vectors exist were discarded, as this was considered to indicate strong out-of-plane motion (and thereby loss-of-correlation of PIV particles). Fig. 4.12 demonstrates the cases which were discarded. Fig. 4.13 shows the numbers of image pairs remained after discarding, for the "upper-plane data", "lower-plane data", and the "numeri-

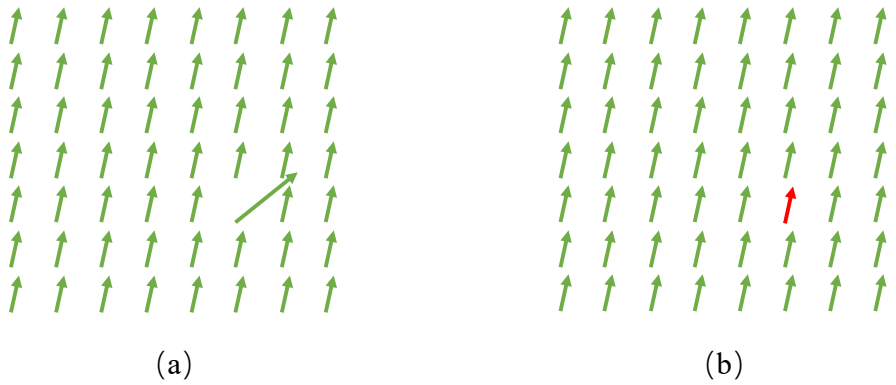

Figure 4.11: Demonstration of the PIV median filter. (a) PIV vector field with a vector considered "spurious". (b) PIV vector field corrected.

cal two-plane data" (the first two are collectively called "single-plane data"). From Fig. 4.13, it is noticed that for 80 CAD bTDC and 65 CAD bTDC, less than 4.5% of the image pairs were discarded. However, much more image pairs were discarded at 115 CAD bTDC, both for the single-plane data and the numerical two-plane data. This indicates that strong out-of-plane flow motion likely exists at 115 CAD bTDC, especially on the lower plane which is closer to the piston. It is worth pointing out that the numerical two-plane dataset does not have more discarded images, suggesting that the two-plane crosstalk is not leading to PIV loss-of-correlation and not causing more images to be discarded.

The PIV measurement results of the numerically added images are compared against the results of the corresponding single-plane images, in the same way as Equation 3.12 and 3.13. As shown in Fig. 4.14, the measurement error at 115 CAD bTDC is obviously larger than the errors at the other two crank angles. At 115 CAD bTDC, less than 7% of all vectors have an absolute error of either component larger than 0.2 pixels / dt. At 80 CAD bTDC, less than 2% of all vectors have an absolute error of either component larger than 0.2 pixels / dt. At 65 CAD bTDC, less than 3% of all vectors have an

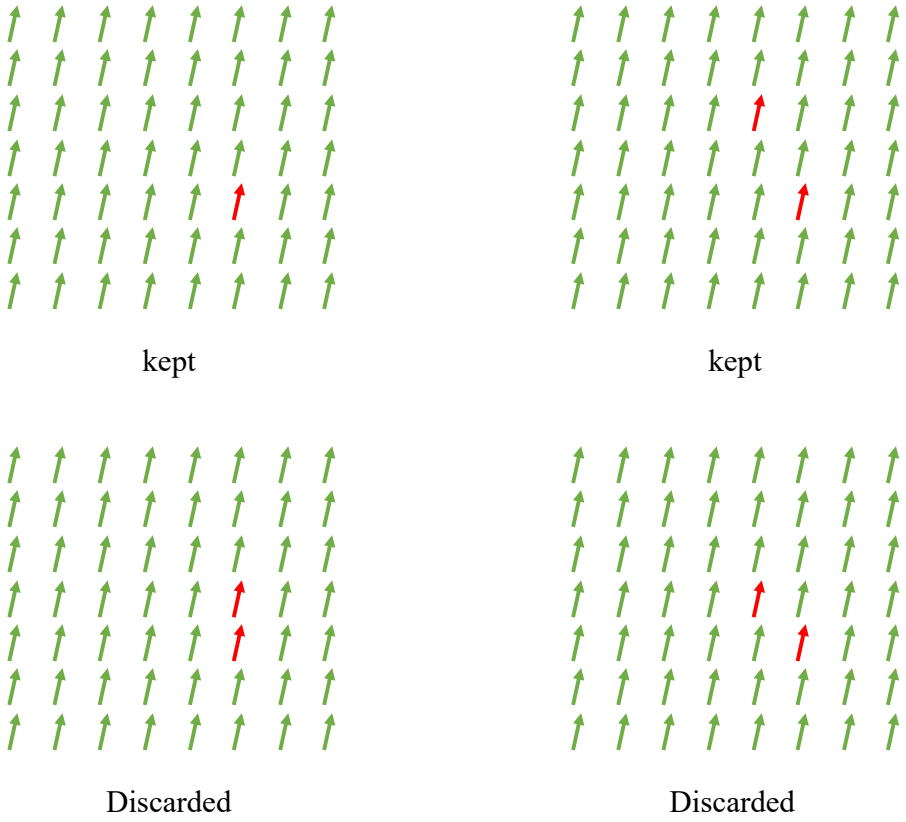

Figure 4.12: A demonstration of the discarded image pairs, in which adjacent spurious vectors exist.

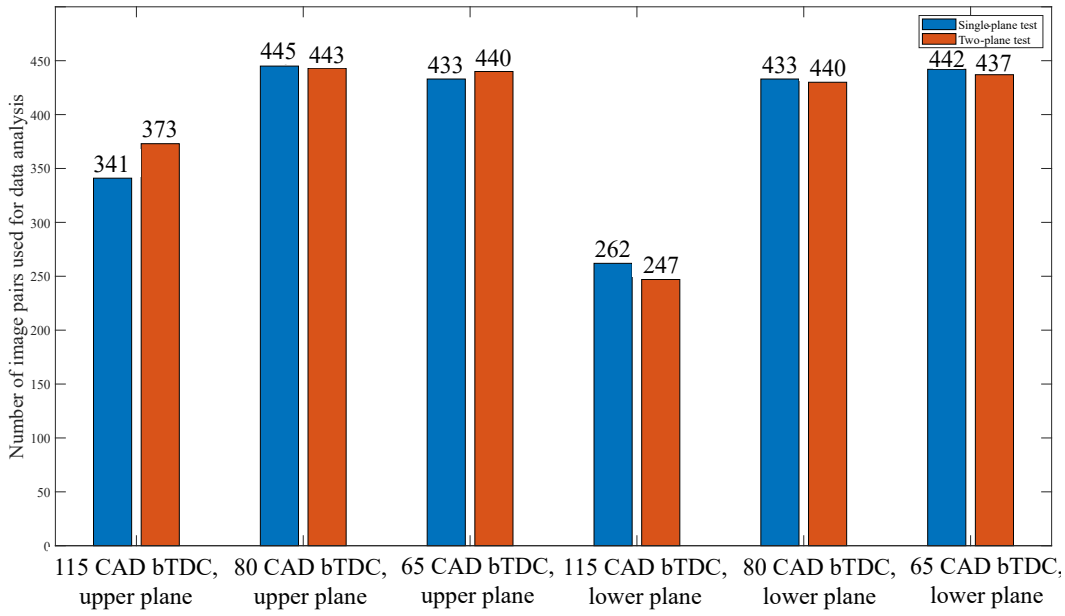

Figure 4.13: Numbers of image pairs used for data analysis, out of 450 cycles.

absolute error of either component larger than 0.2 pixels / dt. From Fig. 4.14, it can also be seen that the measurement error of the horizontal (u) component is larger than the vertical (v) component, which aligns with the findings in Chapter 3, stemming from the "arc" shapes of the defocused particle images. Here, it is worth mentioning that the notation "horizontal (u)" and "vertical (v)" components are based on the camera view (i.e. horizontal and vertical in the images), as in the previous chapter, but not based on the engine geometry where "vertical" means out-of-plane direction.

The absolute errors of all vectors on the upper plane at 115 CAD bTDC and 80 CAD bTDC are shown as scatter plots in Fig. 4.15. The cross (red) markers indicate the vectors located at the edges of the vector fields. The dot (blue) markers indicate the rest of the vectors. The plots show that at both 115 CAD bTDC and 80 CAD bTDC, the vectors at the edges of the vector fields tend to have larger errors. It should be because the PIV algorithm cannot search for matched particles outside the interrogation area, contributing to more loss-of-correlation.

As a summary and discussion, this section evaluates the measurement error caused

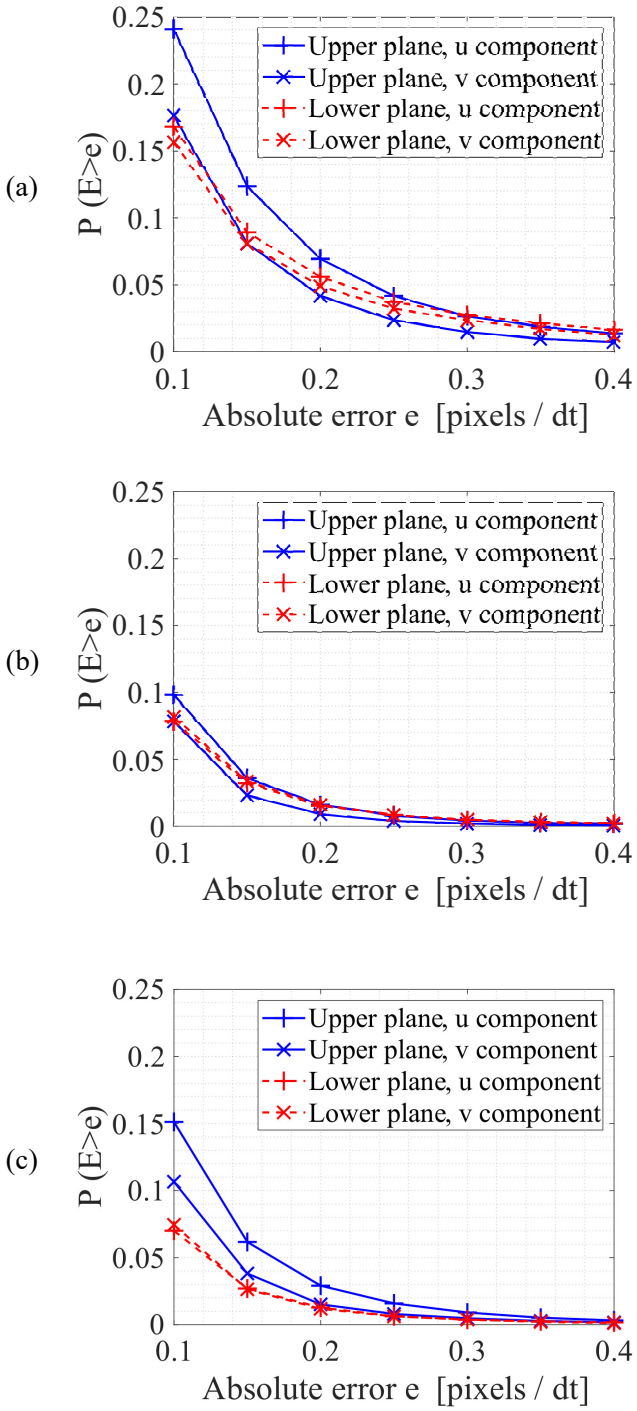

Figure 4.14: The complementary cumulative distribution function of vector error E [pix/dt] at: (a) 115 CAD bTDC; (b) 80 CAD bTDC; (c) 65 CAD bTDC. Note that the error at 115 CAD bTDC is larger than the errors at the other two crank angles.

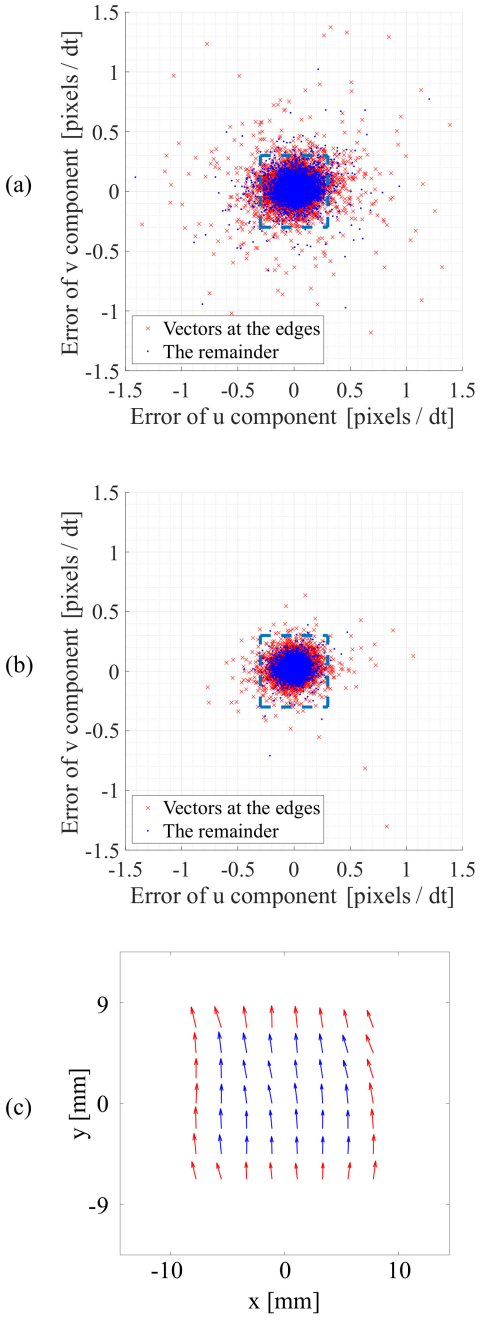

Figure 4.15: Scatter plots of the absolute errors of all vectors on the upper plane at: (a) 115 CAD bTDC; (b) 80 CAD bTDC. Each marker corresponds to one vector. The dash boxes mark errors within ± 0.3 pixels / *dt*. The cross (red) markers indicate the vectors located at the edges of the vector fields; the dot (blue) markers indicate the rest of the vectors, as illustrated in (c). Note that the vectors at the edges of the vector fields tend to have larger errors.

by two-plane crosstalk, by numerically adding single-plane illuminated images, and comparing the PIV results of the numerical two-plane dataset with the results of the single-plane dataset. A median filter was used for validating and correcting the vector fields of all datasets. Any image pairs where adjacent spurious vectors exist were discarded, which indicates that the discarded image pairs suffer from strong PIV loss of correlation. It was shown that the two-plane crosstalk should not be responsible for the loss of correlation. This section evaluates the datasets at three CAD. Considering that there were negligible discarded images at two of the three CAD, which means the PIV hardware setup and cross-correlation process should be reasonable, the thesis author attributed the strong PIV loss of correlation at 115 CAD bTDC to potentially strong out-of-plane flow motions. Fig. 4.14 presented the two-plane crosstalk error, which overall aligns with the evaluation results in Chapter 3 where a similar camera working distance (thereby depth of field) was used. Fig. 4.14 also showed that the measurement error of 115 CAD bTDC is obviously larger than the other two CAD, suggesting that stronger out-of-plane flow motions should be responsible for increasing the measurement error caused by the out-of-focus particles. More parametric study on the influence of out-of-plane motions on the two-plane crosstalk is warranted in future. Fig. 4.15 showed that the PIV vectors at the edges of the vector fields tend to have larger errors, which was another evidence on the influence of PIV loss of correlation.

4.7 Instantaneous flow measurement on the two planes

Fig. 4.16 shows the ensemble average flow fields on the upper plane and the lower plane in the simultaneous two-plane test. The origin (0,0) is the centre of the swirl plane. Since the velocity magnitudes differ greatly for different crank angles and planes, the colour maps do not readily indicate the detail of the velocity magnitudes. The overlaid vector arrows share the same scale, for a more convenient comparison.

From the average fields, it can be seen that when the piston is low (115 CAD bTDC),

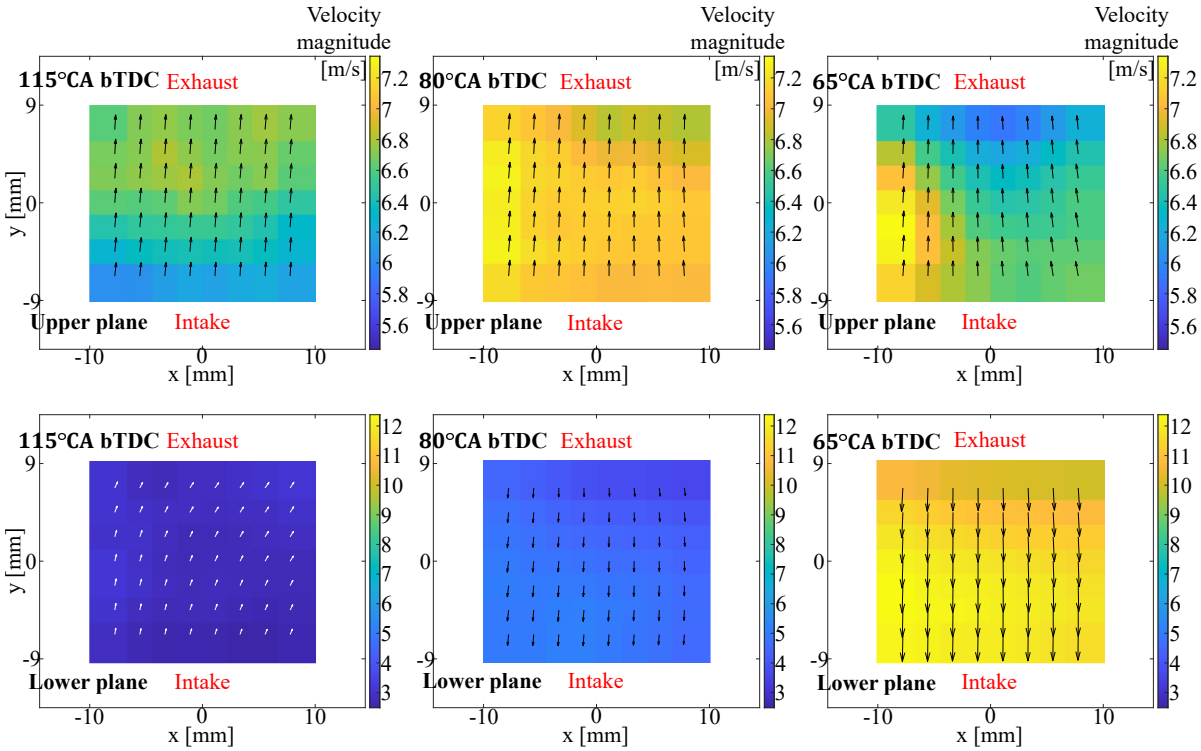

Figure 4.16: The ensemble average velocity fields. Note that the colorbar scale is different for the two planes. The vectors have the same scale for each image. At 115 CAD bTDC, the average flow direction on both planes is from the intake to the exhaust valves. At 80 CAD and 65 CAD bTDC, the two planes have opposite average flow directions.

the tumble vortex centre is below the lower plane, so that the average flow direction on both planes is from the intake valves to the exhaust valves. As the piston rises to 80 CAD bTDC, the vortex centre has travelled across the lower plane. When the piston is higher (65 CAD bTDC), the vortex centre is in the middle of the two planes, so that the two planes have opposite average flow directions. However, the magnitudes of the average velocities on the lower plane at both 115 CAD bTDC and 80 CAD bTDC are low. Due to cyclic variation, the tumble vortex centre may be at a different height in each individual cycle, even at the same crank angle. The average flow fields conceal whether the low velocity magnitudes are due to flow physics, or the varying flow motions in each individual cycle being averaged.

Fig. 4.17 and Fig. 4.18 show the **instantaneous** flow fields from two individual cycles. In Cycle A (Fig. 4.17), at 115 CAD bTDC, the tumble vortex centre lies below the two planes. At 80 CAD bTDC, the vortex centre aligns near the lower plane. The swirl flow structure is also revealed on the lower plane. However in Cycle B (Fig. 4.18), at 115 CAD bTDC, the flow direction on the lower plane has already started to reverse, indicating that the tumble vortex centre is already above the lower plane. The two-plane PIV measurement therefore enables the instantaneous swirl flow structures on two planes, and the tumble vortex travel, to be measured simultaneously. The two-plane PIV measurement also highlights that average flow fields (Fig. 4.16) may be misleading due to CCV. It is noted that when evaluating the ensemble average fields to study CCV in details, the RMS velocities are typically used alongside. As a demonstration of the two-plane technique, the RMS velocities are not discussed in this section.

4.8 Summary

This chapter explored the application of the proposed defocusing based PIV in a real and complex flow device, an optical engine. The instantaneous swirl flow structures on two swirl planes, and the tumble vortex travel along the cylinder axis, are able to be

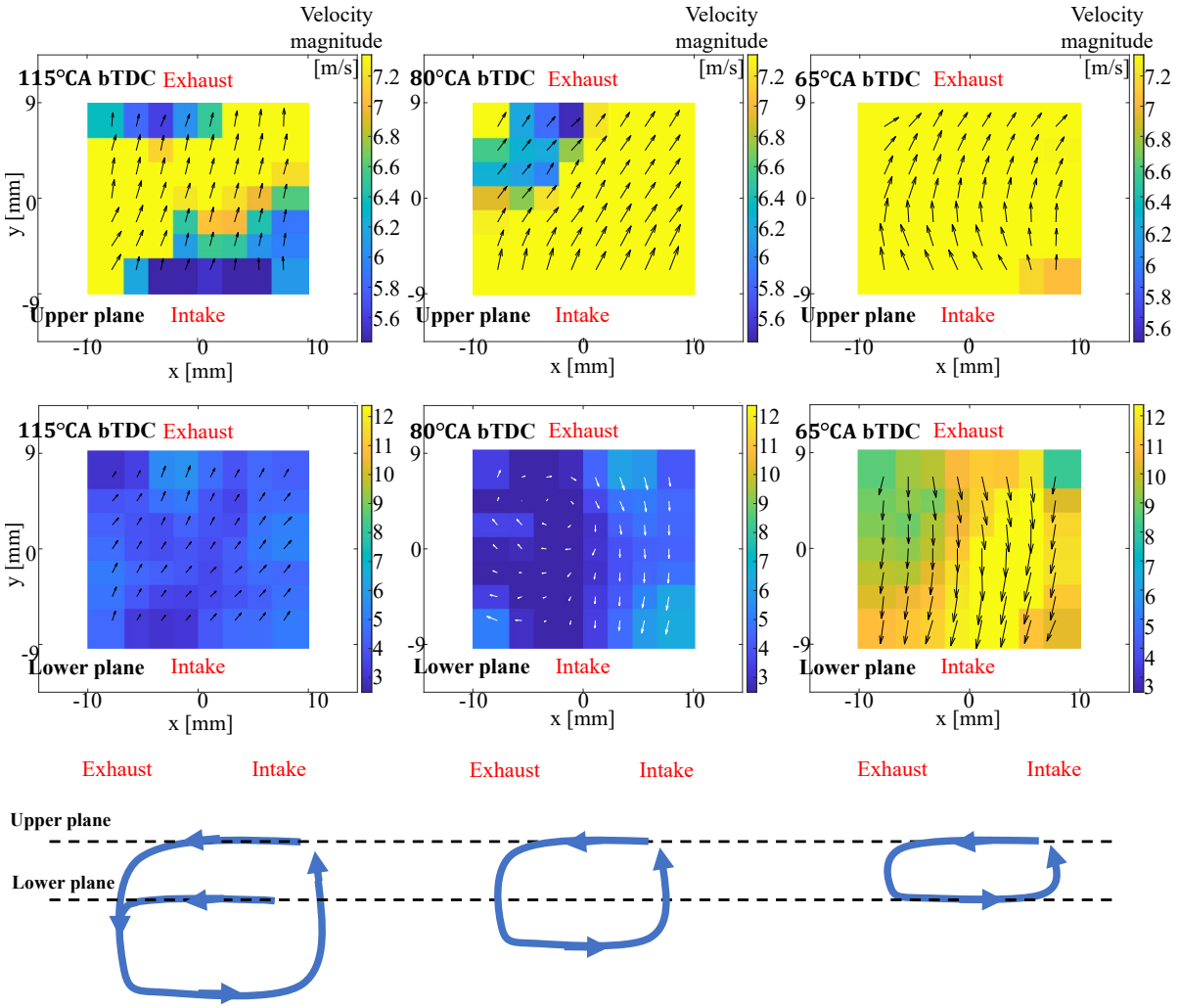

Figure 4.17: The instantaneous velocity fields of Cycle A. At 115 CAD bTDC, the tumble vortex centre is below the lower plane. At 80 CAD bTDC, the tumble vortex centre aligns with the lower plane.

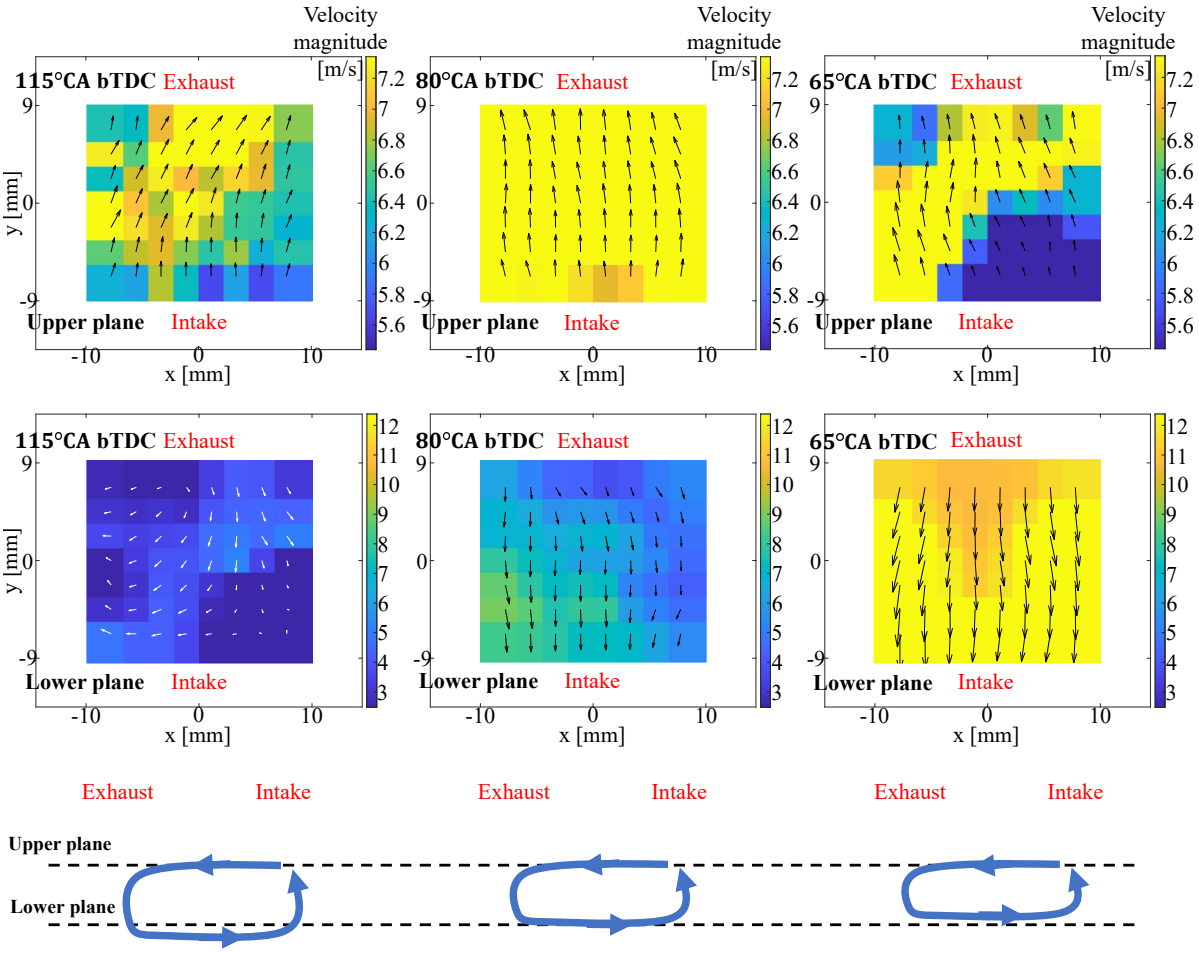

Figure 4.18: The instantaneous velocity fields of Cycle B. At 115 CAD bTDC, the tumble vortex centre has travelled across the lower plane.

resolved using a typical standard single-plane PIV system (with one PIV laser and one camera). The two-plane crosstalk was evaluated by numerically adding single-plane illuminated images. Overall, the two-plane crosstalk was found to match the results in Chapter 3 where a similar depth of field was achieved, but also indicated the influence of PIV loss of correlation and out-of-plane flow motions. More parametric study (either numerical or experimental) on the effect of out-of-plane flow motion is warranted in future.

The work in this chapter is the first application of macroscopic defocusing PIV in a practical flow device where optical access is limited. The seeding density used in this work is a typical high seeding density of single-plane PIV. It demonstrates the potential of modifying a standard single-plane PIV system based on the image splitting device, to enable simultaneous PIV measurement on at least two planes. In principle, the defocusing approach could be combined with the polarisation/wavelength approach, to enable simultaneous multi-plane measurements on more planes.

Chapter 5

Two-plane Flame Front Detection

This chapter presents the first simultaneous two-plane flame front detection using defocusing PIV. The Chapter begins with introducing the experimental setup and test condition. A novel two-step filter is designed, to effectively remove the out-of-focus particle images, while keeping the in-focus particle images. The two-step filter allows the turbulent flame fronts on two planes to be tracked simultaneously. In order to evaluate the two-plane crosstalk, single-plane illumination images were numerically added, to compare the flame front contours generated from ground-truth single-plane illumination image, with the contours generated from numerically-added "two-plane" images. The work in this chapter builds the foundation for the four-plane flame measurement in the next chapter.

The work in this chapter is published in [88].

5.1 Experimental Setup and Test Condition

The test setup is presented in Fig. 5.1. It is almost the same to Fig. 4.4. Two swirl planes were illuminated. The upper plane was 2.5 mm below the firing deck. The lower plane was 22 mm below the upper plane. A dichroic filter (Elliot Scientific CDG-5051) was used to reject the chemiluminescence emissions from the flames, and transmit the

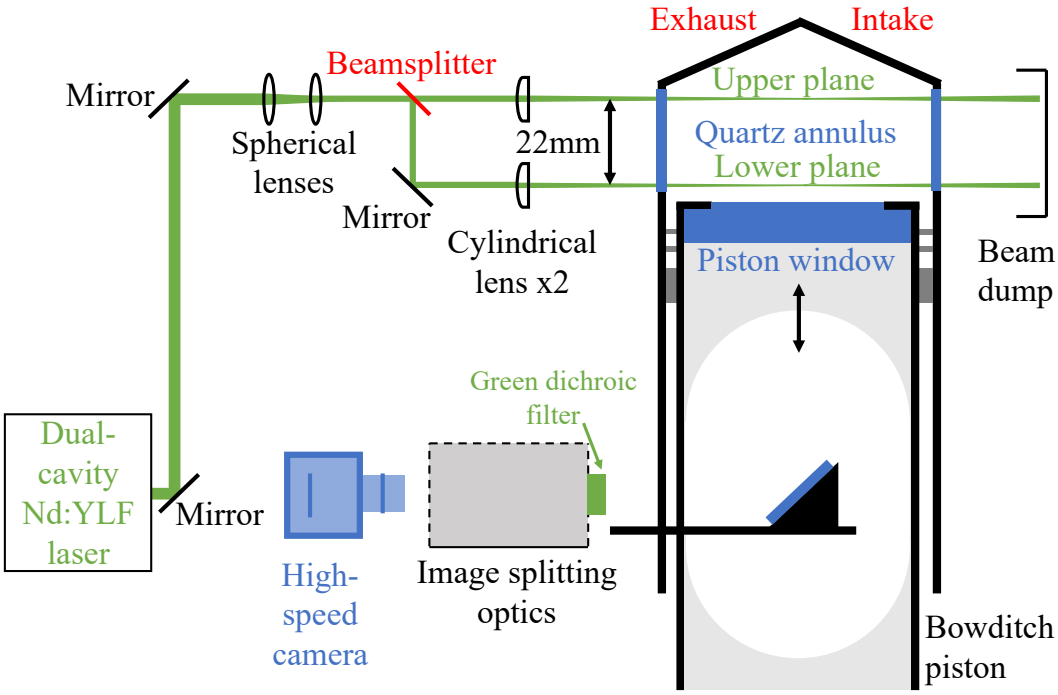

Figure 5.1: Schematic of the test setup for in-cylinder two-plane flame front detection.

Table 5.1: Engine test condition for the two-plane flame front measurement.

Engine speed	1000 rpm
Intake air temperature	303 K
Intake air volume flow rate	1.00 L / s
Fuel	iso-octane (stoichiometric)
Fuel injection timing	280 CAD bTDC
Spark ignition timing	15 CAD after TDC (aTDC)

green Mie scatter from the PIV particles. Table 5.1 presents the test condition. In this experiment, the ignition timing was much later compared to the normal working conditions of an SI engine. This is because in this setup, the measurement had to be taken when the piston was below the lower plane, otherwise the piston would block the laser sheet on the lower plane. In this engine geometry, the two-plane flame front measurement had to take place after 55 CAD after Top Dead Centre (aTDC). It was found that if a normal ignition timing was used, the flame would consume all seeding particles in the chamber at 55 CAD aTDC, for most cycles. Therefore, a late ignition

timing was used. The 15 CAD aTDC ignition timing was determined based on trial and error. It guaranteed that flame contours could be seen on two planes for most cycles, and the combustion would not start too late to cause any potential damage to the exhaust systems, which was evaluated by the in-cylinder peak pressure CAD vs the exhaust valves opening CAD. As a demonstration of the two-plane flame front technique, deviation from normal engine working conditions should not be an issue. It also highlights that when applying PIV approach for flame front tracking in an optical engine, delivering the laser sheets through the piston window would be a better option in terms of enabling the use of relevant engine conditions.

5.2 Two-plane Flame Front Tracking

Fig. 5.2 and Fig. 5.3 show two consecutive images (75 and 80 CAD aTDC) from an engine cycle. To improve visualisation, the PIV images presented here were rotated so that the upper-plane image and the lower-plane image are vertically arranged. The same dynamic background subtraction filter as in Fig 4.9 was used to process the raw images and generate Fig. 5.2 (a) and Fig. 5.3 (a), which are the background subtracted images. Since the out-of-focus (blurry) particle images correspond to the low-frequency signals in the Fourier domain, the same high-pass filter (32 $\times$ 32 window size) as in Chapter 3 was used to process the images, as in Fig. 5.2 (b) and Fig. 5.3 (b). It is noticed that the high-pass filter was able to remove a substantial fraction of the blurry particle images, but some of them still remain. Therefore the thesis author designed a two-step filter to clean up the blurry particle images.

5.2.1 Ratiometric Coefficient of Variation Filter

The first step is called a Ratiometric Coefficient of Variation Filter (RCOVF). First, a 5 $\times$ 5 window is used to calculate the local Coefficient of Variation (COV) for each pixel:

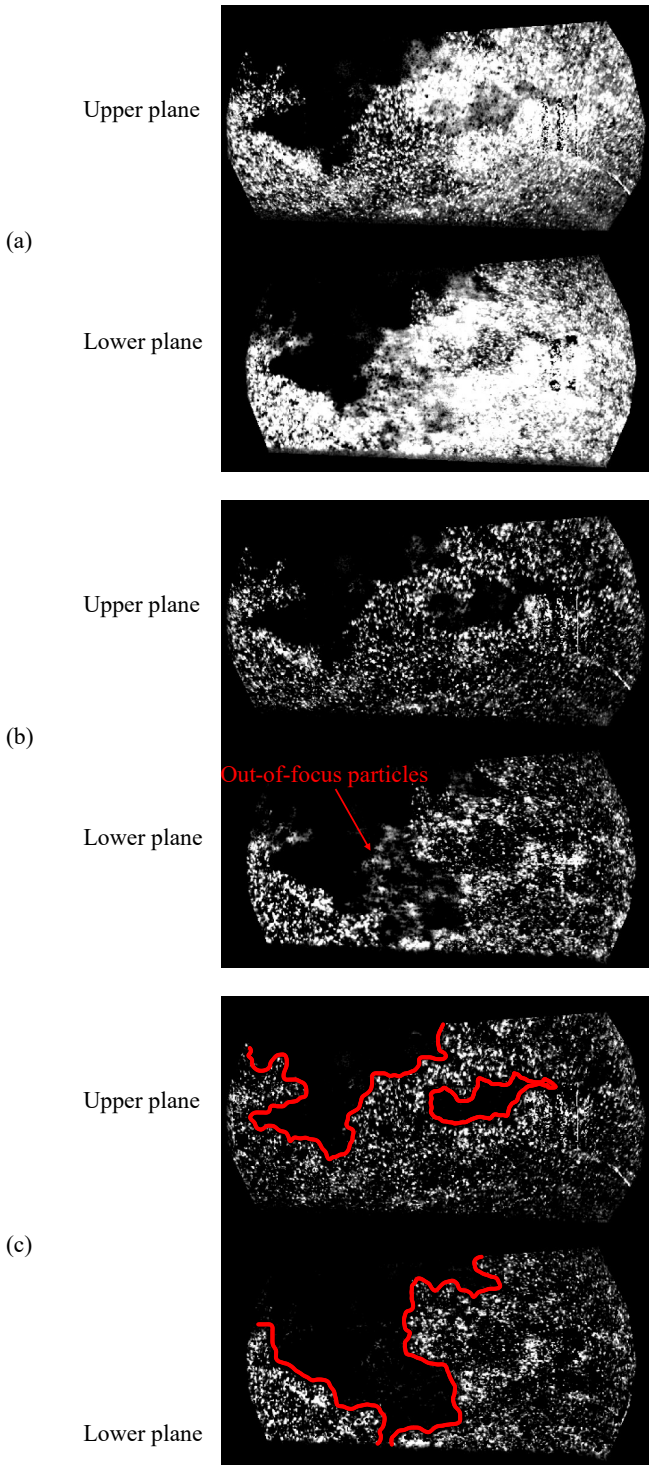

Figure 5.2: A two-plane flame front detection example (75 CAD aTDC). (a) Background subtracted image. (b) High-pass filtered image. (c) Image after two-step filtering.

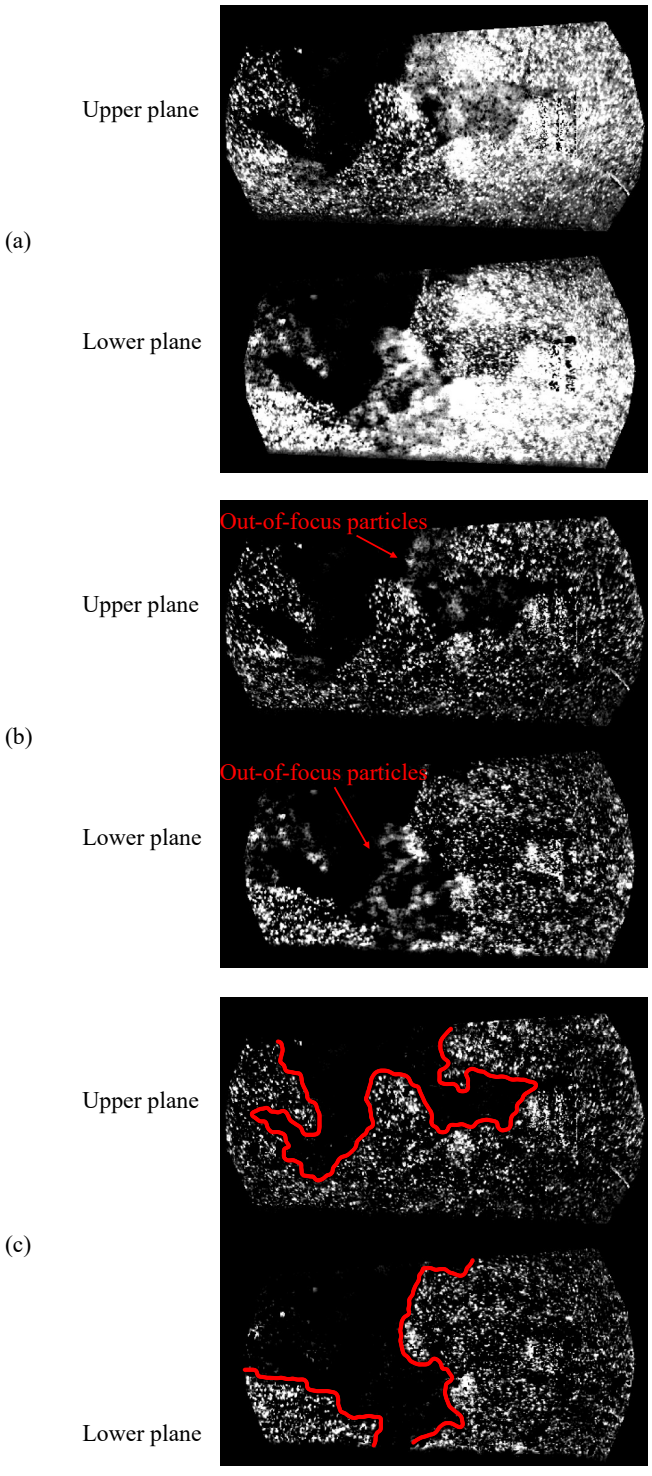

Figure 5.3: A two-plane flame front detection example (80 CAD aTDC). (a) Background subtracted image. (b) High-pass filtered image. (c) Image after two-step filtering.

$$C_v(i,j) = \frac{\sigma(i-2:i+2, j-2:j+2)}{\mu(i-2:i+2, j-2:j+2)}, \tag{5.1}$$

in which i and j denote the pixel's coordinates, σ and μ refer to standard deviation and mean. The COV evaluates how "even" the pixel intensity spreads across the local region. In an area where only out-of-focus particle images exist, the local COV is much smaller than that in areas occupied by just in-focus particles. Note that if out-of-focus particles are seen on one of the two planes, corresponding in-focus particles are then found on the other plane in a region which has the same in-plane world coordinates. That means for areas where particles only exist on one of the two planes, the local COV values from both images should have a relatively large difference. For areas where particles exist on both planes, the local COV values in both images are similar. Therefore the ratio of the local COV from both images can be used to remove certain pixels considered to contain only out-of-focus particle images, by applying the RCOVF defined in Algorithm 2.

Algorithm 2 Ratiometric Coefficient of Variation Filter (RCOVF)

procedure RCOVF(i_u, j_u) ▷ Filter the upper-plane image (subscript u)
  if $\frac{C_v(i_u,j_u)}{C_v(i_l,j_l)} < 0.5$ **then**
    $I(i_u, j_u) = 0$

procedure RCOVF(i_l, j_l) ▷ Filter the lower-plane image (subscript l)
  if $\frac{C_v(i_l,j_l)}{C_v(i_u,j_u)} < 0.5$ **then**
    $I(i_l, j_l) = 0$

To be specific, the RCOVF was independently applied to the images from the two planes. Take the upper plane image as an example. For each pixel in the region of interest in the upper plane image, the local COV was first calculated. In the camera calibration process, the exactly same calibration grid was imaged on the two planes (see Section 4.5.1, the height of the same grid on the piston window was positioned by turning the crank shaft by hand). A pinhole model calibration was performed by the LaVision PIV software DaVis 8.4. After image correction, a linear relation between

pixel and real dimension (mm) was provided on each plane, with the same in-plane origin. Based on the pixel-to-mm relations, each pixel on the upper plane image could be matched with a pixel on the lower-plane image. This was done by converting the pixel coordinate into mm on the upper plane, and then calculating the corresponding pixel coordinate on the lower plane. The calculated pixel coordinate on the lower plane was not integer. In this work, the closest pixel was chosen as the corresponding pixel, so that no pixel interpolation was performed. If the ratio of the local COV of the upper-plane pixel to the local COV of the lower-plane pixel $\frac{C_v(i_u,j_u)}{C_v(i_l,j_l)}$ was smaller than 0.5, that upper-plane pixel was considered to be occupied by just blurry particles and was cleaned, $I(i_u, j_u) = 0$. The same evaluation was repeated for every pixel on the upper plane. Then the same process was performed on the lower plane. It is noted that the local COV window size 5×5, and the COV ratio threshold 0.5 were determined based on trials. They were related to the patterns/shapes of the out-of-focus particles. Although the values were chosen based on experience, the same values were used for a large dataset evaluation in Section 5.3.

5.2.2 Ratiometric Sliding Maximum Intensity Filter

In practice, the RCOVF performs well in removing the central part of an out-of-focus image "blob", but it is not able to effectively remove the edges of the out-of-focus particle images. See Fig. 5.4 for an example of the RCOVF "central removing" effect. This is because the COV alone is not good at discriminating the edges of in-focus particles and the edges of out-of-focus particles. Therefore, a second step called Ratiometric Sliding Maximum Intensity Filter (RSMIF) was applied. It is based on the observation that for those bright out-of-focus particles which survive high-pass filtering, there should be corresponding bright in-focus particles on the other plane. The filter is defined in Algorithm 3, where S is the sliding maximum intensity value of each pixel calculated using a 13×13 window:

$$S(i, j) = \max \{I(i - 6 : i + 6, j - 6 : j + 6)\} . \tag{5.2}$$

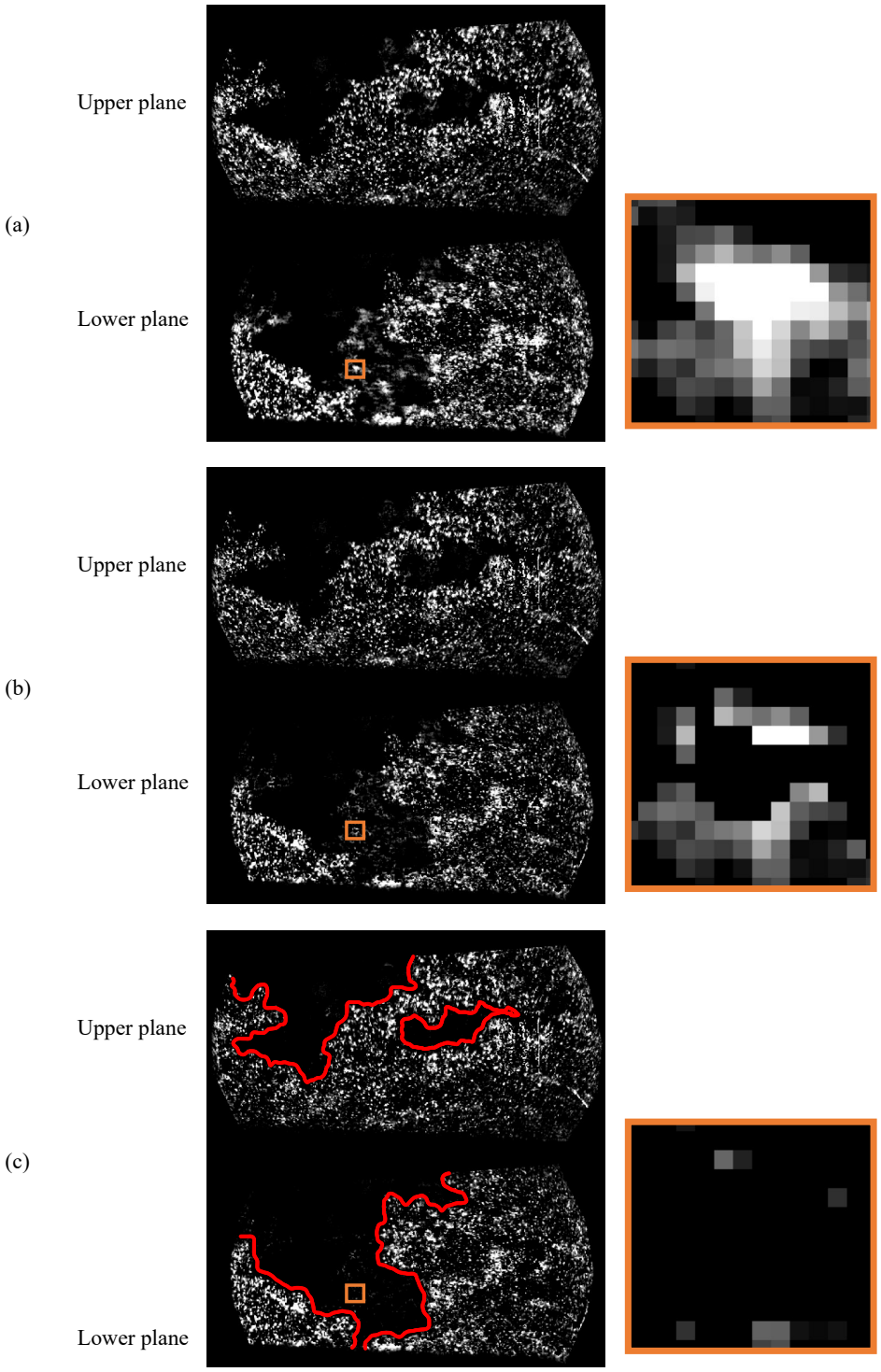

Figure 5.4: An example of the RCOVF "central removing" effect. (a) High-pass filtered image. (b) Image after RCOVF. (c) Image after RSMIF. Note the enlarged views of a representative out-of-focus particle.

Algorithm 3 Ratiometric Sliding Maximum Intensity Filter (RSMIF)

procedure RSMIF(i_u, j_u) ▷ Filter the upper-plane image (subscript u)
  if $\frac{S(i_u,j_u)}{S(i_l,j_l)} < 0.5$ AND $\frac{C_v(i_u,j_u)}{C_v(i_l,j_l)} < 1$ **then**
    $I(i_u, j_u) = 0$

procedure RSMIF(i_l, j_l) ▷ Filter the lower-plane image (subscript l)
  if $\frac{S(i_l,j_l)}{S(i_u,j_u)} < 0.5$ AND $\frac{C_v(i_l,j_l)}{C_v(i_u,j_u)} < 1$ **then**
    $I(i_l, j_l) = 0$

In this filter, the ratio of the sliding maximum intensity value is used to evaluate if a pixel is a part of the edge of an out-of-focus particle image. Due to the inherent brightness difference of in-focus particle images, caused by e.g. the different physical sizes of in-focus particles and the spatial distribution of laser sheet energy, the sliding maximum intensity ratio alone is not a fair evaluation criteria. The second condition on the COV ratio was used to prevent removing pixels in regions where in-focus particles exist on both planes. Again, the window size and the threshold values were chosen based on trials, but they were kept the same for a large dataset evaluation.

The effect of the two-step filter is visualised in Fig. 5.2 (c) and Fig. 5.3 (c). Direct observation of the images shows that the out-of-focus particles were removed satisfactorily. Based on the filtered images, turbulent flame front contours were determined using the automatic histogram-based threshold approach proposed by [50], as described as follows.

5.2.3 Flame Front Tracking Approach

The automatic histogram-based threshold approach begins with processing the image with a 3 × 3 sliding maximum filter. The window size 3 × 3 was chosen based on the diameter of the in-focus particle image. Then the local average intensity of each pixel in the region of interest was calculated using a 17 × 17 window. The local average intensity of each pixel was then used to create a histogram, using the Matlab histogram function with automatic bin width. In the histogram, a nearly

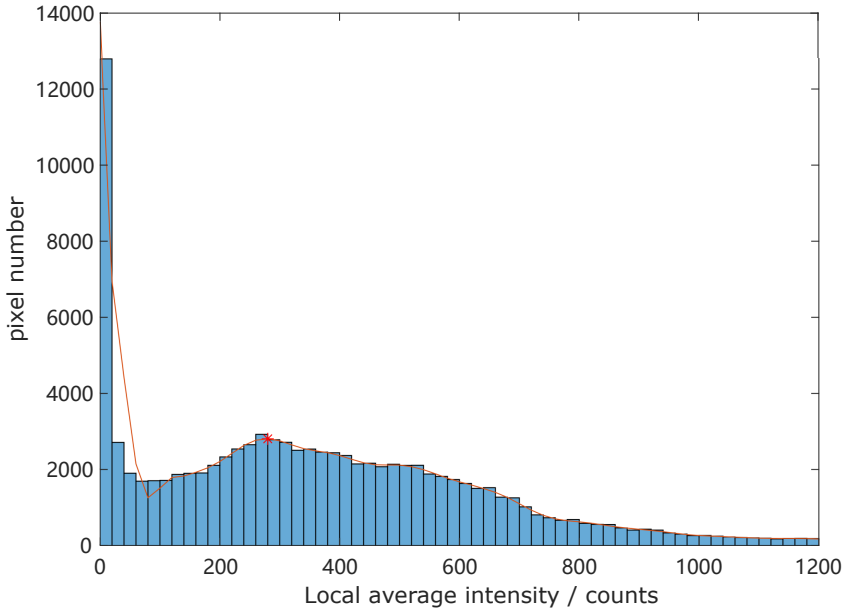

Figure 5.5: The histogram function of local average intensity, of Fig. 5.2 (c), upper plane.

bimodal density distribution with two distinct maxima was observed (See Fig. 5.5 for an example). The first maxima at 0 intensity indicates the absolutely burned region, which is dark. To distinguish between unburned and burned density, a threshold was automatically determined for each image, which should be located between the two maxima, following the method in [50]. The histogram function was smoothed using a quadratic regression over a window of 11 bins. Then a cubic spline interpolation was applied (e.g. the red curve in Fig. 5.5). The Matlab islocalmax function was used to locate the second maxima. The threshold was set to be the arithmetic mean value of the first maxima (0 in this work) and the second maxima. Binarisation was performed for each pixel. Any pixel with a local average intensity below the threshold was considered "burned", otherwise "unburned". A Matlab function bwboundaries was used to detect the flame boundaries between the burned and unburned regions. The generated flame contours were smoothed using a quadratic regression over a window size of 15 points. Examples of the overlaid flame contours on particle images are shown in Fig. 5.2 (c) and Fig. 5.3 (c).

5.3 Two-plane Crosstalk Evaluation

As discussed in the previous section, several empirical parameters were used in the two-step filter, such as the window sizes and the ratio thresholds. These parameters were decided to achieve a good balance between cleaning out-of-focus particles and keeping in-focus particles. To evaluate the flame front detection uncertainty caused by the out-of-focus images, single-plane illumination tests were performed, as in Chapter 4. Single-plane illumination images were numerically added, to compare the flame front contours generated from the numerically-added "two-plane " images, with the contours generated from the ground-truth single-plane illumination images. Throughout this section, the flame front contours generated from the in-focus single-plane illumination images are called "ground-truth" results, because they should most accurately track the flame front position. As discussed in Chapter 3, the shapes of the out-of-focus particle images on the transmitted-side and the reflected-side are different. Therefore, the evaluation was performed independently on the two planes. Fig. 5.6 presents the evaluation on the upper plane. A upper-plane illumination image was selected and numerically added to 100 lower-plane illumination images to create 100 "two-plane illumination" images. Fig. 5.7 presents the probability density map of the unburned region calculated from the numerically-added images, with the ground-truth flame contour overlaid. If each of the numerical two-plane images could provide exactly the same flame contour to the ground-truth one, every pixel in the probability density map below the ground-truth contour (red) should be yellow (i.e. 100% unburned), and everything above the ground-truth contour should be black (i.e. 100% burned). However, due to the two-plane cross-talk and imperfect image processing, the filter could occasionally erase in-focus images, while sometimes ignored out-of-focus images. The purpose of the probability density map is to evaluate this "imperfection". In Fig. 5.7, it is noticed that more than 95% of the two-plane images were able to resolve the unburned region. Less than 35% of the two-plane images slightly expanded the unburned region (indicated by the cyan region, which has a width of $<$1 mm). The same evaluation was performed on the lower plane, as presented in Fig. 5.8. The

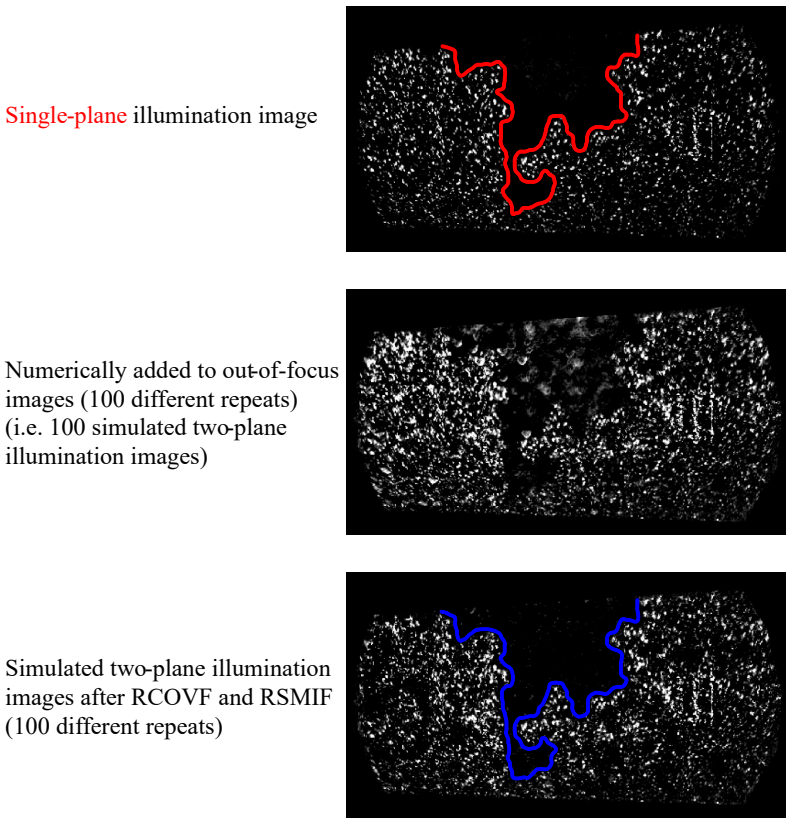

Figure 5.6: Demonstration of two-plane crosstalk evaluation on the upper plane.

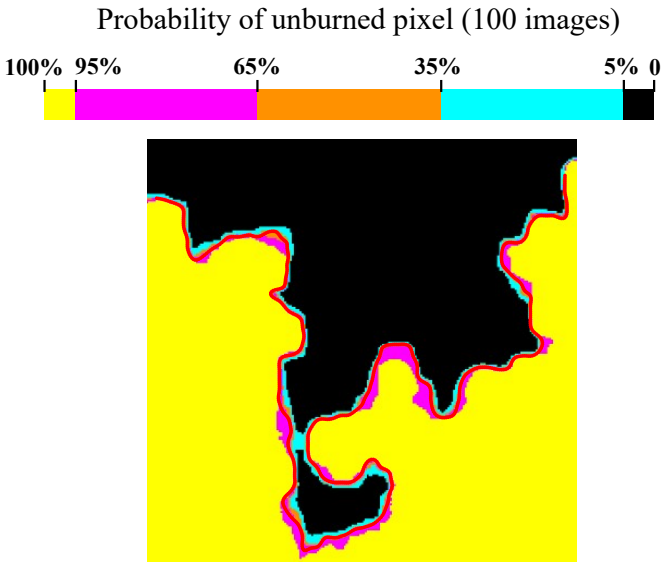

Figure 5.7: The probability density map of unburned pixel in 100 numerical "two-plane" images. The ground-truth single-plane illumination image was from the upper plane.

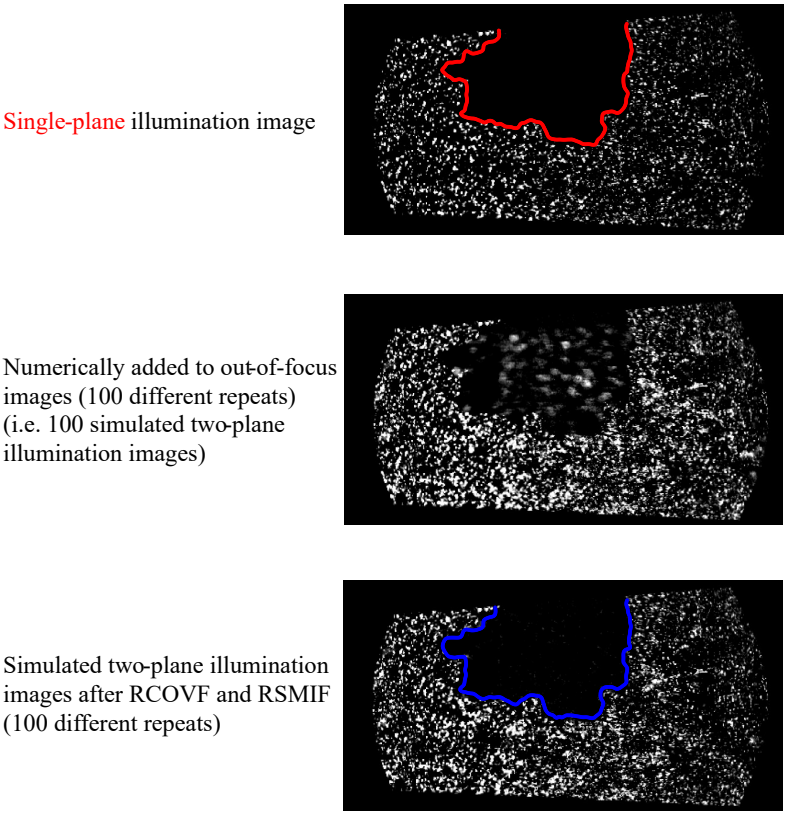

Figure 5.8: Demonstration of two-plane crosstalk evaluation on the lower plane.

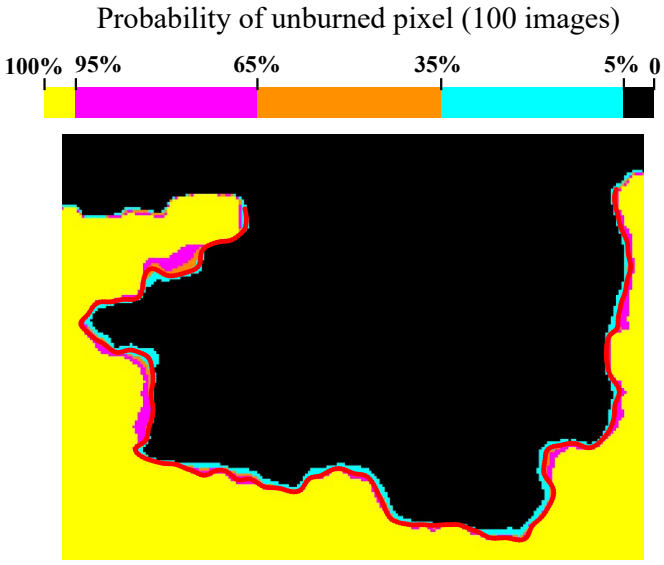

Figure 5.9: The probability density map of unburned pixel in 100 numerical "two-plane" images. The ground-truth single-plane illumination image was from the lower plane.

probability density map of the unburned region calculated from the numerically-added images was shown in Fig. 5.9. Again, the same conclusion, that more than 95% of the two-plane images were able to resolve the unburned region, could be given.

To further examine the impact of the crosstalk on the structure of the measured flame front, the following evaluations are performed on the ground-truth flame front and the 100 numerically-generated flame fronts of Fig. 5.9. First, the x and y coordinates of the points on the flame fronts were parameterised using arc length. Using the Matlab interp1 function, spline interpolations of the flame front points were performed based on specifying a smaller arc length step (0.5 pixel in this work). On average, the interpolation process approximately tripled the number of points on each flame front. For each point on the ground-truth flame front, the curvature was calculated, by parameterising the point and its neighbouring points using a quadratic equation [89].

For each point along the path, the intersections of the path normal with the 100 numerically-generated flame fronts could be located, based on which the distances between the point on the ground-truth flame front and the intersection points on the numerically-added flame fronts were calculated. For each distance, it is defined to be positive if the intersection point is located in the burned region specified by the ground-truth flame image, which indicates the two-step filter is "generous" and not able to effectively remove the out-of-focus noise. It is negative otherwise, which is an indication of the two-step filter being "aggressive" and consuming unburned pixels. The average distance between the point on the ground-truth flame front and the intersection points on the 100 numerically-generated flame fronts is used to indicate the average "offset" of that point. Fig. 5.10 (a) demonstrates the determination of point offset. The red curve is a part of the ground-truth flame front, the blue curve is a part of one of the numerically generated flame fronts. Fig. 5.10 (b) plots the average offset of each point on the ground-truth flame front, versus the curvature of the point. On average, for points with positive curvatures (e.g. points A and B in Fig. 5.10 (c)), the offsets tend to be towards the burned region. This appears in the flame images as though the burned "valley" tends to be slightly filled. On the other hand, for points with negative curvatures (e.g. points C and D in Fig. 5.10 (c)), the offsets tend to be towards the unburned region, appearing like the unburned "peak" is slightly eroded. Considering the pixel magnification (7.12 pixels per mm), the average offset of each point on the real flame front is lower than 1 mm.

To inspect the change of flame front shape around individual characteristic points, four points are inspected, as shown in Fig. 5.10 (c). Points A and B have positive curvatures, while points C and D have negative curvatures. On the numerically-generated flame fronts, the small region containing each point is searched, to find the corresponding point with a maxima or minimum curvature. By searching the positions of the "new" characteristic points and knowing their curvatures, the shift of the four characteristics points on the ground-truth flame front and the changes of their curvatures can be calculated. As shown in Fig. 5.10 (c), for each characteristic point, the average

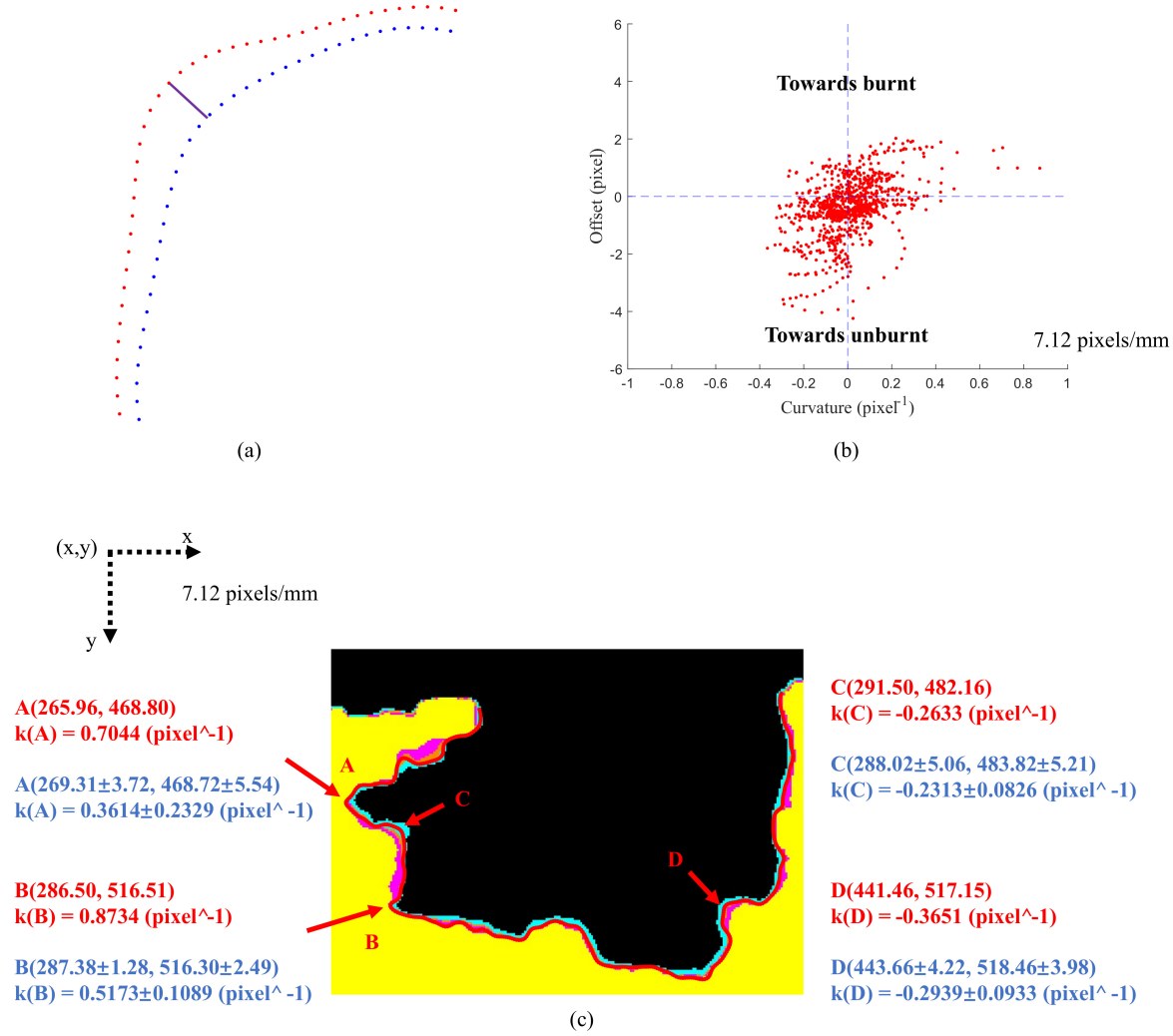

Figure 5.10: (a) Demonstration of determining the point offset. The red contour is a part of the ground-truth flame front, the blue contour is a part of one of the numerically-generated flame fronts. (b) The average offset of each point on the ground-truth flame front, versus the curvature of the point. The average offset is calculated over 100 numerically-generated flame fronts. (c) The average drifts of four characteristic points on the ground-truth flame front, and the average changes of their curvatures. The coordinate values are in the unit of pixel. For each characteristic point, the real coordinate and curvature, k, are shown first (red colour), followed by the average coordinate and curvature (blue colour), calculated over 100 numerically-generated flame fronts.

distances between the real characteristic points and the corresponding "drifted" characteristic points are smaller than 4 pixels (∼0.5 mm). Also, the average drift directions agree with the trends shown in Fig. 5.10 (b), i.e. the burned "valley" being filled, and the unburned "peak" being eroded. The average curvatures of the characteristic points on the numerically-generated flame fronts show that the shape of the flame front is well maintained.

5.4 Summary

This chapter demonstrates the first simultaneous two-plane flame front measurement using defocusing PIV. A novel two-step filter was specifically designed to effectively remove the out-of-focus particle images, while keeping the in-focus particle images. It was based on cross referencing the images from the two planes, making full use of the information provided by the out-of-focus particles. Single-plane illumination images were numerically added to evaluate the error caused by the "imperfect" filter. This chapter is a successful proof-of-concept of simultaneous multi-plane flame front tracking based on defocusing particle imaging, and is the foundation for the four-plane flame measurement in the next chapter.

Chapter 6

Four-plane Flame Detection

This chapter details the first example of four-plane flame front detection based on defocusing particle imaging. Based on using a single PIV laser, a compact and portable laser splitting device is designed to generate four laser sheets (10 mm depth offset), with each of them linearly polarised. Laser sheets with orthogonal polarisations were arranged in an interlaced pattern, which in principle allows a simultaneous four-plane measurement using defocusing and polarisation separations. To allow a much quicker and relatively easier alignment of small optical components, a 3D printed resin plate is designed.

Four-plane flame front tracking was performed in the optical engine. It is shown that the polarisation state of the scattered light would change in some areas within the region of interest. The polarisation state change is shown to be related to the lab jack pressure of the fused silica liner. Since polarisation discrimination is ineffective in this system, defocusing and temporal separation approaches were combined, to achieve a simultaneous two-plane measurement (defocusing) and a quasi-simultaneous four-plane measurement (temporal, 2 μs).

This chapter also investigates the local cycle-to-cycle variation (CCV) of combustion on the four sheets, by comparing the four-plane burn fractions to the pressure-derived Mass Fraction Burned (MFB) of the entire engine chamber. Similar to MFB, Planar Fraction Burned (PFB) is defined here, to quantify the fraction of pixels identified

as "burned" in the field of view. The overall combustion duration, defined as the time (in crank angle degrees) between 0.1 to 0.9 MFB, is typically considered to be an indicator of the overall CCV of an engine test point. In this work, the planar combustion duration on each plane, defined as the number of crank angle degrees (CADs) between 0.1 to 0.9 PFB, is used to explore the local CCV of combustion on each plane.

6.1 Laser Splitting Optics

Taking advantage of the fact that the laser beams from a two-cavity laser normally have orthogonal polarisations, a laser splitting device is proposed to generate four laser sheets based on a single PIV laser. As shown in Fig. 6.1, a Polarising Beamsplitter (PBS) is used to separate the laser beams from the two cavities. By using a pair of Non-Polarising Beamsplitter (NPBS) and several mirrors, four laser beams are generated. A long cylindrical lens is placed at the four-beam outlet to vertically expand the beams and generate four laser sheets. Two cameras, each with a set of image splitting optics, are used for imaging. Because of the polarisation filters fitted to the cameras, each camera could only see two of the four laser sheets. The interlaced pattern of laser sheets with orthogonal polarisations allows to halve the plane separation limited by defocusing. With similar working distance and field of view as in the previous chapter, a 10 mm plane separation could be achieved, which is about half of the already tested 22 mm separation.

A 10 mm separation between beams/sheets is a relatively narrow distance, generating challenges with optics and laser alignment. To address that, a 3D printed plate was designed to mount the laser splitting and sheet-forming optics. The 3D printed plate is shown in Fig. 6.2. Recesses on the plate were created to match the optics sizes and positions. Table 6.1 lists the optics used for four-sheet generation. The optics were held to the plate using Thorlabs clamping arms (PM4/M and PM3/M). To avoid creating threads in resin, the resin plate was fastened to an aluminium base board

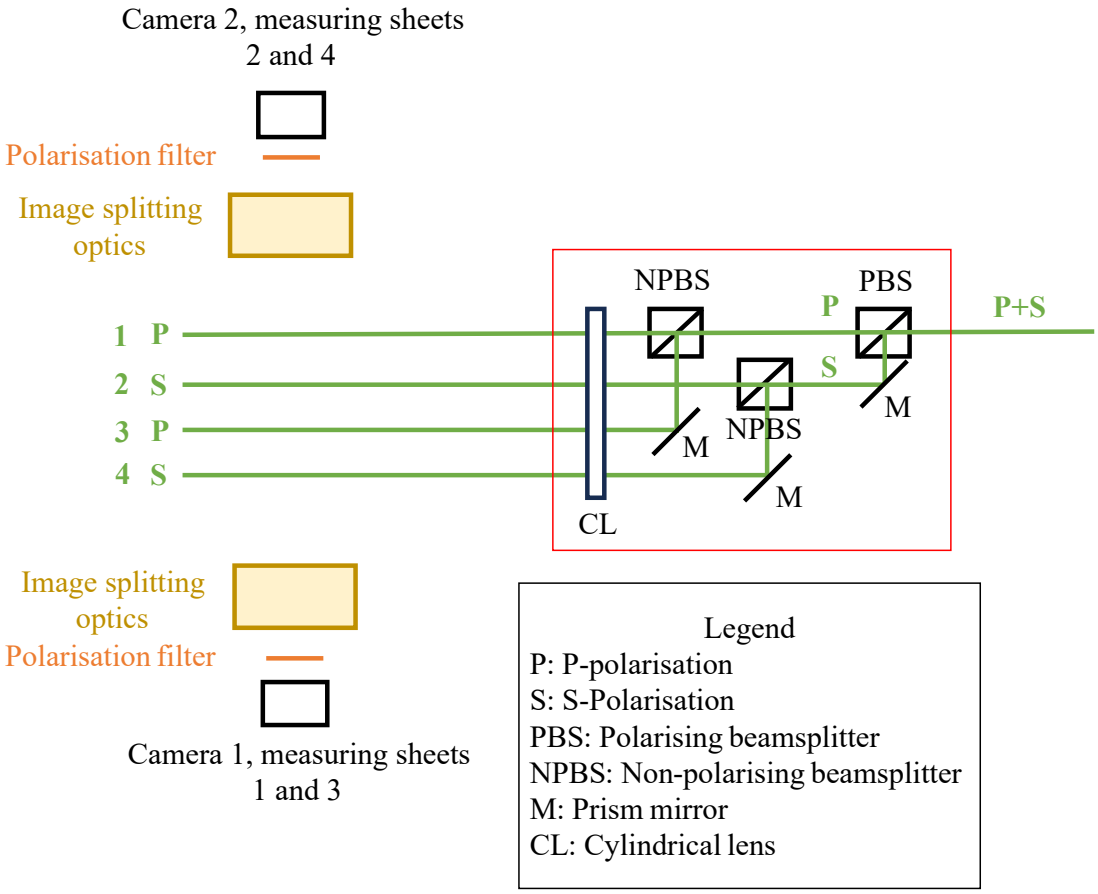

Figure 6.1: The optical setup for a four-plane flame tracking experiment.

Table 6.1: The optical components used for four-sheet generation.

PBS	10 mm cube, 532 nm, Edmund Optics #48571
NPBS	12.5 mm cube, 532 nm, Edmund Optics #35959
Mirror	10 mm triangular prism, 532 nm, Edmund Optics #37653
CL	25 mm × 50 mm, -150mm concave, Edmund Optics #68085

(a)

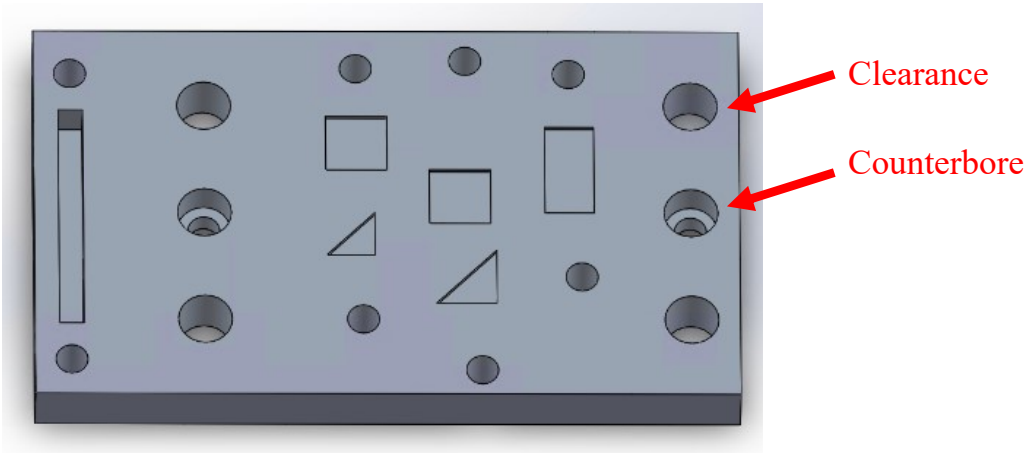

(b)

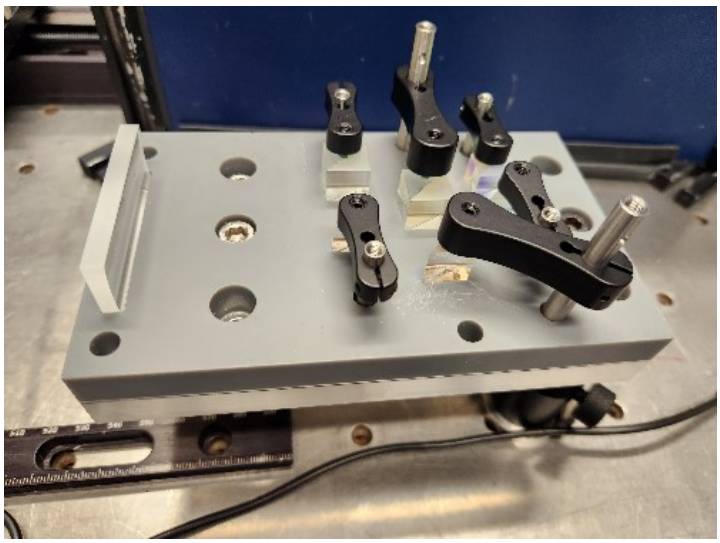

Figure 6.2: The 3D printed resin plate for mounting the four-sheet laser optics. (a) The 3D model of the plate. Multiple recesses were created for the optics, according to their sizes and locations. Next to each recess is a hole for mounting the Thorlabs clamping arm (PM4/M or PM3/M). To avoid creating threads in resin, the 3D printed plate was fastened to an aluminium base board using the counterbores. The clearance holes enable mounting of the entire assembly to any available surface. (b) The real four-sheet optics.

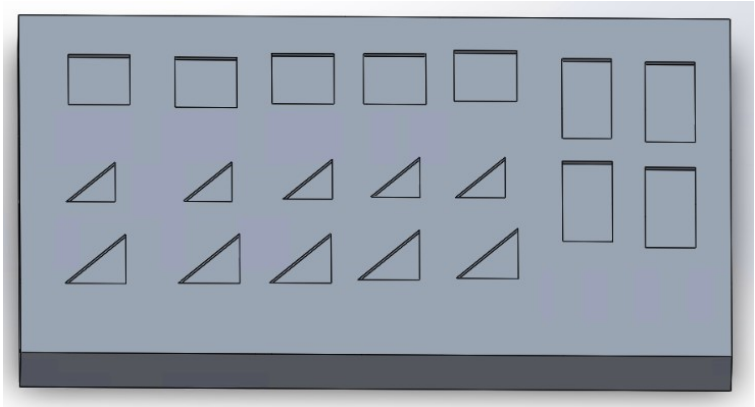

Figure 6.3: Fit test for choosing the right sizes for recesses.

using the counterbores shown in Fig. 6.2. The four M6 clearance holes were included to enable mounting of the entire sheet-splitting assembly, to any available optical table or bread board. Using 3D printing for optics mounting enables a much quicker and relatively easier alignment. It also enables a quick change to other plane separations, by just 3D printing another plate. The compact design allows the optics to be enclosed easily for laser safety purposes, and it is portable to move between optical setups.

The resin plate was printed using a Formlabs printer with $\sim$50 micron precision. Considering the precision of the optics' size, before printing the final mounting plate, a "fit test" was performed. A plate with recesses of different sizes (50 micron step) was printed, in order to find the appropriate sizes for the recesses (Fig. 6.3). The goal of the fit test was to find the sizes of the recesses which "just fit" the optics, limiting the free positioning of the optics in the recesses.

The optics alignment process was similar to Section 3.2. To briefly review, a class 2 laser diode module (mostly called "laser pointer" in this thesis) mounted in a lens tube was used to generate an alignment beam. A Thorlabs ruler card was stuck on top of a Thorlabs magnetic stand, to create an alignment target. The alignment target travelled along the optical axis, to ensure the laser beams were in the right locations

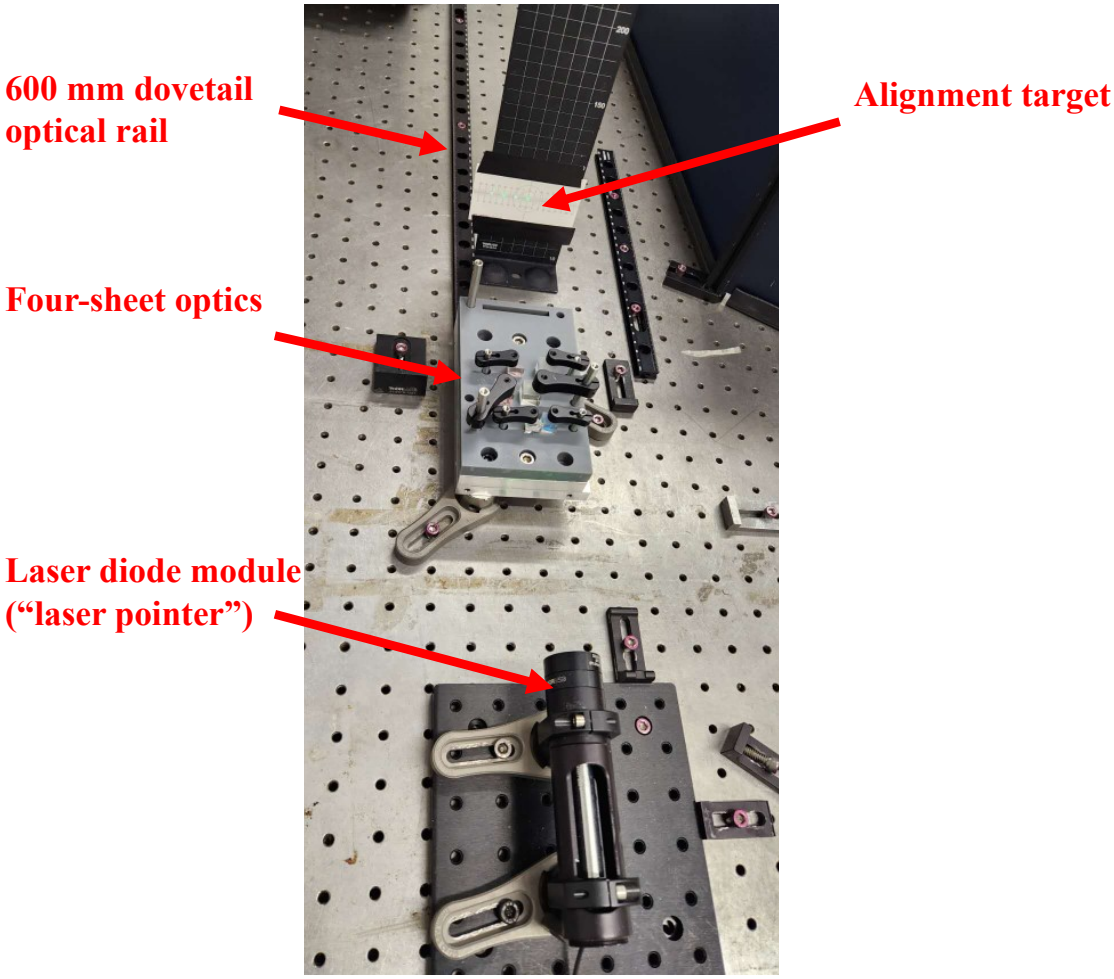

Figure 6.4: The setup for aligning the four-sheet optics.

and were travelling straight. Fig. 6.4 shows the setup for aligning the four-sheet optics. In this procedure, the positioning of the alignment target along the optical axis was achieved by moving the target along a Thorlabs RLA600/M dovetail optical rail. The beam location offsets were all within 0.5 mm (with 600 mm travel along the optical axis).

6.2 Optical Engine Setup

Fig. 6.5 shows the experimental setup in the optical engine. The linear polarised laser

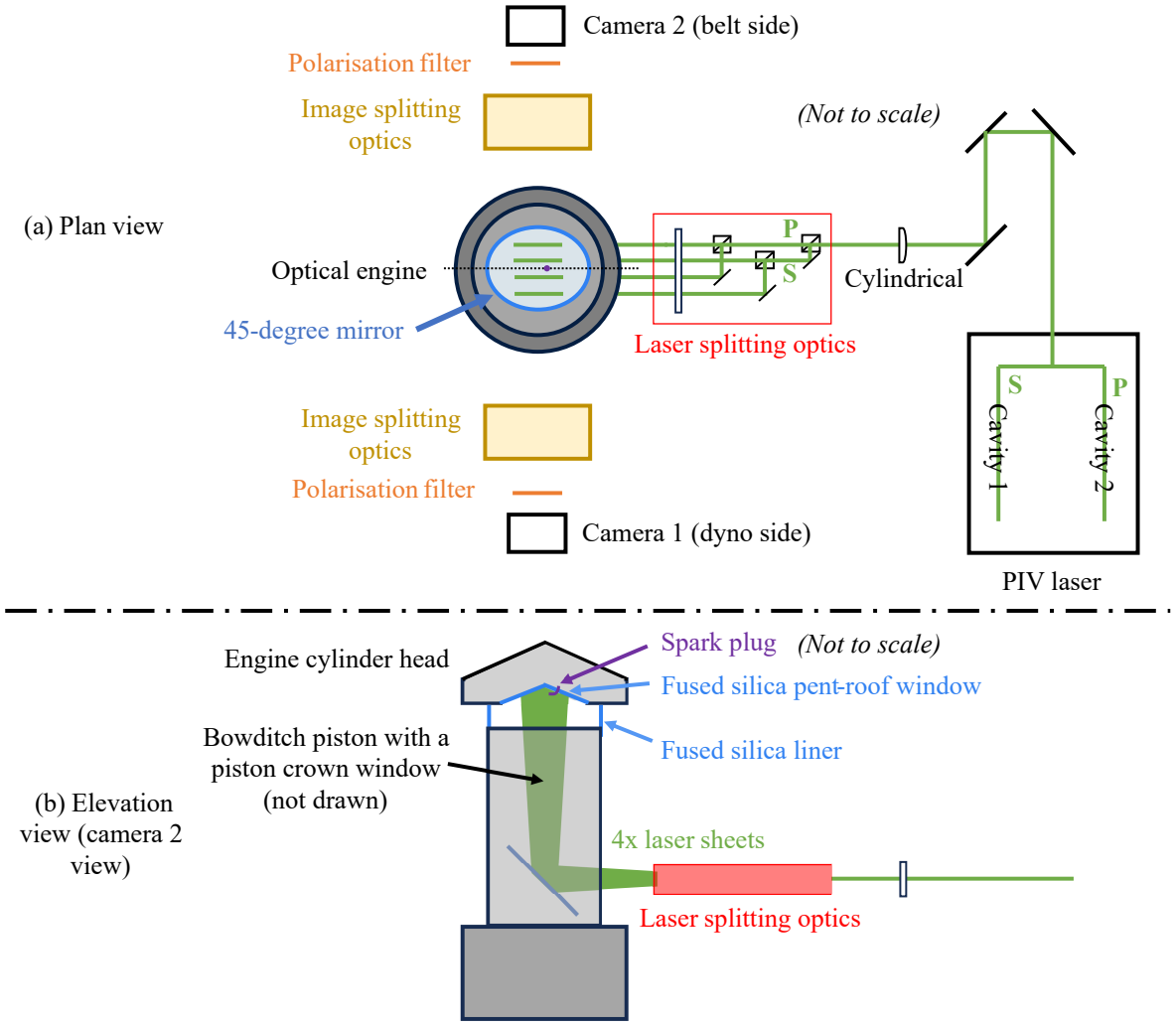

Figure 6.5: Four-plane flame front measurement setup (diagram).

beams from the two cavities of the high-speed Nd:YLF laser (Photonics Industries DM20-527-DH) were separated by the laser splitting device. The cylindrical lens before the PBS and the cylindrical lens after the PBS generate four laser sheets with ∼34 mm width and ∼0.5 mm thickness in the region of interest. The four laser sheets were reflected by the 45-degree mirror beneath the Bowditch piston and went through the piston crown window. The four sheets had a 10 mm separation between each and were symmetrically distributed about the central tumble plane of the engine cylinder. The spark plug is on the central tumble plane, and is slightly offset towards the exhaust valves. The fused silica liner and a pair of fused silica pent-roof windows provided the optical access for the pair of high-speed CMOS cameras (Phantom VEO 710L). Not drawn in the figures, the same dichroic filter (Elliot Scientific CDG-5051) as in Chapter 5 was used to reject the chemiluminescence light from the flame. The real setup in the optical engine is shown in Fig. 6.6.

6.3 Laser alignment and Camera Calibration

As discussed in Chapter 5, the two-step image processing filter is based on matching the pixels on the two sides of the image frame (i.e. the "transmitted" and "reflected" sides) which have the same in-plane world coordinates, and comparing the local COVs and sliding maximum values. To accurately match the pixels, accurate camera calibrations on the four measurement planes were needed. As in the previous chapters, camera calibrations were performed by imaging a dot grid with known dot size and dot spacing, placed on the measurement planes. In this four-plane measurement, the grid had to be positioned to match the locations of the four sheets. The laser alignment and camera calibration strategies were developed based on this requirement.

To mark the target locations of the four sheets, an acrylic "alignment guide" was made, as shown in Fig. 6.7 (a) and (b). The assembly consists of two circular plates, with a 20 mm offset in height by four posts at the margins. The plates and posts were made by laser cutting. The diameter (84.9 mm nominal) of the plate was chosen

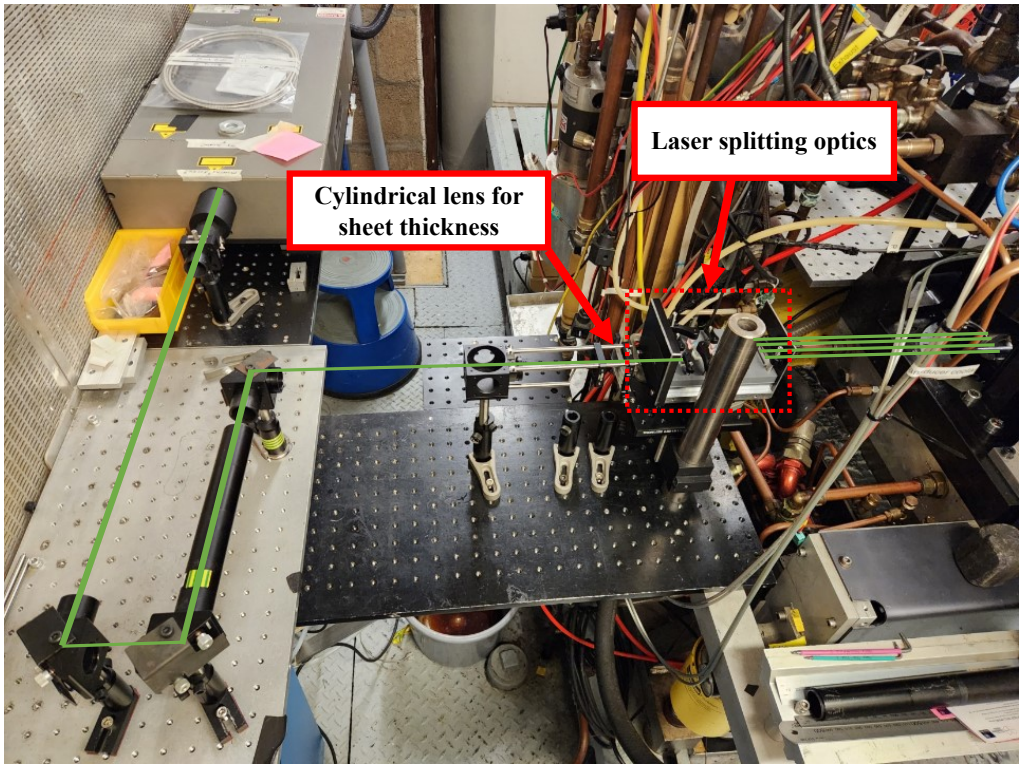

(a)

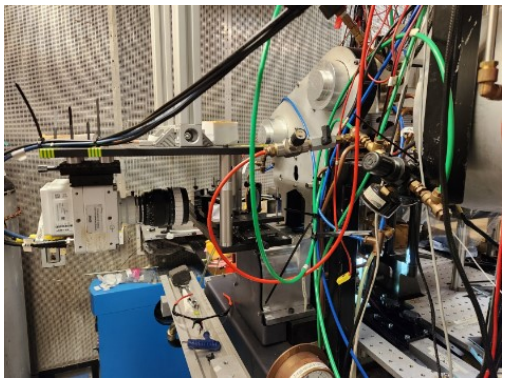

(b)

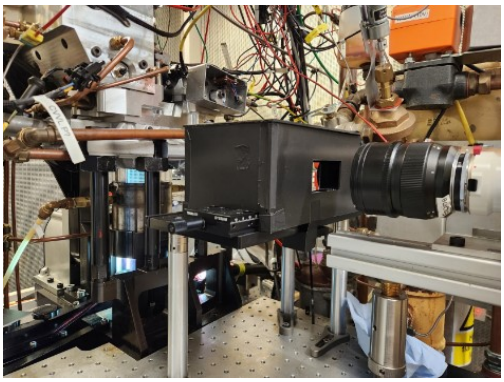

(c)

Figure 6.6: Four-plane flame front measurement setup. (a) The laser setup, with green overlay to indicate beam propagation. (b) Camera 2 and image splitting optics (mounted beneath a breadboard hanging from the ceiling I-beam). (c) Camera 1 and image splitting optics (mounted on an optical surface next to the engine).

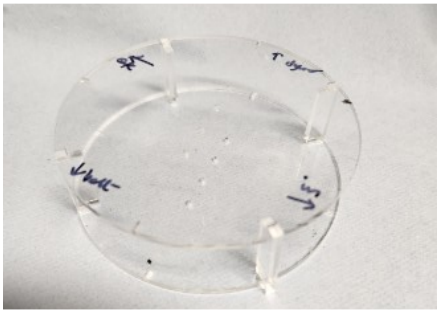

(a)

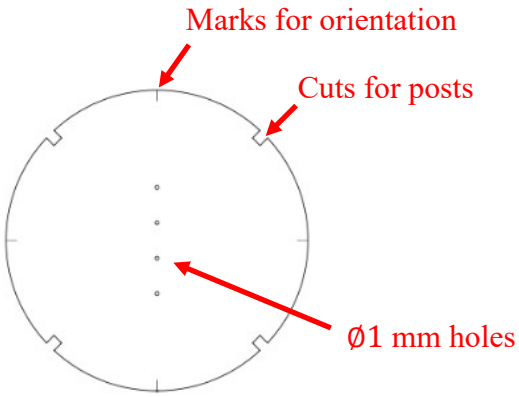

(b)

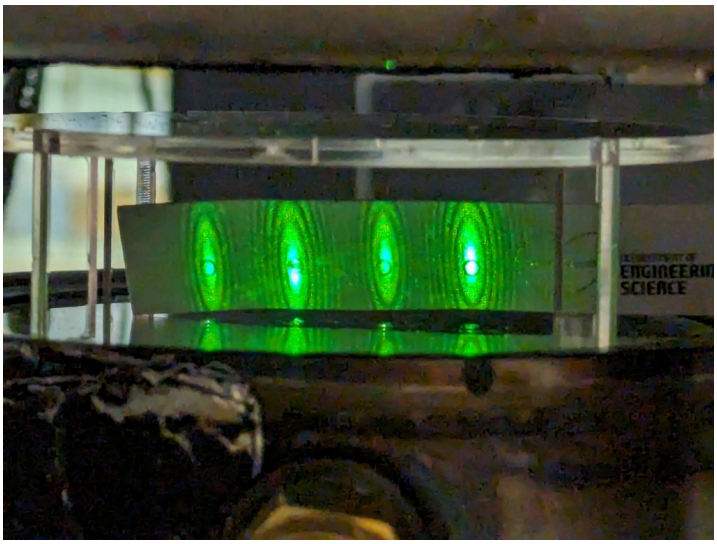

(c)

Figure 6.7: (a) The assembled acrylic alignment guide. (b) Annotated diagram of alignment and orientation features. (c) Diffraction patterns resulting from the four thick sheets travelling through the holes on the lower plate (in this photo, the cylindrical lens controlling sheet thickness was not included yet).

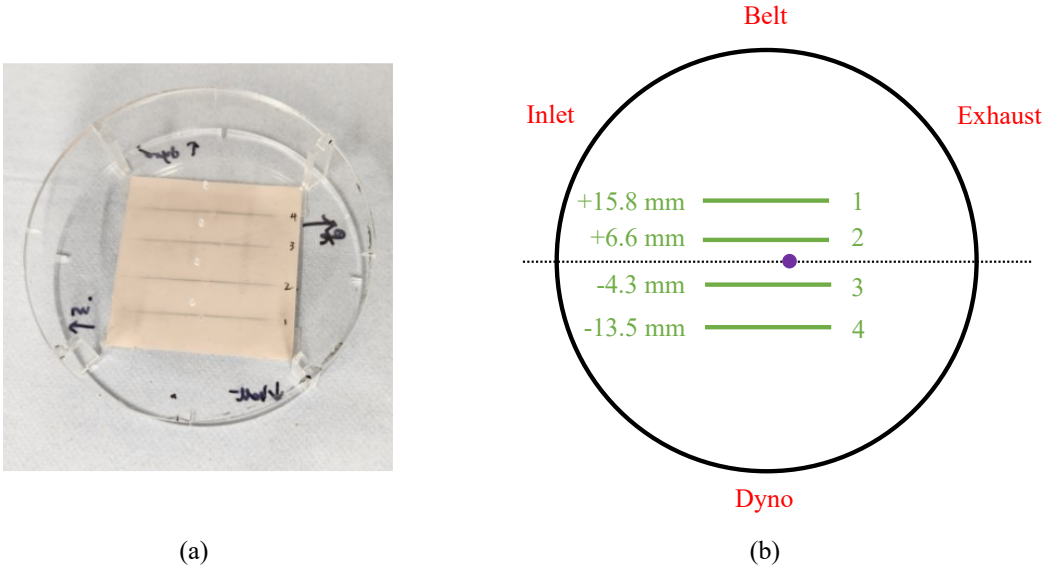

Figure 6.8: (a) Burn paper on the alignment mask. (b) The locations of the four sheets.

so that it fits in the engine cylinder (with an inner diameter of 85 mm nominal) and can be placed on top of the piston. On top of each disk there are four holes with 1 mm diameter, marking the target locations for the four sheet centers. Notches (∼0.2 mm wide, 3 mm long) at the edges were created for marking the orientation of the mask, and were matched with scratches on the barrel during alignment. The aim of the laser alignment was to align the centers of the four sheets to the holes, as close as possible. The two plates provided an estimation on whether the sheets were travelling parallel and vertically in the cylinder, while the 20 mm height offset was limited by the distance between the top of the barrel and the engine firing deck. Fig. 6.7 (c) shows an example image of the alignment process. The four holes could be seen due to the laser illumination.

To mark the actual locations of the four sheets after alignment, the upper plate of the mask was temporarily removed. A piece of burn paper was taped to the lower surface of the upper plate, as shown in Fig. 6.8 (a). Then the upper plate was refitted. Based on the burned marks on the burn paper, a combination of approaches including using a ruler, caliper and imaging the burn paper next to a ruler were used to measure

the locations of the four sheets, as reported in Fig. 6.8 (b).

According to the locations of the sheets, a calibration mask was made. As shown in Fig. 6.9, the calibration mask consists of two parts. (a) is a printed dot grid taped on an acrylic plate. (b) is another circular disc with a diameter of 84.9 mm nominal. Four pairs of rectangle recesses were cut based on the locations of the four laser sheets, so that the printed dot grid could be placed on the four planes accordingly (shown in Figure c). Again, the circular disk was taped on top of the piston window. The height of the dot grid could then be adjusted by the piston height. As shown in Fig. 6.9 (a), a pair of marks ($\sim$0.2 mm wide, 3 mm long) were made on both the printed grid and the acrylic plate. The marks were designed to be aligned with the engine firing deck, providing a reference for the grid height adjustment on the four planes. To judge whether the marks aligned with the firing deck, a thin copper wire (Φ 0.2 mm) was placed between the fused silica liner and the firing deck (gasket). The copper wire was pulled straight, and an image was taken by the camera to check the alignment. The principle and an example image are shown in Fig. 6.10. In sub figure (b), it could be seen that the offset between the copper wire and the marks was sub-pixel (i.e. $<$0.15 mm). In Fig. 6.10 (b), it is also noticed that a "shadow" region is visible between the pent-roof window and the liner. This region is caused by the gasket between the liner and the firing deck. In the subsequent data analysis sections, this region is not used.

A brief comment on the accuracy of the measured four-sheet locations in Fig. 6.8 (b): The four pairs of rectangle recesses in Fig. 6.9 (b) and (c) were created based on the measured four-sheet locations. In camera alignment, the focus of the camera lenses was adjusted to achieve the best focus on the calibration grid on the four planes defined by the recesses. After camera alignment, it was found that the quality of the in-focus particle images was good (i.e. the in-focus particles had a diameter of 2 to 3 pixels). The camera lens focus was not tuned after camera alignment.

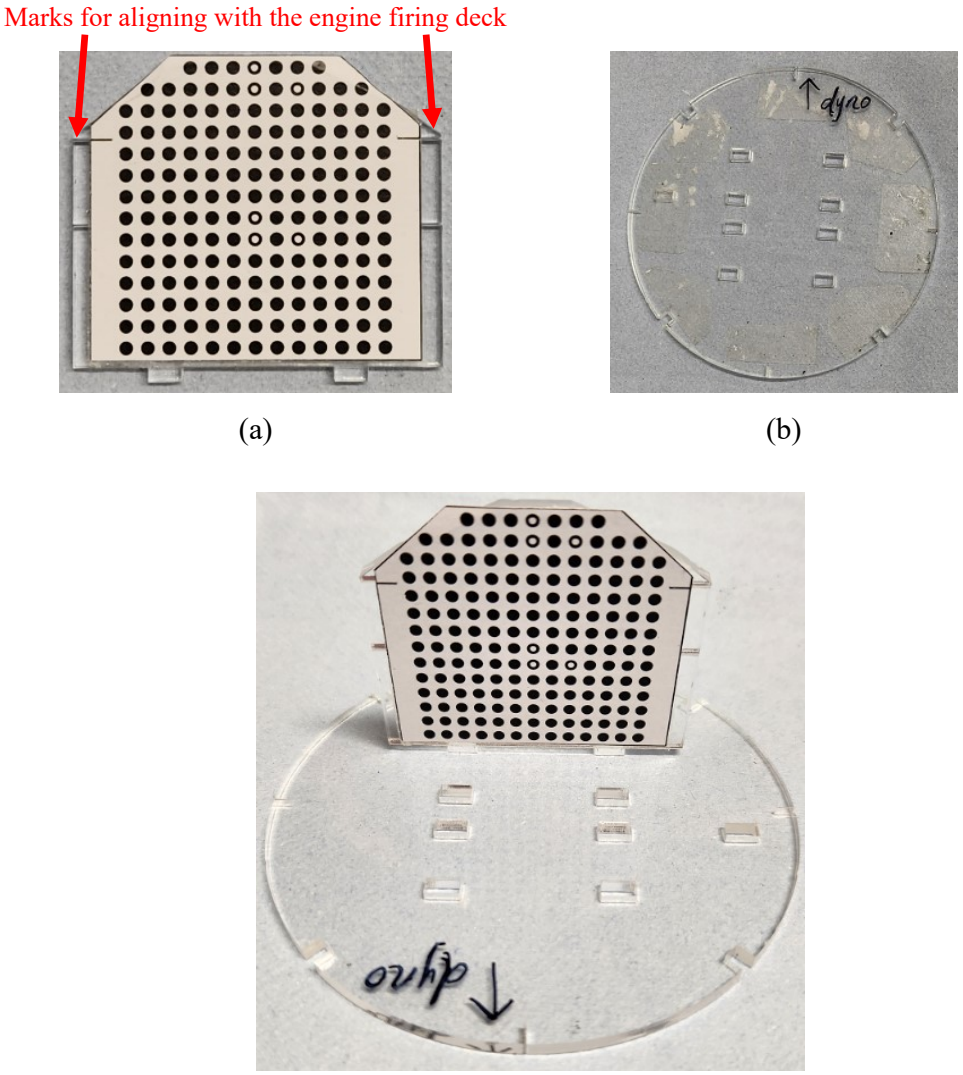

Figure 6.9: The calibration mask for four-plane calibration. (a) The calibration grid taped on an acrylic plate. A pair or marks (∼0.2 mm wide, 3 mm long) were made on both the grid and the plate. The marks were designed to be aligned with the engine firing deck, as a reference of the height of the grid in the cylinder. (b) A circular disc with four pairs of rectangle recesses, cut based on the measured locations of the four sheets. The calibration grid on the plate was placed on the four planes defined by the recesses. (c) The assembly of (a) and (b), on one of the four plane locations

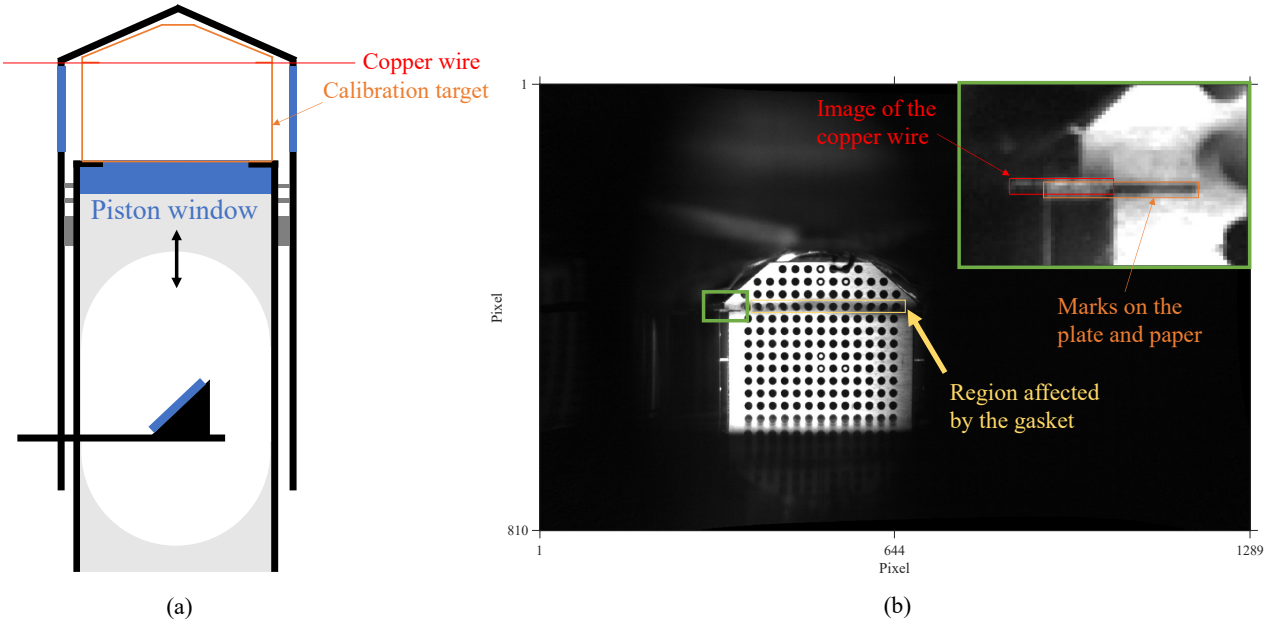

Figure 6.10: Calibration grid height adjustment based on pulling straight a thin copper wire (Φ 0.2 mm) between firing deck and fused silica liner.

6.4 Polarisation Change

In principle, the laser splitting optics and cameras with polarisation filters enable simultaneous four-plane imaging based on defocusing separation and polarisation separation. To find the correct orientation of the polarisation filter of each camera, the following procedure was followed. First, only planes 1 and 3 (see Fig. 6.1 for the numbering of the sheets and cameras) were illuminated, then the polarisation filter orientation of camera 2 was adjusted until the light signal received by camera 2 was minimised, because camera 2 was set up to measure planes 2 and 4. Second, only planes 2 and 4 were illuminated, then the polarisation filter orientation of camera 1 was adjusted until the light signal received by camera 1 was minimised. A ∼22.5 degree-step was used for the filter orientation testing. Fig. 6.11 shows the best attempts of polarisation separation. The crosstalk between polarisations was visualised by illuminating with each laser cavity independently. When sheets 1 and 3 were illuminated, camera 1 could see most particle images. However, there are several regions where the particle images appeared darker (indicated by the blue arrows). Those regions become brighter in

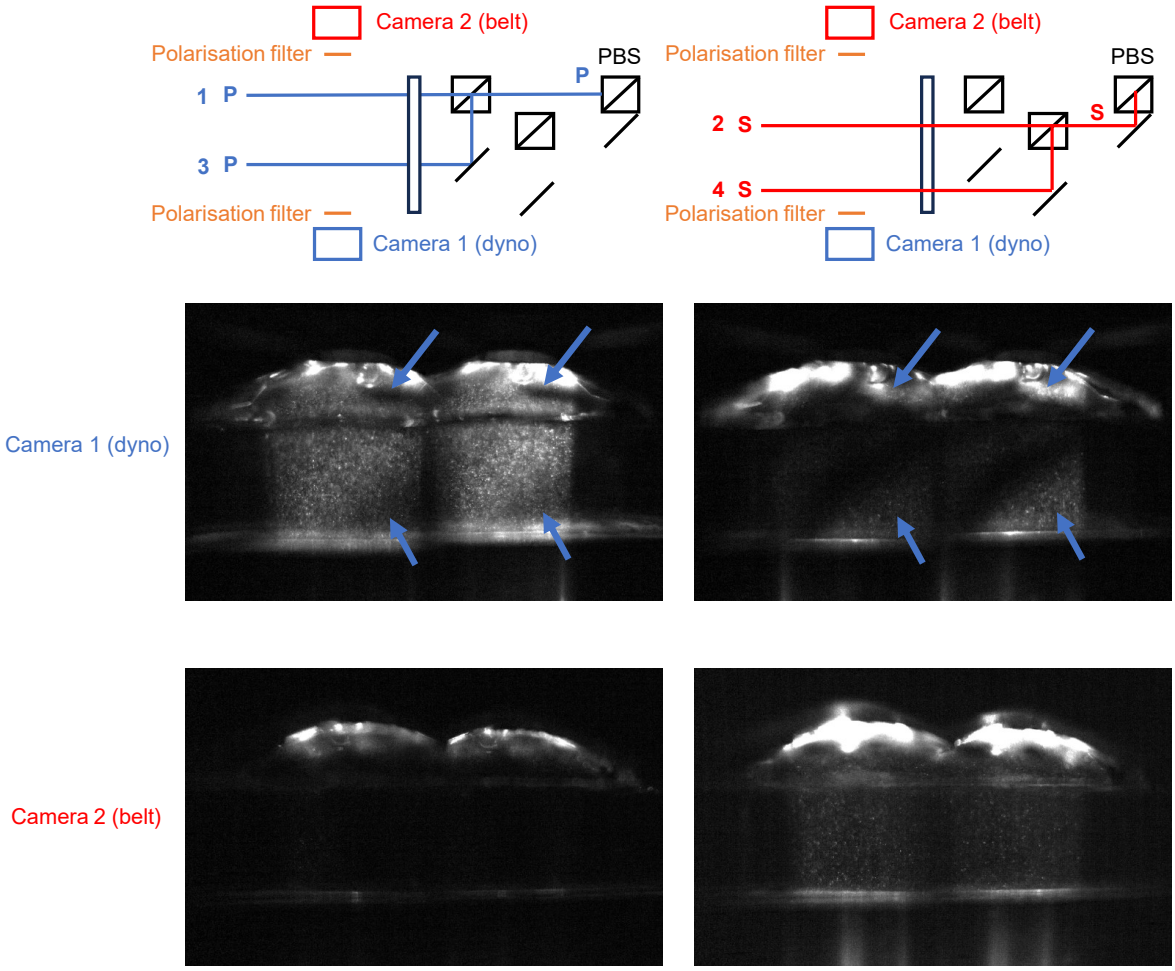

Figure 6.11: Polarisation separation performance, evaluated by illuminating with each laser cavity separately. All the images use the same colourbar scale (not shown). The imaging splitting optics are not drawn. Note how the parts of the images that are dark under sheet 1 & 3 illumination became bright under sheet 2 & 4 illumination, indicated by the blue arrows.

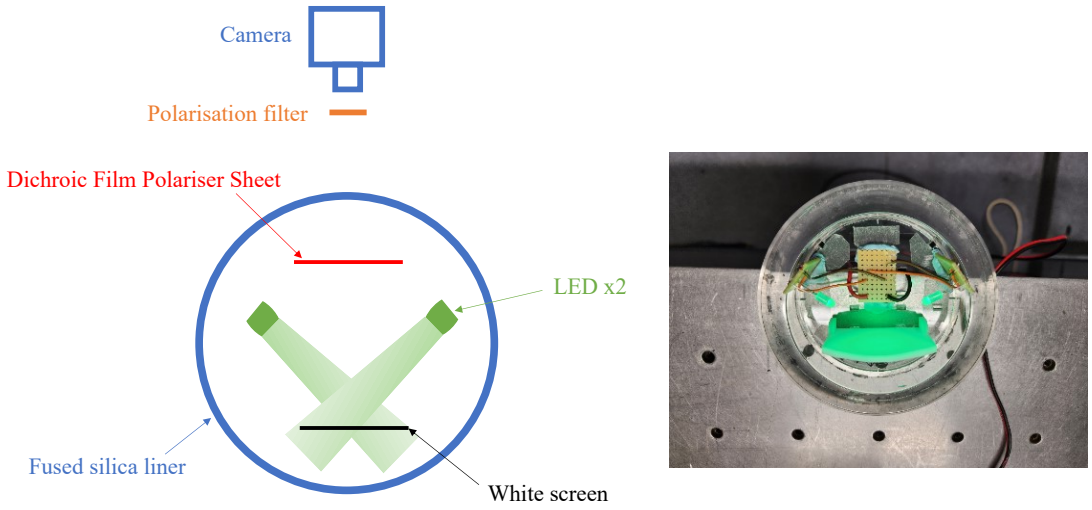

Figure 6.12: The illumination rig for testing the effect of liner sealing pressure on light polarisation.

the images taken when sheets 2 and 4 were illuminated, suggesting a corresponding pattern. The polarisation separation for camera 2 performed better. However, the overall intensities of the camera 2 images are lower, which could be visually observed in Fig. 6.11 where the same colourbar scale is used for all the images. (As will be shown later, the camera 2 images are still darker, even when temporal separation is used and no polarisation filter is involved.) Based on the spatial-dependence characteristic of the camera 1 images, it is inferred that the polarisation state of the scattered light has been modified by the stress-induced birefringence of fused silica under the 20 bar lab jack pressure holding the liner in place. To demonstrate the effect of pressure on the polarisation state, an illumination rig was built inside the engine chamber and images was taken with different sealing pressures. Fig. 6.12 shows the illumination rig. It was built on the circular disc (Fig. 6.9 (b)) for camera calibration. A 3D printed white plate screen was positioned on one of the four pairs of recesses, as an illumination screen. Two green LEDs (532 nm) illuminated the screen from the sides. A dichroic polariser film (Thorlabs LPVISE2X2) was positioned between the white screen and the camera, to linearly polarise the light through the fused silica liner and pent-roof window. A polarisation filter was put on the camera lens, to analyse the polarisation state of the

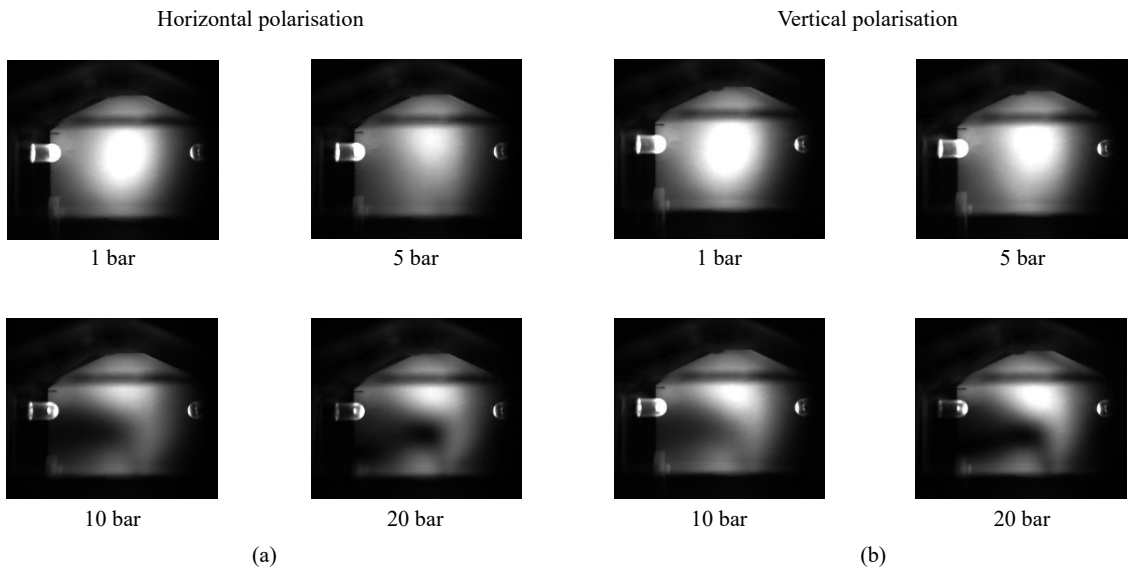

Figure 6.13: Images of the illumination rig in the engine chamber, under different liner sealing pressures. (a) The dichroic polariser film and the camera lens polarisation filter allow horizontal polarisation through. (b) The dichroic polariser film and the camera lens polarisation filter allow vertical polarisation through. Horizontal and vertical polarisations are defined from the perspecrive of the camera. All images in this figure use the same colourbar scale (not drawn).

light. Some images from the camera are shown in Fig. 6.13, which clearly show how the LED images change with different sealing pressures. In future, more study is warranted to systematically investigate the pressure effect (such as, whether it is affected by the fused silica liner manufacture/design, the lab jack system loading uniformity and so on). On the other hand, the failure of polarisation discrimination in this test further highlights the importance of the defocusing method. At least in this engine, the defocusing method and the wavelength method are the only two approaches for extending standard PIV system to perform simultaneous multi-plane measurements.

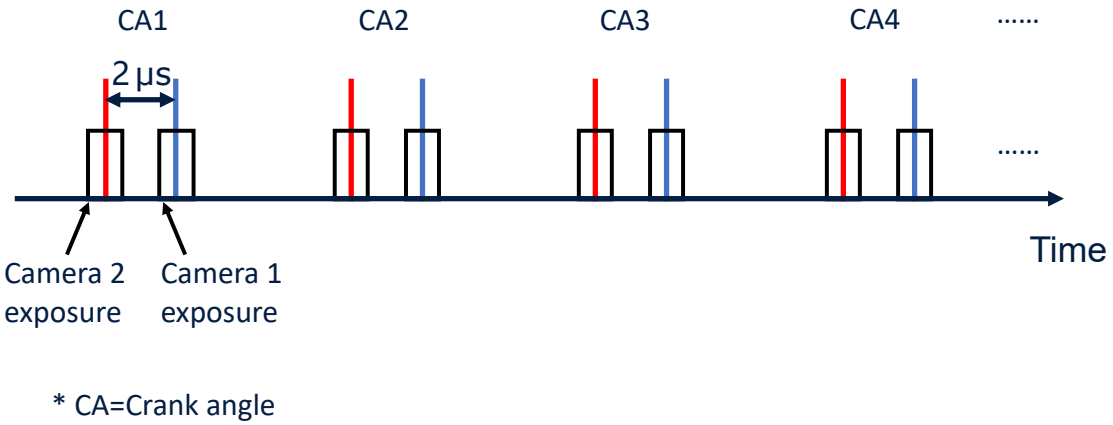

Figure 6.14: Timing diagram of the temporal separation. Each cavity is indicated by a different colour. The black rectangles represent camera exposures.

6.5 Four-plane Flame Front Tracking

Because polarisation discrimination was not reliable in this work, a combination of defocusing and temporal separation was used, to achieve a simultaneous two-plane measurement (defocusing) and a quasi-simultaneous four-plane measurement (temporal, 2 μs between laser cavities). The 2 μs separation was limited by the minimum exposure duration of the cameras (1 μs), for reliably avoiding crosstalk. The timing diagram describing the temporal separation is shown in Fig. 6.14. Measurements were made every 2 CADs. As the polarisation separation was replaced by temporal separation, the polarisation filters of the cameras were removed, to make the best use of the light scattered from seeding particles.

The engine test condition is described in Table 6.2. At this working condition, it was found that in most cycles, all particles were consumed by flames in the pent-roof window region, so the liner region was always dark and therefore not used for data analysis. By using the same image processing scheme in Chapter 5, Fig. 6.15 and Fig. 6.16 show an example of four-plane flame front tracking, at the same CAD of the

Table 6.2: Engine test condition for the four-plane flame front measurement.

Engine speed	1000 rpm
Intake air temperature	318 K
Intake air volume flow rate	1.00 L / s
Fuel	iso-octane (stoichiometric)
Fuel injection timing	280 CAD bTDC
Spark ignition timing	10 CAD bTDC

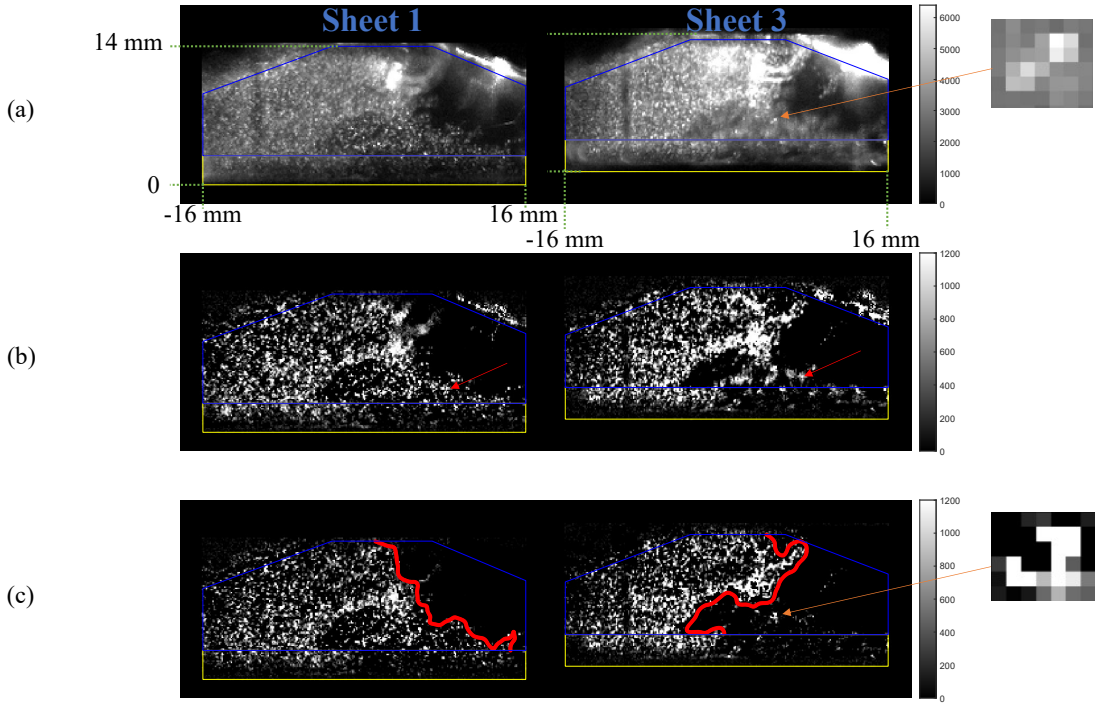

Figure 6.15: Four-plane flame front tracking example, camera 1. (a) Raw image (after distortion correction). (b) Background subtracted image. (c) Image after two-step filtering. The regions indicated by the yellow boxes are affected by the gasket (see Fig. 6.10 (b)), and not used in the data analysis. The blue boxes indicate the regions of interest. The zero height is the height of the firing deck. 0 mm on the horizontal axis aligns with the central axis of the cylinder.

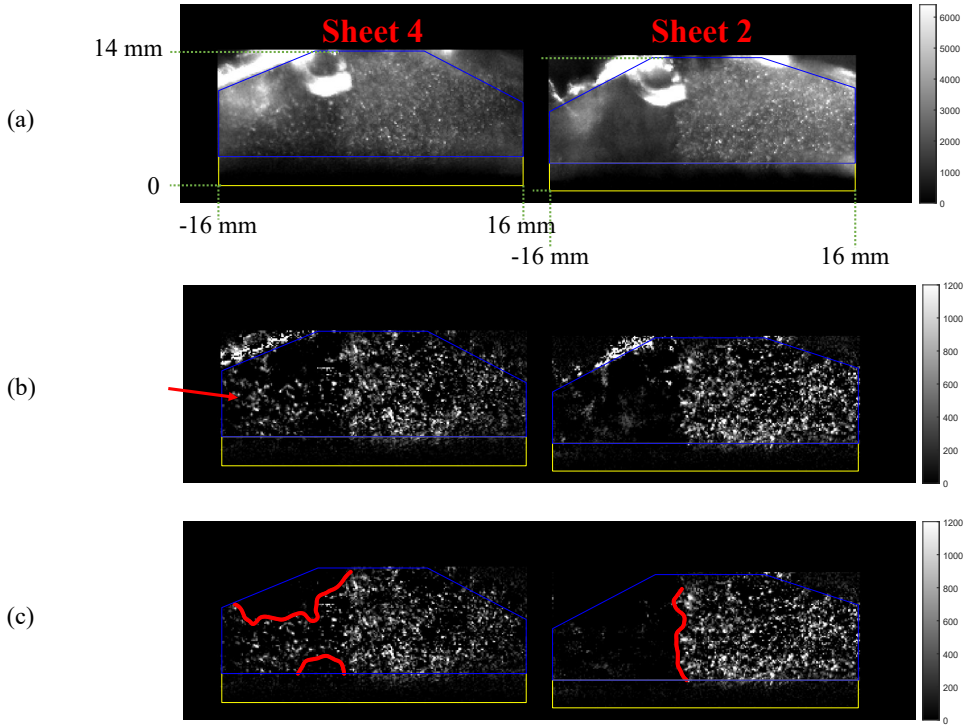

Figure 6.16: Four-plane flame front tracking example, camera 2. (a) Raw image (after distortion correction). (b) Background subtracted image. (c) Image after two-step filtering. The regions indicated by the yellow boxes are affected by the gasket (see Fig. 6.10 (b)), and not used in the data analysis. The blue boxes indicate the regions of interest. The zero height is the height of the firing deck. 0 mm on the horizontal axis aligns with the central axis of the cylinder.

same cycle. From the raw images, it could be noticed that the background scatter from the spark plug and the edges of the pent-roof window is bright. Some of these bright areas persist after background subtraction. In the next section, where four-plane burn rates are evaluated, the effect of the background scatter will be further discussed. The blue boxes in the figures indicate the regions of interest used on the four planes. They were determined to be as large as possible while avoiding the influence of the bright background scatter as much as possible. The yellow boxes indicate the regions affected by the gasket between the firing deck and the fused silica liner (see Fig. 6.10 (b)). Those regions were not used in data analysis. In Fig. 6.15, it could be seen that there is a vertical black stripe on the left of the field of view. By visually checking the piston window, it appears that the stripe is caused by a small area of damage on the piston window, roughly aligned with sheet 3. The stripe causes the affected region to become darker, but particles could still be seen. Therefore, the affected region was kept for data analysis. In Fig. 6.15 (b), a pair of red arrows are used to highlight in-focus particle images on sheet 1 and their corresponding out-of-focus images on sheet 3. In Fig. 6.15 (c), it could be seen that the out-of-focus images are effectively removed. The bright residual highlighted by the orange arrow could be traced back to the raw image, in which the residual looks like sharp particles and could be an "unburned island". Because human eyes could not confirm whether such an "island" is a physically unburned region or noise, in future, numerical tests would be valuable to further investigate the performance of the defocusing technique on distinguishing small "burned pockets" or small "unburned islands".

Another important characteristic of the data is that, the background subtracted image in Fig. 6.16 (camera 2) looks darker than the background subtracted image in Fig. 6.15 (camera 1). In fact, in this test, the pulse energy ($\sim$ 12 mJ) of the laser cavity used by camera 2 was about double the pulse energy ($\sim$ 6 mJ) of the laser cavity used by camera 1. However, the particle images of camera 2 still look darker. Limited by the laser, the power difference of the two cavities could not be further increased at the current repetition rate. Although the seeding density is the same in

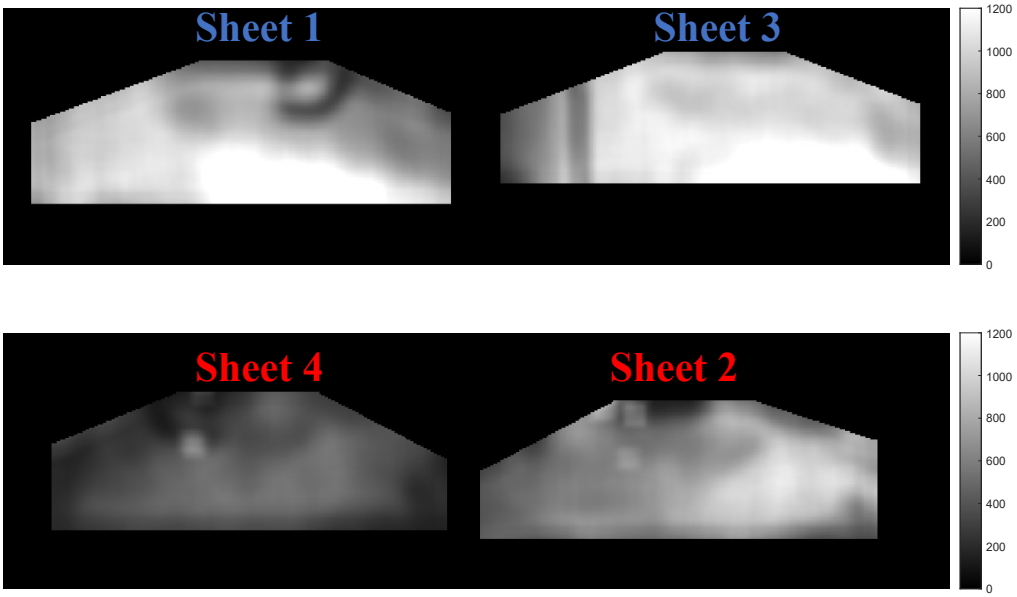

Figure 6.17: The sliding average intensities of 300 images of the two cameras before ignition. First row: camera 1. Second row: camera 2.

the engine chamber, the darker images on camera 2 lead to the particles appearing sparser and darker on camera 2 (highlighted by the red arrow in Fig. 6.16 (b)), making the data processing less robust to out-of-focus noise and background noise. To show the intensity difference of the two cameras, the sliding average intensities of 300 images from the two cameras before ignition were averaged, as shown in Fig. 6.17. It is apparent that images from camera 2 are darker overall, and data from sheet 4 darker still. It is thought that the camera 2 images being darker could be due to a polarisation effect, but this needs to be confirmed by future tests. In future, it is expected that the intensity difference between the two cameras could be minimised by placing a half-wave plate after the first prism mirror (the one next to the polarising beamsplitter) in the laser splitting setup. In terms of Sheet 4 images being darker than sheet 2 images, it could be related to the image splitting optics' alignment, but also warrants future investigation.

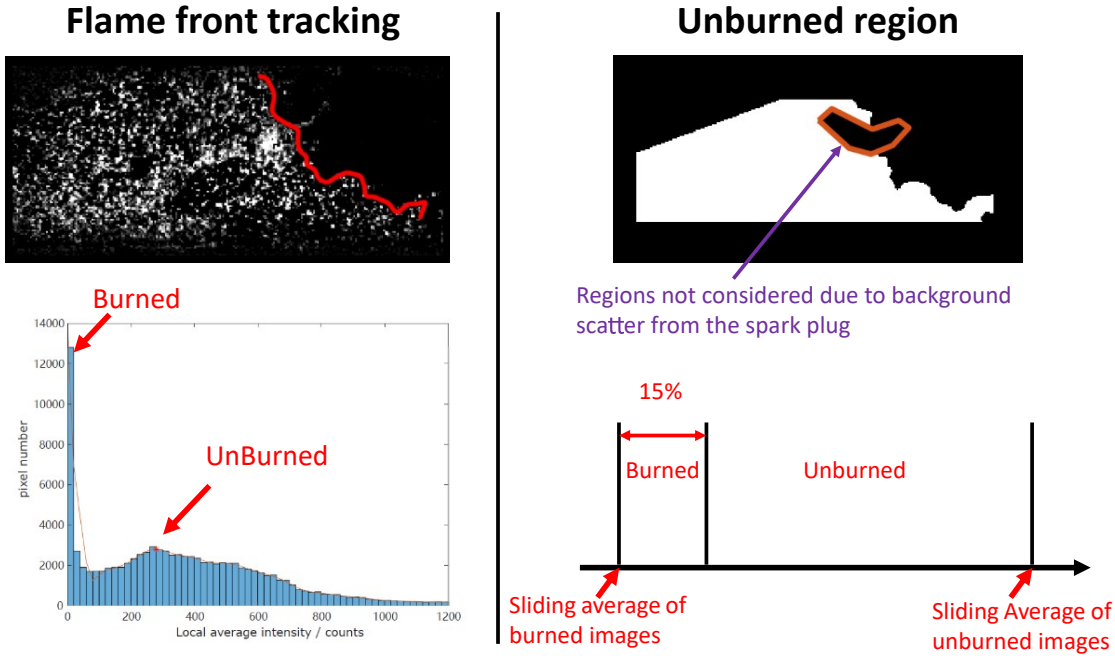

Figure 6.18: A demonstration of two approaches for "burned region vs. unburned region" evaluation.

6.6 Four-plane Burn Rate Evaluation

This section explores the potential to use the four-plane combustion images for evaluating the local burn rates on the four planes, versus the overall burn rate calculated using the Rassweiler and Withrow method, which is a typical method for calculating the overall Mass Fraction Burned (MFB) in engine cylinders from an in-cylinder pressure trace. The combustion images from 100 cycles between 18 CAD before TDC to 30 CAD after TDC are analysed (the ignition timing was 10 CAD before TDC). The same two-step filtering scheme was performed on all images. In this section, a different approach to distinguish "burned region vs. unburned region" was applied. As illustrated in Fig. 6.18 (left hand side), a histogram method has been used so far for flame front tracking (details can be found in Chapter 5). In principle, the histogram method takes advantage of the "difference" between the bright (unburned) and the dark (burned) regions. This method works well in the middle stage of combustion, where a sharp boundary exists between unburned and burned regions. However, it is not reliable at the late CADs, where most or all particles are consumed, and the

"difference" between burned pixels and background noise can be misleading. More discussions on the background scatter effect will be given later in the result analysis. In this section, an approach based on evaluating the sliding average intensities of pixels was used. For each plane separately, 300 images before ignition were used to calculate the mean sliding average intensities (i.e. the images shown in Fig. 6.17), which were used for marking the average intensities in unburned images. 100 images at the last CAD (30 CAD after TDC) of the measurement were used to calculate the average sliding average intensities for burned cases. The 100 images were visually checked, to confirm that particles were all consumed. A threshold (15%) between the "burned intensity" and the "unburned intensity" was set. When evaluating individual pixels in the regions of interest, any pixel with a sliding average intensity larger than the threshold was considered unburned. The ratio of the (number of burned pixels) to the (total number of pixels in the field of view), is defined as the Planar Fraction Burned (PFB).

The MFB was calculated by using the "CoBRA" code maintained by the Oxford Thermal Propulsion Research Group. It is based on the Rassweiler and Withrow method [82], which employs the observation that in a constant volume combustion bomb, the fraction of the mixture mass that has burned is proportional to the fractional pressure rise in the bomb. In the Rassweiler and Withrow method, the pressure rise measured by the in-cylinder transducer is considered to consist of two components, one due to combustion, Δp_c, and one due to volume change, Δp_v:

$$\Delta p = \Delta p_c + \Delta p_v. \tag{6.1}$$

Assuming that the pressure change due to volume change can be calculated based on a polytropic process:

$$p_{i+1} - p_i = \Delta p_c + p_i \left[(\frac{V_i}{V_{i+1}})^{\gamma} - 1 \right], \tag{6.2}$$

which can be reorganised into:

$$\Delta p_c = p_{i+1} - p_i \left(\frac{V_i}{V_{i+1}}\right)^{\gamma}. \tag{6.3}$$

Different from a combustion bomb, the combustion in an engine occurs at different volumes. Therefore, Δp_c needs to be normalised by a reference volume, before it could be related to the MFB. In this work, the reference volume was chosen to be the volume at TDC, V_{TDC}:

$$\Delta p_c^{\star} = \Delta p_c \frac{V_i}{V_{TDC}}. \tag{6.4}$$

By identifying the start and end of combustion, and the number of crank angle degrees N between them, the MFB can be calculated:

$$\text{MFB} = \frac{\sum_0^i \Delta p_c^{\star}}{\sum_0^N \Delta p_c^{\star}}. \tag{6.5}$$

In this work, the start of combustion was specified to be the ignition timing, and the end of combustion was chosen to be one CAD after the exhaust valve opening.

For convenience of locating the four sheets, a layout diagram is shown in Fig. 6.19. Fig. 6.20 shows the comparison between the overall MFB curve and the local PFB curves of the four planes, averaged over 100 cycles. In the plots, 360 CAD indicates top dead centre. The ignition timing is 350 CAD (10 CAD bTDC), indicated by the dotted line. Several observations could be made from the plots. First, the optical method is able to measure the early-stage combustion on each plane, when the overall MFB curve hardly detects any combustion (for example, at 360 CAD). In the early stages of combustion, the overall MFB calculated based on the pressure trace is not reliable. This could be due to signal noise when the pressure rise is low, or because the model does not consider the heat transfer effect by the ignition. Considering Fig. 6.20 (a), there is no obvious difference between the PFB curve of sheets 1 & 2 averaged together and the PFB curve of sheets 3 & 4 averaged together, suggesting that the early flame in this engine does not have a preferred growth direction at this test condition.

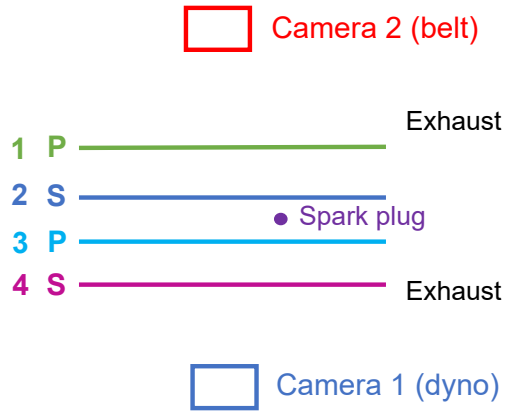

Figure 6.19: A diagram of the four sheet locations. The image splitting optics are not drawn.

Considering Fig. 6.20 (b) and (c), the air-fuel mixtures on the sheets (2 and 3) closer to the spark plug burn sooner than the mixtures on the sheets (1 and 4) further from the spark plug, on average. This observation is not against intuition. At the end of combustion on the four sheets, there are unnatural turning points on the curves. These are caused by the relatively bright and changing background scatter, as introduced earlier. An example is shown in Fig. 6.21, which shows an image from camera 2, very late in the cycle (388 CAD). By eye, it could be confirmed that all particles were consumed. But some of the background scatter could not be perfectly removed, leading the data processing code to believe there were unburned pixels. Referring back to Fig. 6.20 and comparing the error bars on the curves, it can be seen that sheet 4 suffered most from the background scatter, as the error bars of the late CADs (from 382 to 390 CADs) on the sheet 4 curve are larger than those of the other sheets. This aligns with the discussion on Fig. 6.17 where the images of camera 2 are darker compared to camera 1, and the data on sheet 4 are also darker than sheet 2. Note also that before ignition, the optical method reports average PFBs lower than 0.5% for sheets 1, 2 and 3, and about 2% for sheet 4. Ideally, the reported PFBs should be zero.

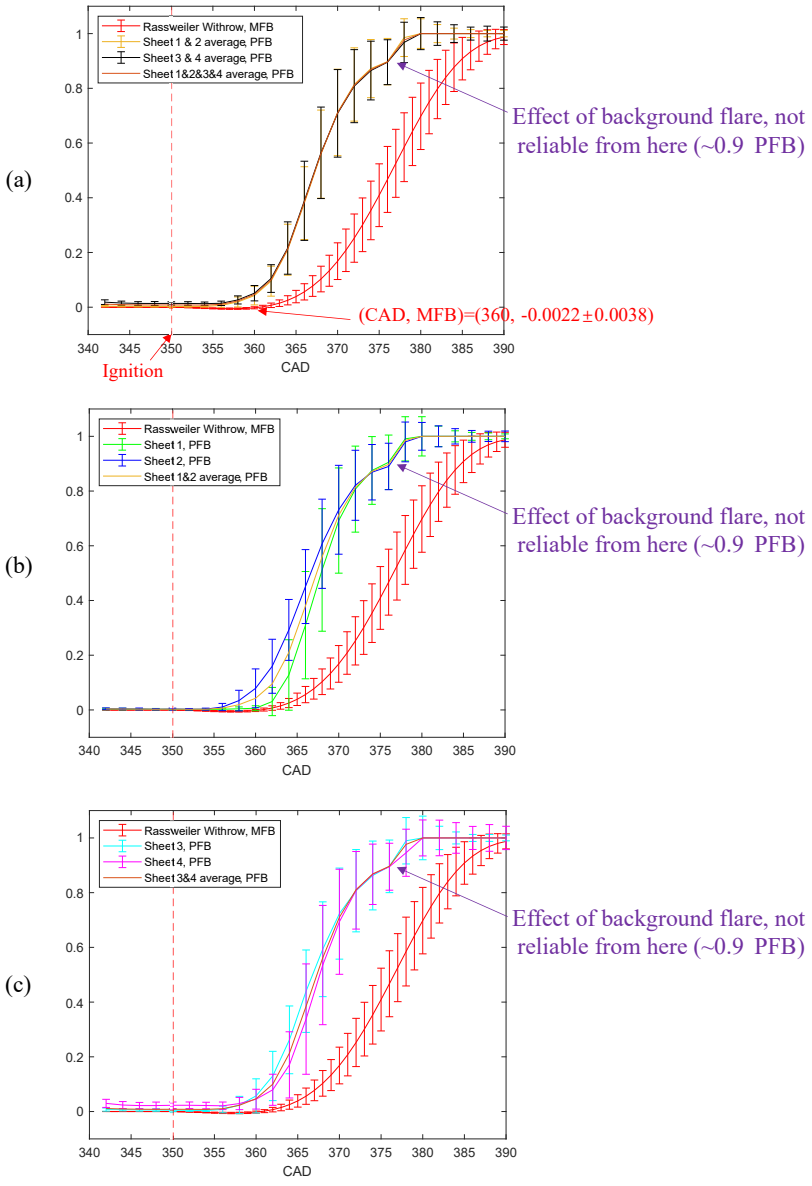

Figure 6.20: Average MFB and PFB curves of 100 cycles.

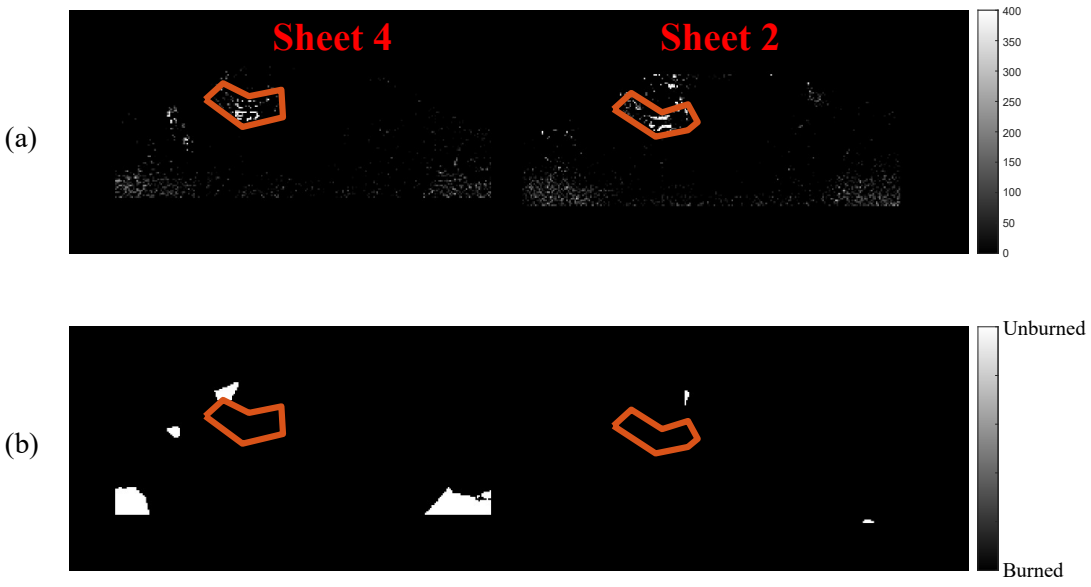

Figure 6.21: An example showing the impact of the varying background scatter. This example is at 388 CAD (28 CAD aTDC), in which human eyes could confirm all particles were burned, but the data processing code believed that some pixels were unburned. (a) Background subtracted image. (b) Burned vs. unburned map. The regions enclosed by the orange polygons, chosen based on the scattered light from the spark plug, were not considered for burned fraction evaluation.

The discrepancy is caused by the two-step filter occasionally being too aggressive, and some inaccuracy in the "burned region vs. unburned region" evaluation approach as described in Fig. 6.18. Again, this observation aligns with the discussion that sheet 4 was the most unreliable plane in this test. In future, polarisation effects should be further investigated. In particular, the darker images seen by camera 2 could be potentially resolved by adding a half-wave plate after the first prism mirror next to the polarising beamsplitter. Other approaches for "burned region vs. unburned region" evaluation are also worth exploring in future work.

It is known that the overall burn duration (calculated from MFB) is one of the indices for evaluating the CCV of engine behaviour. With the four-plane imaging approach, this work introduces the "local CCV of combustion", based on the PFBs on the four planes. The overall burn duration is defined as the number of CAD between 0.1 to 0.9 MFB, equivalently the planar burn duration is defined as the number of CAD between 0.1 to 0.9 PFB. Fig. 6.22 compares the planar burn durations on the four sheets and the overall burn duration in the chamber, across 100 cycles. In Fig. 6.22, the numbers in the dots indicate the numbers of cycles they represent. (Those dots without numbers represent only one cycle.) The direct observation from the plots is that a strong correlation between local burn duration and overall burn duration is not found. The red dotted lines denote equivalent fractional burn duration. Dots appearing above the lines mean that in those cycles, it took longer to burn 10%-90% of the mixtures on the planes, than 10%-90% of the mixtures in the entire combustion chamber. To a certain extent, the range of the overall burn duration on the x axis indicates the overall CCV of engine performance, and the range of the planar burn duration on the y axis represents the local CCV of combustion. From all the plots in Fig. 6.22, no strong correlations could be found between the two. For example, on sheet 1, when the overall burn duration is 15 CADs, the local burn duration ranges from 4 to 18 CADs.

To examine the locally "slow-burning" phenomena more closely, the MFB and PFB curves of a representative cycle (indicated by the red arrows in Fig. 6.22) are plotted,

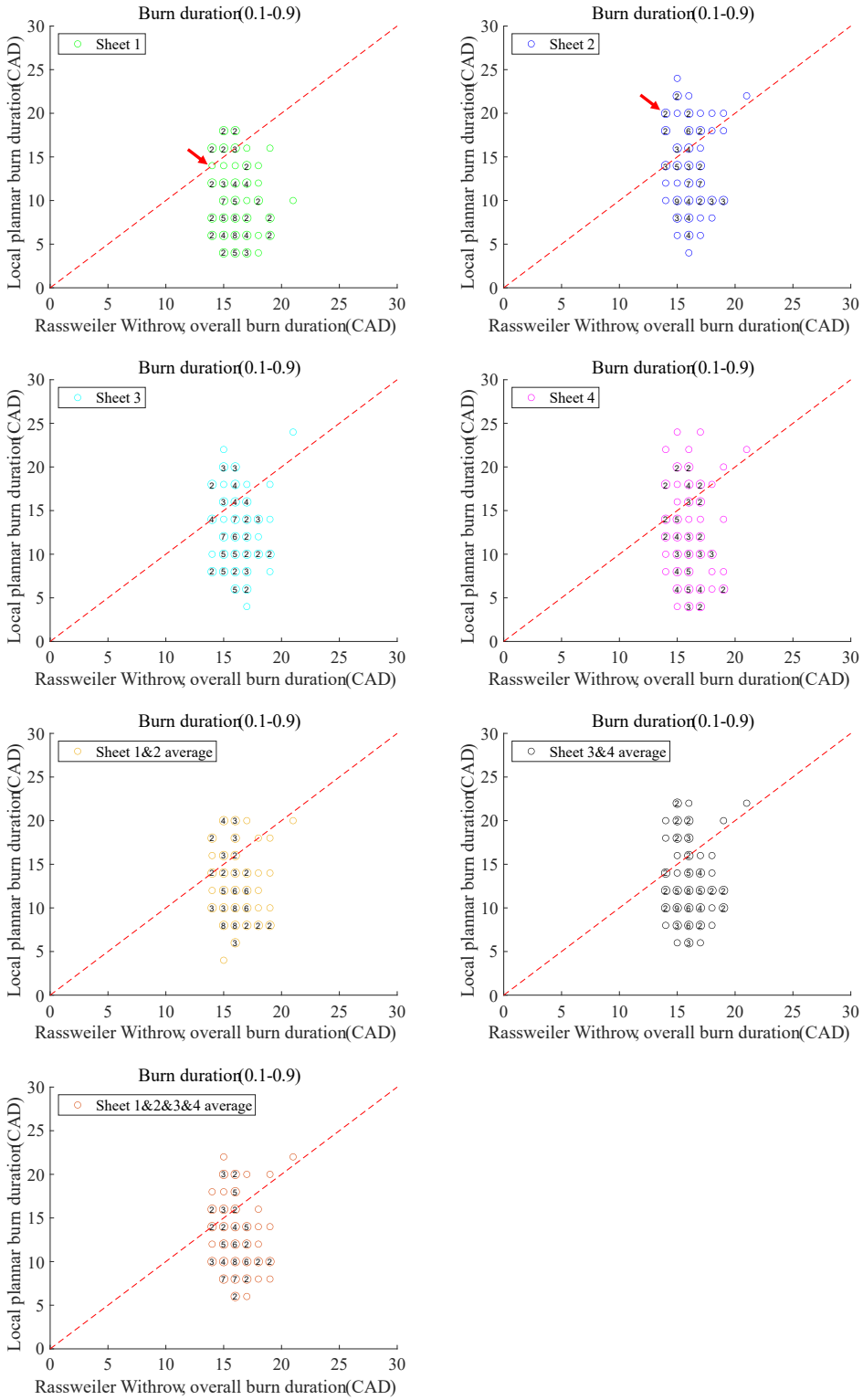

Figure 6.22: Comparison between local burn durations on the four sheets, and overall burn duration in the chamber.

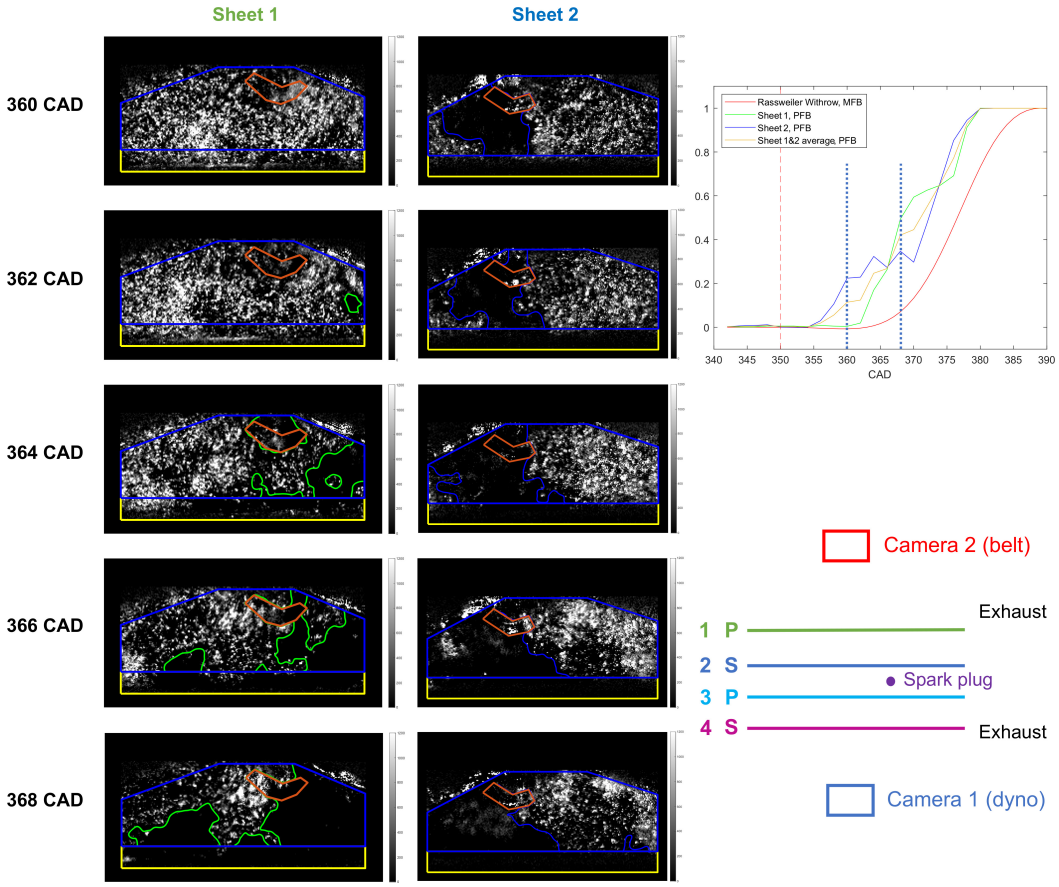

Figure 6.23: A representative cycle with locally "slow-burned" planes, corresponding to the highlighted cycle in Fig. 6.22. The PFB curves of sheet 1 and 2 are plotted. The combustion images (background subtracted images) from 360 CAD to 368 CAD are shown. It is noticed that sheet 2 experienced a "frozen" period in which the flame stops expanding.

and the relevant particle images are shown in Fig. 6.23. It can be seen that from 360 CAD to 368 CAD, the flame on sheet 2 does not expand (appearing "frozen"). On the other hand, the flame on sheet 1, which is the plane further away from the spark plug, grows and rapidly consumes a larger in-plane region than the flame on sheet 2. In this cycle, the flame first burned a substantial part on sheet 2 (indicating a fast early flame growth up to top dead centre), and then stops expanding for some time. Conversely, the flame starts expanding on sheet 1 after top dead centre, with a relatively high rate throughout. Such a phenomenon might be related to an interaction between swirl flow motion and the early flame growth.

In combustion engine study, an assumption that is widely accepted is that a cycle which burns fast in the early stages burns fast overall. However, from Fig. 6.22, no strong correlation could be found between the local burn duration and the overall burn duration. In this work, the four sheets form a measurement volume with a size of about 32 mm width $\times$ 12 mm height $\times$ 30 mm depth, centered around the spark plug. The size of the measurement volume is about 20.5 % of the size of the chamber volume at TDC, and is therefore considered to represent the early-stage combustion, to a large extent. The results shown above suggest that in the current working condition (Table 6.2) of this optical engine, no strong correlation between the local burning at the early stage of combustion and the overall burning duration could be found. Such a finding does not align with literature which show relations between the two [90, 91]. For example, Judith Laichter *et al.* identified a strong correlation between the equivalent flame radius versus the crank angle at which 10% of the fuel mass are burned (CA10) in a split injection DISI Engine [90]. Similarly, strong correlation between the flame area versus CA04 in a stratified-charge DISI engine was found in the work of Wei Zeng *et al.* [91]. The difference between the findings in this work and in the above literature could be originated from the stability of the chosen working conditions. In this chapter, the COV of the engine Indicated Mean Effective Pressure (IMEP) is 1.38%, which suggests that the engine was running under a relatively stable condition. In comparison, the IMEP COVs in [90] and [91] are 4% and 2.8%. For such a robust engine operating point, the engine could demonstrate consistent overall burning characteristics regardless of variations of the early-stage combustion. Enabled by the four-plane flame imaging approach, more future study could be performed to study correlations between early flame development, engine/fuel parameters, and engine performance (such as output torque, exhaust emission, knocking and so on). In principle, simultaneous flame imaging and flow velocimetry based on defocusing is feasible. By adding another two-cavity laser to the setup, the interaction between in-cylinder flow CCV, local combustion characteristics and engine performance could be studied in depth.

6.7 Summary

This chapter reports the first four-plane flame front detection based on defocusing particle imaging, using a single PIV laser. It is shown that the polarisation of the scattered light could change, which is inferred to be related to the lab jack pressure applied to the fused silica liner. In this work, temporal separation replaced polarisation separation, achieving a simultaneous two-plane measurement (by defocusing) and a quasi-simultaneous four-plane measurement (temporal, 2 μs between laser cavities). The failure of the polarisation discrimination approach highlights the value of the defocusing method, suggesting that in some cases where polarisation discrimination is not reliable, defocusing and wavelength would become the only two approaches to enable simultaneous multi-plane measurement. Based on defocusing and temporal separations, a four-plane flame front tracking test is demonstrated, with the same type of camera lens, same imaging optics and a similar working distance to the two-plane flame front tracking test in Chapter 5. Although applying temporal separation means that the four-plane measurement was not perfectly "simultaneous", a 2 μs time difference is equivalent to a 500 kHz rate of the scanning device in a scanning PIV test, which is not easily achieved (if it has been achieved). In this work, 2 μs equals 0.012 CAD, so on the engine timescale the "quasi-simultaneous" description is still reasonable.

With the four-plane flame imaging approach, this chapter explores the potential to relate local CCV of combustion on multiple planes to the overall CCV of engine performance. It is shown that a wide range of planar burn durations could happen with no detectable correlation with the overall burn duration, suggesting that: a) pressure-derived MFB is insensitive to local variation; b) the local (and early, to a certain extent) burn behaviour is dominated by other factors (such as in-cylinder flow) as combustion proceeds. The multi-plane imaging technique enables further investigations on this topic. In future, there is the potential for combining defocusing velocimetry and defocusing flame imaging, to further study the possible correlations between combustion CCV, flow CCV and engine performance, **even with the limited optical access**

offered by the optical engine, where a multi-camera tomographic PIV approach would be highly impractical.

Chapter 7

Conclusions

7.1 Contribution of this Thesis

This thesis is the first application and systematic evaluation of defocusing macroscopic PIV based on image splitting. The compact and low-cost image splitting optics design, as it stands, provides the potential to extend any existing single-plane PIV system to PIV on at least two planes, with high in-plane seeding density of typical planar PIV measurement. In principle, the image splitting optics assembly is also capable of pairing with the polarisation/wavelength method, to further extend the number of measurement planes for existing multi-plane PIV system. The compact design of the image splitting optics assembly makes it highly portable and can be easily adapted to typical PIV cameras. The image splitting principle is found to be compatible with Scheimpflug principle, therefore defocusing stereoscopic PIV is theoretically feasible.

A laminar flow rig test was assembled, to systematically evaluate the measurement accuracy of defocusing PIV. Based on experimental results and PIV theory, it is proved that the cross-talk between in-focus and out-of-focus images not only depends on plane separation, but also relates to the velocity fields on the two planes. This thesis categorises the measurement errors caused by out-of-focus crosstalk into three types: peaks merging, wrong peak discrimination, and peak shape change. Each type was

systematically evaluated and discussed using real particle images. It was found that with a field of view of 35 $\times$ 54 mm on each plane, the absolute two-plane crosstalk error is lower than 0.1 pixel per time step, with a 20 mm plane separation onwards.

The image splitting optics and defocusing PIV were successfully applied to simultaneously resolve the instantaneous swirl flow and tumble vortex structures in an optically accessible internal combustion engine. The two-plane cross-talk was evaluated using real particle images from the engine. The evaluation results overall aligned with the results in the laminar flow rig test, and also showed that the PIV loss of correlation caused by out-of-plane flow motions could increase the measurement error.

The image splitting optics and defocusing PIV were used for a simultaneous two-plane flame front measurement, for the first time. A novel two-step filter was specifically designed to enable highly reliable flame front tracking on two planes, by cross-referencing the particle images on the two planes. The two-plane cross-talk was evaluated using real particle images from the optical engine.

To enable simultaneous four-plane flame front tracking using a single PIV laser, a laser splitting optics design was proposed and built, to make advantage of the polarisation difference of laser beams from a typical two-cavity laser. The design is based on 3D printing, enabling a relatively quick and easy alignment for small optics with small distances. Four-plane flame front tracking was demonstrated in the optical engine. It is shown that the polarisation state of the scattered light could change and is spatially-dependent, which might be related to the stress-induced birefringence of fused silica under high pressure. The unsatisfying polarisation separation determined that defocusing separation and temporal separation were used for the four-plane flame imaging work, but it also highlights the contribution of the defocusing approach. In cases where polarisation separation is not reliable, defocusing separation and wavelength separation would become the only two methods for simultaneous multi-plane measurement, and the wavelength method is typically costly and adds complexity to the optics setup. It is also worth noting that, a 2 μs temporal separation is equivalent to a 500 kHz rate scanning device in a scanning PIV test, which could not be easily

achieved (if at all). In the four-plane flame imaging work, 2 μs is only 0.012 CAD in the engine cycle, which is a very short time, compared to typical engine behaviour.

In the end, this thesis explored the potential to evaluate the local combustion CCV, by comparing the local burn durations on four planes to the overall burn duration in the engine. Being a index for evaluating the overall CCV of engine performance, the overall burn duration cannot describe the local combustion characteristics. It is also shown that local CCV of combustion might be related to the in-cylinder flow. The four-plane flame imaging approach enables further studies on this topic.

7.2 Future Prospects

7.2.1 Extension of the Imaging Splitting Approach

One of the biggest shortcomings of the image splitting design is that the width of the field of view on each plane is limited by the mirror size. In this thesis, the width is limited by 35 mm, the size of the prism mirror. Theoretically the field of view width could be increased by using larger mirrors and beamsplitter. However, as the mirror size further increases, the more marginal areas of the camera lens are used for imaging, which could pose challenges on image quality. Although this is greatly dependent on camera lens design, it is very useful to inspect the potential for further increasing the field of view width with typical camera lenses, in order to further popularise the technique. Also, it is demonstrated that in theory, the image splitting device is compatible with Scheimpflug principle, while an actual defocusing two-plane stereoscopic PIV experiment will make the claim much more convincing. The capability of two-plane stereoscopic PIV using a single camera would greatly extend the application of the technique.

7.2.2 Further Evaluation on Out-of-focus Crosstalk

The laminar flow rig test systematically evaluated the two-plane crosstalk, but not fully comprehensively. It quantitatively evaluated how the in-plane velocity fields on the two planes could have impacts on the two-plane crosstalk, which is a significant contribution to PIV theory for defocusing macroscopic PIV. However, the effect of out-of-plane flow motion, which is another important consideration in an actual PIV setup, is not quantitatively evaluated. The findings in the laminar flow rig test are valid, only when the out-of-plane flow motions on two planes are equivalent or similar, since the loss-of-correlation could change the relative contributions of the in-focus correlation peak and the out-of-focus correlation peak. Although it is shown that the out-of-focus noise itself is not leading to PIV loss-of-correlation, the applicability of defocusing PIV in extreme cases where out-of-plane flow motion is causing trouble to even conventional single-plane PIV, as in 115 CAD bTDC in Chapter 4, is not quantitatively investigated. The reason for not deeply studying the out-of-plane effect yet is that, the thesis author has not found a way to quantitatively control out-of-plane flow motion in a well-controlled experimental setup like the laminar flow rig. The typical way for quantitatively studying the effect of out-of-plane flow motion is numerically generating particle images and changing them under preset velocity fields and out-of-plane motions. If experimental evaluations are proved not possible in future, numerical study is warranted.

7.2.3 Polarisation Issue

Based on the spatially-dependent and pressure-dependent characteristics of the polarisation change of the scatter light, it is inferred that stress-induced birefringence of fused silica under high pressure would be the cause. This needs to be further investigated. For example, it would be valuable to study whether the polarisation change effect is related to the fused silica windows/liner manufacture, the lab jack system design, etc. Such an investigation would be useful for future studies aiming to use polarisation

discrimination in similar facilities with high-pressure fused silica windows.

In the four-plane flame imaging work, even though polarisation separation was replaced by temporal separation, the images from camera 2 are darker by a factor more than 2. The physical reason to this is worth investigating. In terms of image quality, it could be improved by adding a half-wave plate after the first prism mirror next to the polarising beamsplitter, minimising the polarisation difference of the light imaged by the two cameras.

7.2.4 Future Directions on the Four-plane Work

The local CCV of combustion is inferred to be related to some other factors, such as the in-cylinder flow, and thereby the the engine performance. A further investigation on this topic would be novel in engine study. A set of reliable metrics for describing the correlations between the local combustion characteristics and engine performance would be valuable. Based on that, the impacts of different engine parameters and fuel components could be studied.

In principle, simultaneous flame imaging and flow velocimetry based on defocusing is feasible. If another two-cavity laser is added to the four-plane flame imaging setup, the double-frame functions of the high-speed cameras could be made advantage of, for flow velocity field evaluation. Separately, this Thesis shows that defocusing flow velocimetry and defocusing flame imaging are feasible. In principle, a "two-step" scheme could be used for simultaneous defocusing flow velocimetry and defocusing flame imaging. First, flame boundaries are derived in the processed images. Second, the flame boundaries found in the processed images could be used as masks in the unprocessed images for defocusing flow velocimetry.

There are also several improvements that could be made to the current four-plane setup. As discussed previously, adding a half-wave plate could potentially resolve the "darker images" issue. Based on that, a higher repetition rate of the PIV laser might be used, since the repetition rate of the high-speed laser is related to the maximum

pulse energy. Potentially, the current temporal resolution (2 CAD) could be improved to 1 CAD. In terms of data processing, different approaches for detecting unburned regions are worth investigating, in order to minimise the effects of varying background scatter. In addition, camera lenses with longer focal length could be used. When designing the four-plane test, it was anticipated that the fused silica liner region would be used for flame analysis, but in practice it was not. Therefore, the number of pixels addressing the pent-roof window region are small in the current setup.

7.2.5 Prediction of Performance

So far, the crosstalk evaluation has been based on using real flow and flame images. It would be useful to develop numerical models or theory to predict the performance of the defocusing technique, before actually building a real system. This would help researchers evaluate whether the defocusing technique is suitable for their work at the preparation stage. However, performance prediction would be challenging since it is relevant to the design of real camera lenses. The potential for using simplified camera lens models to numerically generate "out-of-focus" particles is an interesting topic for future work.

Appendix A

Particle Slide Test

This appendix presents the setup and results of the so-called "particle slide test", which is a "semi-quantitative" evaluation on the crosstalk between in-focus and out-of-focus particles at different plane separations. This was the first evaluation test performed by the author, on the accuracy of defocusing-based macroscopic PIV. It features an absolute validation case with known particle displacements. The work in this appendix is published in [92].

A.1 Experimental Setup

To begin with, two representative PIV "targets" were created by distributing PIV particles on top of microscope slides. Solid PIV particles (Polyamide Seeding Particles, diameter 5 μm, Dantec Dynamics, Fig. A.1) were added to water in a small glass bottle. The bottle was shaken for about 5 minutes, aiming for a homogeneous mixture. A couple of mixture drops were distributed across the surface of a microscope slide (Corning CLS294875X25 75 mm $\times$ 25 mm) using a pipette, then another microscope slide was placed on top. The target was ready for use when the water inside evaporated. This process was repeated to create two PIV targets, so the particle seeding numbers of the two targets were expected to be close. Each target was mounted on a pair of orthogonal translation stages using Thorlabs CH1A mounts. The stages provide

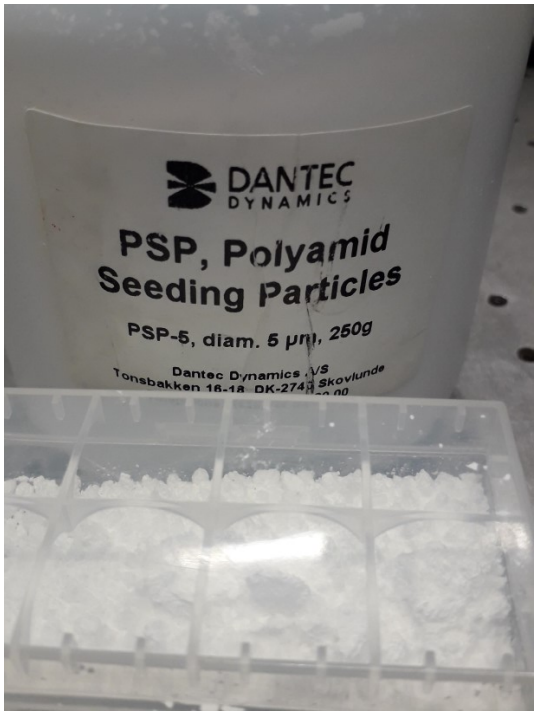

Figure A.1: The PIV particles used for creating the PIV targets.

controllable axial and lateral translations to create a pair of parallel PIV measurement planes. Fig. A.2 and Fig. A.3 show the diagram and real setup of the test. Fig. A.4 shows a raw image of one of the particle targets. The pair of axial translation stages (colored in orange in Fig. A.2) are the Thorlabs DTS50/M dovetail translation stages, and are responsible for controlling the plane separation between the in-focus and out-of-focus planes. The dovetail stages are manual stages so the plane separation was measured using a ruler. An LED torch was used to simultaneously illuminate the two particle targets. As shown in Fig. A.3, the LED torch was placed far away ($\sim$500 mm) from the targets, aiming for an as uniform as possible illumination. The pair of lateral translation stages (colored in blue in Fig. A.2) are the Thorlabs motorised stages driven by Z825B - 25 mm motorised actuator with a minimum resolution of 29 nm and a bidirectional repeatability of $\pm$0.8 μm, and are responsible for controlling the particle displacements seen from the camera (Photron FASTCAM 1024PCI). A working distance similar to the work in the main chapters was used, though it was not

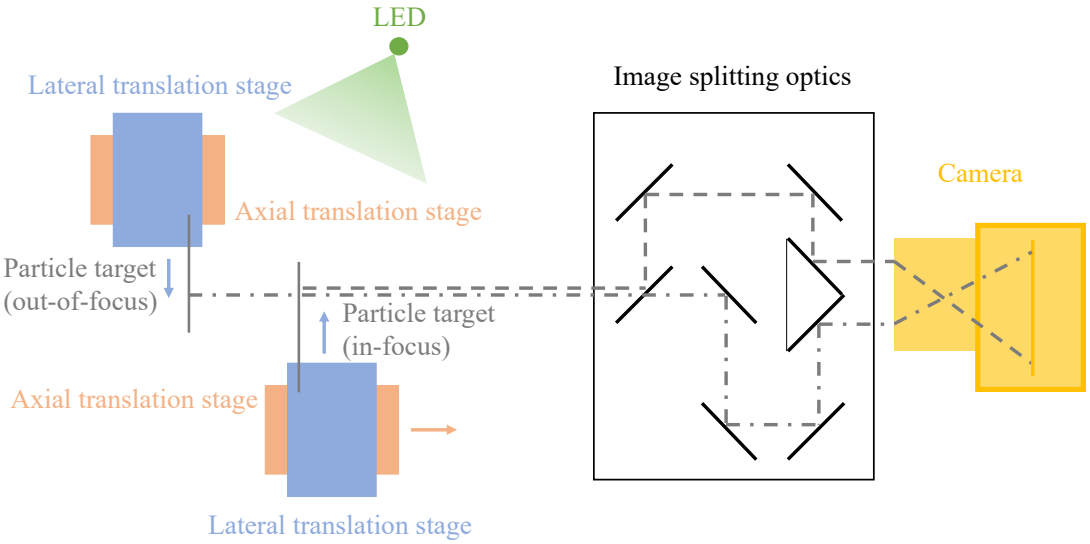

Figure A.2: The diagram of the particle slide test setup. A pair of "lateral translation stages" (blue) controlled the particle displacements. A pair of "axial translation stages" (orange) controlled the plane separation between the in-focus and the out-of-focus planes. An LED torch was used to illuminate the two particle targets.

possible to make it exactly the same.

The test steps are summarised as follows: for each plane separation (from 5 mm to 40 mm with a step of 5 mm), PIV measurements were simulated by illuminating the two target slides simultaneously with the torch LED. An image was taken before any lateral displacement occurred. The slides were then given opposite lateral translations, followed by a second image to be taken. Each image pair therefore contains both in-focus and out-of-focus particle images, with the two classes of particle images showing opposing displacements. In this test, the in-focus particle targets had a displacement of 1 mm ($\sim$ 8-pixel) towards the right hand side (seen from the camera images), and the out-of-focus particle targets had a displacement of 1 mm towards the left hand side.

The Matlab package PIVlab (v2.56) was used to calculate an apparent velocity field from each image pair, details of the PIV processing scheme can be found in the main chapters. A region of interest of 104 $\times$ 100 pixels was used for vector calculations.

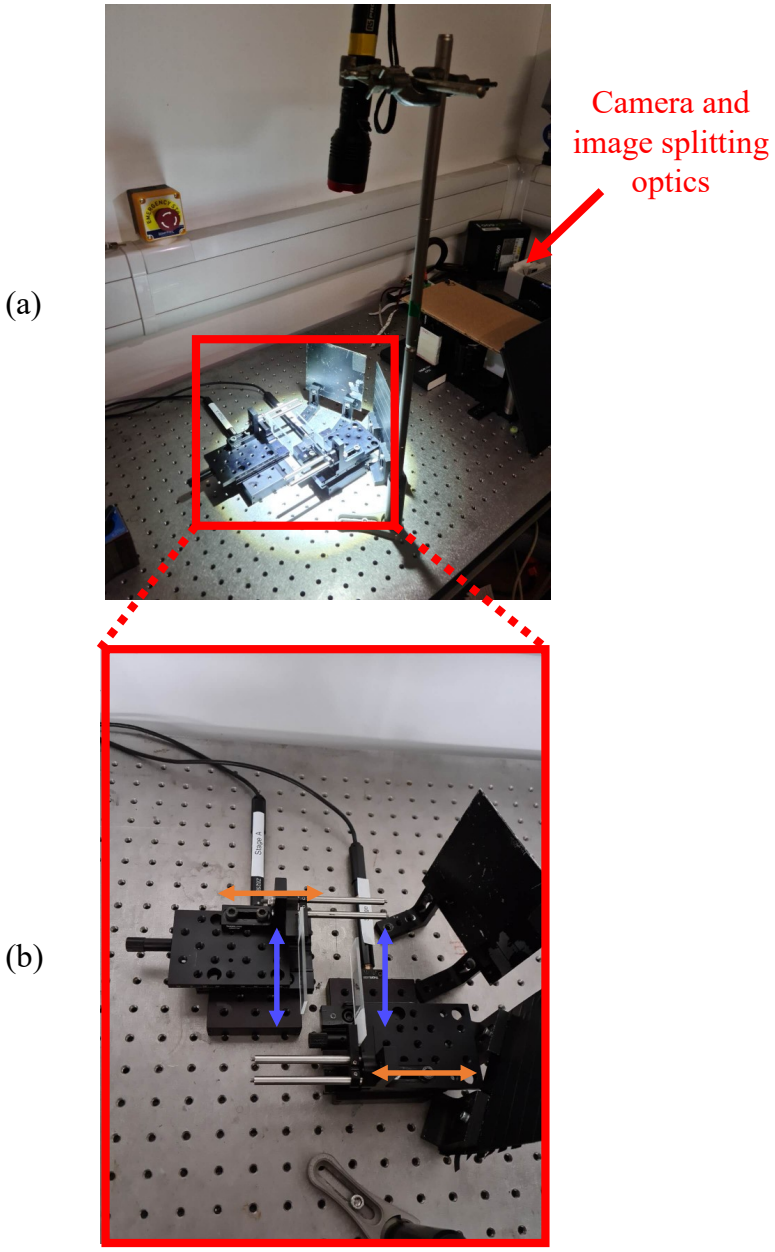

Figure A.3: Experimental setup of the particle slide test. (a) The overall setup. (b) An enlarged view of the translation stages and the particle targets.

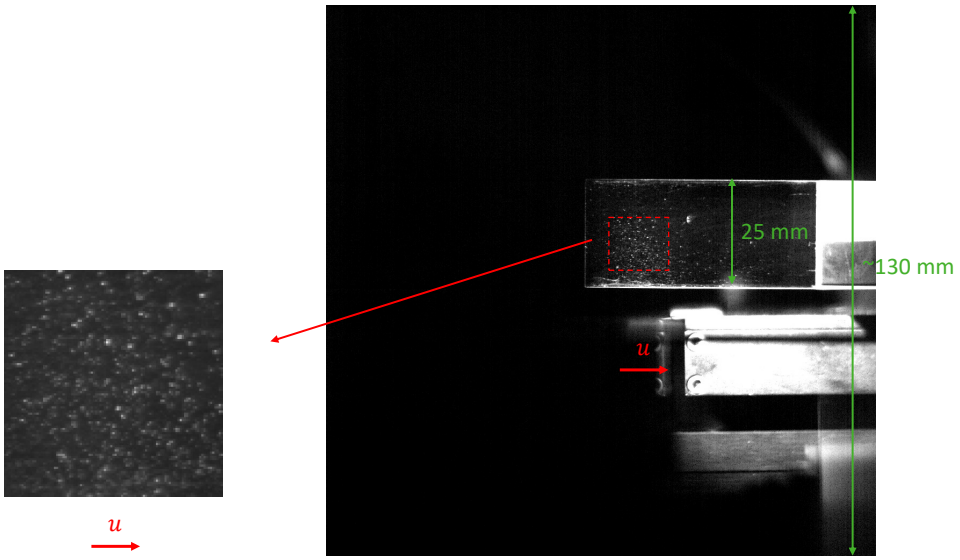

Figure A.4: A raw image of one of the two particle targets (in-focus). The enlarged view is the region of interest used for PIV vector generations.

The interrogation window size was reduced from 64 × 64 pixels to 16 × 16 pixels, with a 50% overlap between each window, leading to 132 vectors. To simulate particles moving in and out of the interrogation region, the vectors at the margins of the region of interest were not used for data analysis (the "vectors at the margin" are defined in the same way as in Fig. 4.15). In this test, the particle images on the reflected-side were used for analysis.

A.2 Results

An in-focus single-plane measurement provides a nominally correct result for comparison to the two-plane data. This single-plane measurement was recorded with the out-of-focus target removed. As introduced above, the in-focus particle target had a 1 mm displacement towards the right. The PIV vectors generated from cross-correlations would ideally output 1 mm as the measurement result. Here, because the lateral trans-

Table A.1: The values of data points in Fig A.5.

	Single-plane	5 mm	10 mm	15 mm	20 mm	25 mm	30 mm	35 mm	40 mm
Average	1	-0.9929	0.9917	0.9933	1.0066	0.9987	0.9981	0.9989	0.9977
Max	1.0082	-0.4226	1.1147	1.0879	1.0246	1.0289	1.0214	1.0192	1.0193
Min	0.9928	-1.4951	0.9100	0.9245	0.9800	0.9592	0.9697	0.9609	0.9672
Std	0.0034	0.1255	0.0277	0.0237	0.0091	0.0133	0.0106	0.0101	0.0100

lation stages were mounted on an optical table using several M6 holes, the "left and right" translation was not perfectly perpendicular to the optical access. Therefore the single-plane vectors output a velocity field with an average of 0.9566 mm (with a very narrow standard deviation, as shown below). This number was used to normalise the apparent velocities of both the single-plane and two-plane data, so that a value of "1" represents an exact match to the single-plane data. A normalised apparent velocity of "-1" represents a velocity vector in the opposite direction to this reference case (i.e. in the direction of the out-of-focus slide motion).

Fig. A.5 shows the apparent velocities calculated. The deviation of the apparent velocities from the reference case indicates the extent of the cross-talk between the two measurement planes as a function of plane separation. It is observed that the PIV cross-correlation algorithm cannot successfully recover the apparent velocity of the in-focus particles for a plane separation of 5 mm. Fig. A.6 shows an example correlation map of a 64 $\times$ 64 window at 5 mm plane separation, showing the two distinct correlation peaks generated from the two types of particles. When the plane separation is 5 mm, the out-of-focus particles are not significantly defocused, which still have relatively strong intensities but larger areas, leading to a stronger correlation peak in the correlation map. From 10 mm onwards, successful measurements for the in-focus displacement were achieved, and the standard deviation of the measurement is reducing overall. The values of mean, max, min and standard deviation are shown in Table A.1. At a plane separation of 10 mm, the mean normalised velocity ($\pm$ one standard deviation) of the vectors is 0.993 $\pm$ 0.028, compared to the ideal result of "1 $\pm$ 0.0034" of the single-plane in-focus particles. For plane separations $\geq$ 15 mm, the

(a)

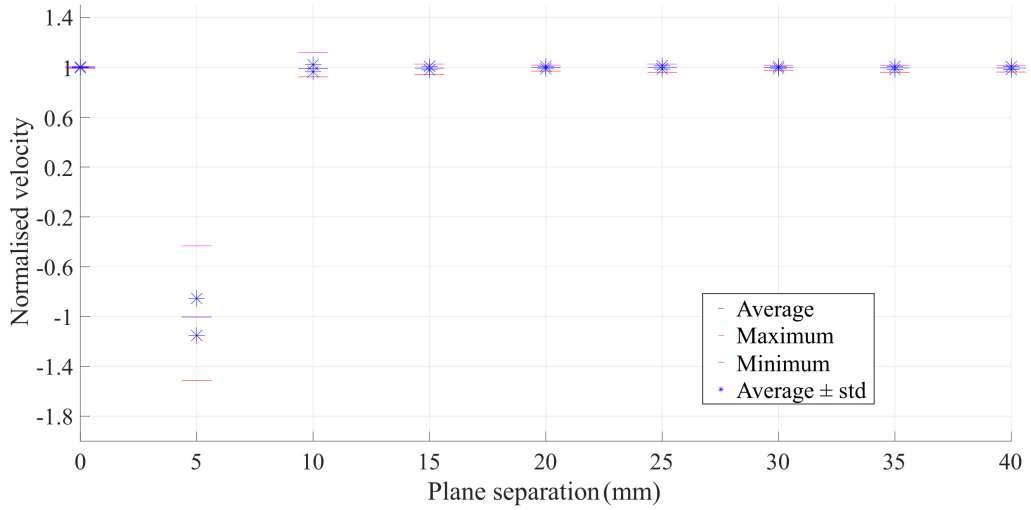

(b)

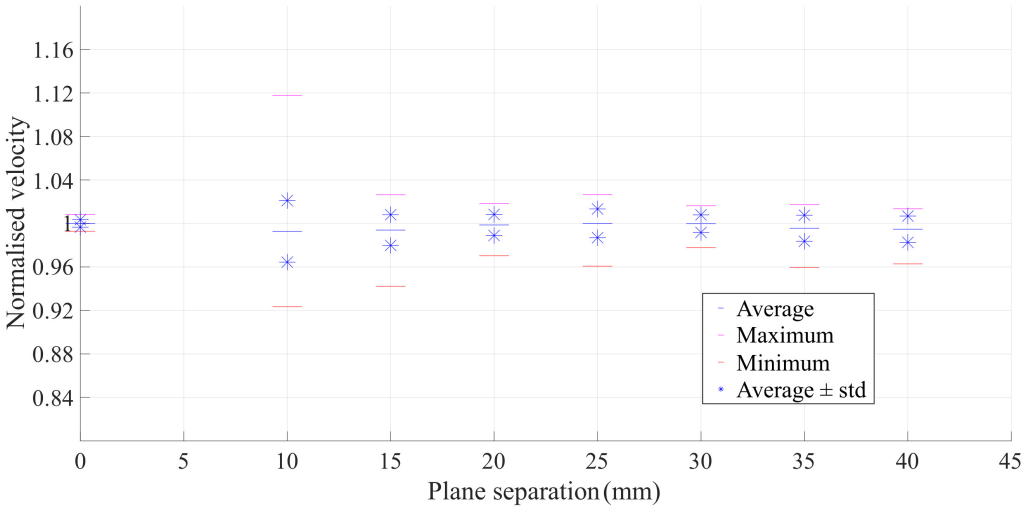

Figure A.5: Measurement of the apparent velocity of the in-focus particle target as a function of plane separation. The in-focus and out-of-focus test targets of were given known opposed translations between images 1 and 2 of each PIV image pair. A nominally correct in-focus single-target PIV measurement is plotted at 0 mm for reference. (b) is a zoom-in version of (a) by adjusting the velocity scale on y-axis. It is noticed that 5 mm separation test failed to recover the in-focus particle displacement. Successful measurements were achieved from 10 mm onwards, with an overall reducing standard deviation of the measurements.

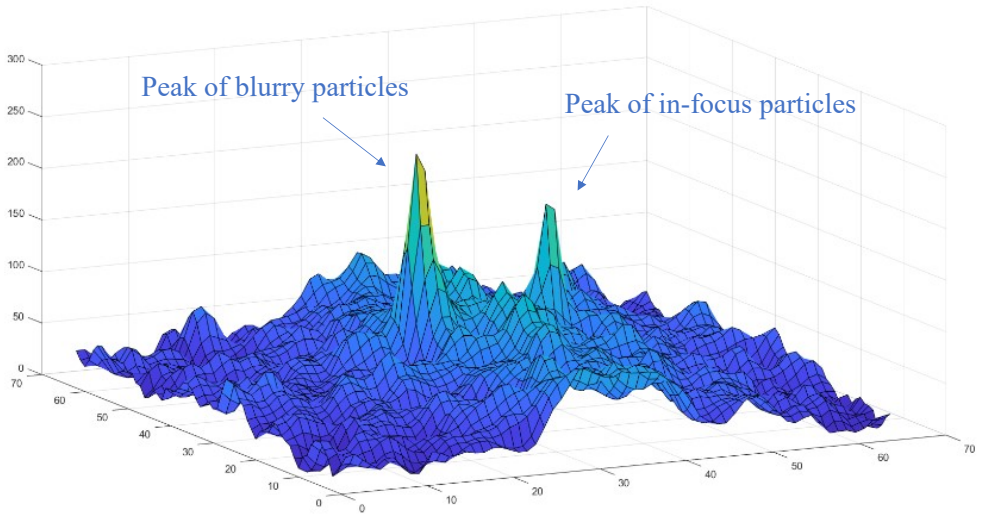

Figure A.6: An example correlation map of a 64 × 64 window, 5 mm plane separation. The correlation strength is normalised to 255 as the maximum. The correlation peak produced by the out-of-focus particles outweights the correlation peak produced by the in-focus particles.

mean normalised velocities are all within 0.6% of "1" with standard deviations smaller than 1.5%.

A.3 Summary and Discussions

This Appendix presents the setup and results of a particle slide test. Two PIV particle targets were created by dispersing solid PIV particles on top of microscope slides. Four translation stages were used to independently control the lateral displacements of the two PIV targets, and the plane separation between them. The two PIV targets were given oppose lateral displacements at different plane separations. The velocity vectors generated from two-plane tests where the two targets were simultaneously illuminated, were compared against the velocity vectors generated with the out-of-focus target removed. This comparison provided an evaluation of the cross-talk between in-focus and out-of-focus particles with different plane separations.

Compared to all other evaluation tests presented in this Thesis, the particle slide test features an absolute validation case, where the "ground truth" velocity vectors were absolutely known. No numerical addition of in-focus images to out-of-focus images was needed. As the very first experiment evaluating the technique, the particle slide test provided "promising" results, in which two-plane cross-talk did significantly reduce as the plane separation increased. This gave confidence to the Thesis author on exploring the technique further. However, the particle slide test was never a comprehensive validation of the technique. The test had two main drawbacks. Firstly, the illumination was provided by an LED torch. It could not simulate the spatial variation of the laser sheet energy, which is typical in a real PIV experiment and would make an impact on the two-plane cross-talk, as indicated in Chapter 3. Secondly, the difficulty of making good PIV targets with appropriate particle numbers and uniform particle distributions meant that it was challenging to evaluate the statistical cross-talk with a large sample size. The Thesis author made more than 20 targets, but only two of them appeared to have appropriate numbers of particles well distributed across the region of interest. Therefore, although the particle slide test has its unique advantages, it was not able to quantitatively evaluate the accuracy of the defocusing PIV technique. The thesis author decided to put it in this appendix, which is an essential part of the story of the technique development.

Bibliography

[1] Sherif S Rashwan, Medhat A Nemitallah, and Mohamed A Habib. Review on premixed combustion technology: stability, emission control, applications, and numerical case study. *Energy & Fuels*, 30(12):9981–10014, 2016.

[2] Thierry Poinsot and Denis Veynante. *Theoretical and numerical combustion*. RT Edwards, Inc., 2005.

[3] Y Naka, K Tomita, M Shimura, N Fukushima, M Tanahashi, and T Miyauchi. Quad-plane stereoscopic PIV for fine-scale structure measurements in turbulence. *Experiments in Fluids*, 57(5):1–20, 2016.

[4] Osborne Reynolds. An experimental investigation of the circumstances which determine whether the motion of water shall be direct or sinuous, and of the law of resistance in parallel channels. *Philosophical Transactions of the Royal society of London*, (174):935–982, 1883.

[5] E-J Marey. Le mouvement de l'air étudié par la chronophotographie. *J. Phys. Theor. Appl.*, 1(1):129–135, 1902.

[6] Ludwig Prandtl. Entstehung von wirbeln bei wasserströmungen - 2. anwendungen auf die strömung durch krümmer, hohlräume und verzweigungsstücke. Reichsanstalt für Film und Bild in Wissenschaft und Unterricht (RWU), 1936. https://doi.org/10.3203/IWF/C-2.

[7] PC Stainback and KA Nagabushana. Review of hot-wire anemometry techniques

and the range of their applicability for various flows. *Electronic Journal of Fluids Engineering, Transactions of the ASME*, 1993.

[8] Richard Stone. *Introduction to internal combustion engines*, volume 2. Macmillan, 1992.

[9] C Tropea. Laser Doppler anemometry: recent developments and future challenges. *Measurement Science and Technology*, 6(6):605, 1995.

[10] Sven Scharnowski and Christian J Kähler. Particle image velocimetry-classical operating rules from today's perspective. *Optics and Lasers in Engineering*, 135:106185, 2020.

[11] Markus Raffel, Christian E Willert, Fulvio Scarano, Christian J Kähler, Steve T Wereley, and Jürgen Kompenhans. *Particle image velocimetry: a practical guide*. Springer, 2018.

[12] Andreas Schröder and Christian E Willert. *Particle image velocimetry: new developments and recent applications*. Springer Science & Business Media, 2008.

[13] Ronald J Adrian. Scattering particle characteristics and their effect on pulsed laser measurements of fluid flow: speckle velocimetry vs particle image velocimetry. *Applied optics*, 23(11):1690–1691, 1984.

[14] Christopher JD Pickering and Neil A Halliwell. Laser speckle photography and particle image velocimetry: photographic film noise. *Applied optics*, 23(17):2961–2969, 1984.

[15] Richard D Keane and Ronald J Adrian. Theory and simulation of particle image velocimetry. In *Fifth International Conference on Laser Anemometry: Advances and Applications*, volume 2052, pages 477–492. SPIE, 1993.

[16] Richard D Keane and Ronald J Adrian. Optimization of particle image velocimeters. I. Double pulsed systems. *Measurement science and technology*, 1(11):1202, 1990.

[17] William Thielicke and Eize Stamhuis. PIVlab–towards user-friendly, affordable and accurate digital particle image velocimetry in MATLAB. *Journal of open research software*, 2(1), 2014.

[18] LaVision GmbH. *DaVis 8.4 Sofware Product Manual*. LaVision Göttingen, 2017.

[19] Ajay K Prasad. Stereoscopic particle image velocimetry. *Experiments in fluids*, 29(2):103–116, 2000.

[20] Toshio Hori and Jun Sakakibara. High-speed scanning stereoscopic PIV for 3D vorticity measurement in liquids. *Measurement Science and Technology*, 15(6):1067, 2004.

[21] Tao Li, Jhon Pareja, Lukas Becker, Wolfgang Heddrich, Andreas Dreizler, and Benjamin Böhm. Quasi-4D laser diagnostics using an acousto-optic deflector scanning system. *Applied Physics B*, 123:1–7, 2017.

[22] J Bode, J Schorr, C Krüger, A Dreizler, and B Böhm. Influence of the in-cylinder flow on cycle-to-cycle variations in lean combustion DISI engines measured by high-speed scanning-PIV. *Proceedings of the Combustion Institute*, 37(4):4929–4936, 2019.

[23] Nishab Ali and Andallib Tariq. Laminar and turbulent flow development study in a rectangular duct with 180° sharp bend by using stereo particle image velocimetry and liquid crystal thermography measurements. *Physics of Fluids*, 35(1), 2023.

[24] M Eletta Negretti, Francesco L Tucciarone, and Achim Wirth. Intruding gravity currents and re-circulation in a rotating frame: Laboratory experiments. *Physics of Fluids*, 33(9), 2021.

[25] Fulvio Scarano. Tomographic PIV: principles and practice. *Measurement Science and Technology*, 24(1):012001, 2012.

[26] Hecong Liu, Qianlong Wang, and Weiwei Cai. Assessment of plenoptic imaging for

reconstruction of 3D discrete and continuous luminous fields. *JOSA A*, 36(2):149–158, 2019.

[27] Timothy W Fahringer, Kyle P Lynch, and Brian S Thurow. Volumetric particle image velocimetry with a single plenoptic camera. *Measurement Science and Technology*, 26(11):115201, 2015.

[28] Timothy W Fahringer and Brian S Thurow. Plenoptic particle image velocimetry with multiple plenoptic cameras. *Measurement Science and Technology*, 29(7):075202, 2018.

[29] Gerrit E Elsinga, Fulvio Scarano, Bernhard Wieneke, and Bas W van Oudheusden. Tomographic particle image velocimetry. *Experiments in fluids*, 41(6):933–947, 2006.

[30] Matteo Novara and Fulvio Scarano. Performances of motion tracking enhanced Tomo-PIV on turbulent shear flows. *Experiments in fluids*, 52:1027–1041, 2012.

[31] John A Mullin and Werner JA Dahm. Dual-plane stereo particle image velocimetry measurements of velocity gradient tensor fields in turbulent shear flow. I. Accuracy assessments. *Physics of Fluids*, 18(3):035101, 2006.

[32] Christian J Kähler and Jürgen Kompenhans. Fundamentals of multiple plane stereo particle image velocimetry. *Experiments in Fluids*, 29(Suppl 1):S070–S077, 2000.

[33] MG Olsen and RJ Adrian. Out-of-focus effects on particle image visibility and correlation in microscopic particle image velocimetry. *Experiments in fluids*, 29(1):S166–S174, 2000.

[34] Massimiliano Rossi, Rodrigo Segura, Christian Cierpka, and Christian J Kähler. On the effect of particle image intensity and image preprocessing on the depth of correlation in micro-PIV. *Experiments in fluids*, 52(4):1063–1075, 2012.

[35] Michael G Olsen. Directional dependence of depth of correlation due to in-plane fluid shear in microscopic particle image velocimetry. *Measurement Science and Technology*, 20(1):015402, 2008.

[36] Michael G Olsen. Depth of correlation reduction due to out-of-plane shear in microscopic particle image velocimetry. *Measurement Science and Technology*, 21(10):105406, 2010.

[37] Rune Barnkob and Massimiliano Rossi. General defocusing particle tracking: fundamentals and uncertainty assessment. *Experiments in Fluids*, 61:1–14, 2020.

[38] Rune Barnkob, Christian J Kähler, and Massimiliano Rossi. General defocusing particle tracking. *Lab on a Chip*, 15(17):3556–3560, 2015.

[39] A Liberzon, R Gurka, and G Hetsroni. XPIV–Multi-plane stereoscopic particle image velocimetry. *Experiments in fluids*, 36(2):355–362, 2004.

[40] James F Driscoll, Jacqueline H Chen, Aaron W Skiba, Campbell D Carter, Evatt R Hawkes, and Haiou Wang. Premixed flames subjected to extreme turbulence: Some questions and recent answers. *Progress in Energy and Combustion Science*, 76:100802, 2020.

[41] Norbert Peters. *Turbulent Combustion*. Cambridge Monographs on Mechanics. Cambridge University Press, 2000.

[42] James F Driscoll. Turbulent premixed combustion: Flamelet structure and its effect on turbulent burning velocities. *Progress in Energy and Combustion Science*, 34(1):91–134, 2008.

[43] Isaac Boxx, Carson Slabaugh, Peter Kutne, Robert P Lucht, and Wolfgang Meier. 3 kHz PIV/OH-PLIF measurements in a gas turbine combustor at elevated pressure. *Proceedings of the Combustion Institute*, 35(3):3793–3802, 2015.

[44] Ayush Jain, Pradeep Parajuli, Yejun Wang, and Waruna D Kulatilaka. Hydroxyl

radical planar laser-induced fluorescence imaging in flames using frequency-tripled femtosecond laser pulses. *Optics Letters*, 45(17):4690–4693, 2020.

[45] Paul S Hsu, Mikhail N Slipchenko, Naibo Jiang, Christopher A Fugger, Austin M Webb, Venkat Athmanathan, Terrence R Meyer, and Sukesh Roy. Megahertz-rate OH planar laser-induced fluorescence imaging in a rotating detonation combustor. *Optics letters*, 45(20):5776–5779, 2020.

[46] Mamoru Tanahashi, Shinichirou Murakami, Gyung-Min Choi, Yuichi Fukuchi, and Toshio Miyauchi. Simultaneous CH–OH PLIF and stereoscopic PIV measurements of turbulent premixed flames. *Proceedings of the Combustion Institute*, 30(1):1665–1672, 2005.

[47] Brian Peterson, Elias Baum, Andreas Dreizler, and Benjamin Böhm. An experimental study of the detailed flame transport in a SI engine using simultaneous dual-plane OH-LIF and stereoscopic PIV. *Combustion and Flame*, 202:16–32, 2019.

[48] Benjamin R Halls, Naibo Jiang, Terrence R Meyer, Sukesh Roy, Mikhail N Slipchenko, and James R Gord. 4D spatiotemporal evolution of combustion intermediates in turbulent flames using burst-mode volumetric laser-induced fluorescence. *Optics letters*, 42(14):2830–2833, 2017.

[49] Lin Ma, Qingchun Lei, Tyler Capil, Stephen D Hammack, and Campbell D Carter. Direct comparison of two-dimensional and three-dimensional laser-induced fluorescence measurements on highly turbulent flames. *Optics letters*, 42(2):267–270, 2017.

[50] Sebastian Pfadler, Frank Beyrau, and Alfred Leipertz. Flame front detection and characterization using conditioned particle image velocimetry (CPIV). *Optics Express*, 15(23):15444–15456, 2007.

[51] Xiaoyang Wang, Kunpeng Liu, Chen Fu, Juan Yu, and Yi Gao. Investigation of

the applicability of conditioned particle image velocimetry under conditions close to lean blow-off. *Experiments in Fluids*, 64(6):118, 2023.

[52] Pavlos G Aleiferis and Markus K Behringer. Flame front analysis of ethanol, butanol, iso-octane and gasoline in a spark-ignition engine using laser tomography and integral length scale measurements. *Combustion and Flame*, 162(12):4533–4552, 2015.

[53] Christine Mounaïm-Rousselle, Ludovic Landry, Fabien Halter, and Fabrice Foucher. Experimental characteristics of turbulent premixed flame in a boosted Spark-Ignition engine. *Proceedings of the Combustion Institute*, 34(2):2941–2949, 2013.

[54] Yutao Zheng, Lee Weller, and Simone Hochgreb. Instantaneous flame front identification by Mie scattering vs. OH PLIF in low turbulence Bunsen flame. *Experiments in Fluids*, 63(5):79, 2022.

[55] Sebastian Pfadler, Friedrich Dinkelacker, Frank Beyrau, and Alfred Leipertz. High resolution dual-plane stereo-PIV for validation of subgrid scale models in large-eddy simulations of turbulent premixed flames. *Combustion and flame*, 156(8):1552–1564, 2009.

[56] Johannes Kerl, Chris Lawn, and Frank Beyrau. Three-dimensional flame displacement speed and flame front curvature measurements using quad-plane PIV. *Combustion and flame*, 160(12):2757–2769, 2013.

[57] Dominik Ebi and Noel T Clemens. Simultaneous high-speed 3D flame front detection and tomographic PIV. *Measurement Science and Technology*, 27(3):035303, 2016.

[58] Qichi He, Christopher Willman, Richard Stone, and Benjamin AO Williams. Inexpensive multi-plane particle image velocimetry based on defocusing: Proof of concept on two-component measurement. *Physics of Fluids*, 35(6), 2023.

[59] Qichi He, Christopher Willman, Richard Stone, and Benjamin AO Williams. Data for 'Inexpensive multi-plane particle image velocimetry based on defocusing: proof of concept on two-component measurement'. University of Oxford, 2023. http://dx.doi.org/10.5287/ora-xqv18vnrx.

[60] William Thielicke and René Sonntag. Particle Image Velocimetry for MATLAB: Accuracy and enhanced algorithms in PIVlab. *Journal of Open Research Software*, 9(1), 2021.

[61] H Nobach and M Honkanen. Two-dimensional gaussian regression for sub-pixel displacement estimation in particle image velocimetry or particle position estimation in particle tracking velocimetry. *Experiments in fluids*, 38:511–515, 2005.

[62] Christopher J Bourdon, Michael G Olsen, and Allen D Gorby. Validation of an analytical solution for depth of correlation in microscopic particle image velocimetry. *Measurement Science and Technology*, 15(2):318, 2003.

[63] Andrea Sciacchitano. Uncertainty quantification in particle image velocimetry. *Measurement Science and Technology*, 30(9):092001, 2019.

[64] Christian J Kähler, Tommaso Astarita, Pavlos P Vlachos, Jun Sakakibara, Rainer Hain, Stefano Discetti, Roderick La Foy, and Christian Cierpka. Main results of the 4th International PIV Challenge. *Experiments in Fluids*, 57:1–71, 2016.

[65] Ning Liu, Yue Wu, and Lin Ma. Quantification of tomographic piv uncertainty using controlled experimental measurements. *Applied optics*, 57(3):420–427, 2018.

[66] David L Reuss. Cyclic variability of large-scale turbulent structures in directed and undirected IC engine flows. *SAE transactions*, pages 128–145, 2000.

[67] Nir Ozdor, Mark Dulger, and Eran Sher. Cyclic variability in spark ignition engines a literature survey. *SAE transactions*, pages 1514–1552, 1994.

[68] Tetsuo Omura, Koichi Nakata, Yasushi Yoshihara, and Daishi Takahashi. Research on the measures for improving cycle-to-cycle variations under high tumble combustion. Technical report, SAE Technical Paper, 2016.

[69] Yasushi Yoshihara, Koichi Nakata, Daishi Takahashi, Tetsuo Omura, and Atsuharu Ota. Development of high tumble intake-port for high thermal efficiency engines. Technical report, SAE Technical Paper, 2016.

[70] Bahram Khalighi. Intake-generated swirl and tumble motions in a 4-valve engine with various intake configurations—flow visualization and particle tracking velocimetry. *SAE transactions*, pages 354–374, 1990.

[71] Daming Liu, Tianyou Wang, Ming Jia, and Gangde Wang. Cycle-to-cycle variation analysis of in-cylinder flow in a gasoline engine with variable valve lift. *Experiments in fluids*, 53:585–602, 2012.

[72] Tianyou Wang, Daming Liu, Bingqian Tan, Gangde Wang, and Zhijun Peng. An investigation into in-cylinder tumble flow characteristics with variable valve lift in a gasoline engine. *Flow, Turbulence and Combustion*, 94:285–304, 2015.

[73] Helmut Ruhland, Thomas Lorenz, Jens Dunstheimer, Albert Breuer, and Maziar Khosravi. A study on charge motion requirements for a class-leading GTDI engine. Technical report, SAE Technical Paper, 2017.

[74] Wei Zeng, Magnus Sjöberg, and David L Reuss. PIV examination of spray-enhanced swirl flow for combustion stabilization in a spray-guided stratified-charge direct-injection spark-ignition engine. *International Journal of Engine Research*, 16(3):306–322, 2015.

[75] Douglas Heim and Jaal Ghandhi. A detailed study of in-cylinder flow and turbulence using PIV. *SAE International Journal of Engines*, 4(1):1642–1668, 2011.

[76] Roberto Berlini Rodrigues da Costa, Raphael Meireles Braga, Carlos Alberto Gomes Júnior, Ramón Molina Valle, and Rudolf Huebner. PIV measurements

and numerical analysis of in-cylinder tumble flow in a motored engine. *journal of the Brazilian Society of Mechanical Sciences and Engineering*, 39:3931–3945, 2017.

[77] A Kalpakli Vester, Y Nishio, and P Henrik Alfredsson. Investigating swirl and tumble using two prototype inlet port designs by means of multi-planar PIV. *International Journal of Heat and Fluid Flow*, 75:61–76, 2019.

[78] Paul C Miles. The history and evolution of optically accessible research engines and their impact on our understanding of engine combustion. In *Internal Combustion Engine Division Fall Technical Conference*, volume 46179, page V002T08A003. American Society of Mechanical Engineers, 2014.

[79] HR Ricardo. Some notes on gasoline-engine development. Technical report, 1927.

[80] Lloyd Withrow and TA Boyd. Photographic flame studies in the gasoline engine. *Industrial & Engineering Chemistry*, 23(5):539–547, 1931.

[81] Gerald M Rassweiler and Lloyd Withrow. High-speed motion pictures of engine flames. *Industrial & Engineering Chemistry*, 28(6):672–677, 1936.

[82] Gerald M Rassweiler and Lloyd Withrow. Motion pictures of engine flames correlated with pressure cards. *SAE transactions*, pages 185–204, 1938.

[83] Dana W Lee. A study of air flow in an engine cylinder. Technical report, 1939.

[84] Frederick W Bowditch and Lloyd L Withrow. Cylinder and piston assembly, January 5 1960. US Patent 2,919,688.

[85] Xiaowei Wang. *Instantaneous in-cylinder heat transfer and combustion analysis in spark ignition engines*. PhD thesis, University of Oxford, 2008.

[86] Blane Scott. *Flow and combustion in direct injection spark ignition engines*. PhD thesis, University of Oxford, 2019.

[87] Christopher Willman, Blane Scott, Richard Stone, and David Richardson. Quantitative metrics for comparison of in-cylinder velocity fields using particle image velocimetry. *Experiments in Fluids*, 61:1–16, 2020.

[88] Qichi He, Christopher Willman, and Benjamin AO Williams. Simultaneous two-plane flame front detection using PIV based on defocusing. *Optics Letters*, 49(3):422–425, 2024.

[89] Dirk-Jan Kroon. 2D Line Curvature and Normals. MATLAB Central File Exchange, 2024. https://www.mathworks.com/matlabcentral/fileexchange/32696-2d-line-curvature-and-normals.

[90] Judith Laichter and Sebastian A Kaiser. Optical investigation of the influence of in-cylinder flow and mixture inhomogeneity on cyclic variability in a direct-injection spark ignition engine. *Flow, Turbulence and Combustion*, 110(1):171–183, 2023.

[91] Wei Zeng, Magnus Sjöberg, David L Reuss, and Zongjie Hu. The role of spray-enhanced swirl flow for combustion stabilization in a stratified-charge disi engine. *Combustion and Flame*, 168:166–185, 2016.

[92] Christopher Willman, Qichi He, Benjamin A O Williams, Richard Stone, and Matthew McAllister. Multi-plane PIV using depth of field for in-cylinder flow measurements. *SAE Technical Papers*, 2023-01-0213, 2023.